

AN ABSTRACT OF THE THESIS OF

Younghoon Kwak for the degree of Doctor of Philosophy in Mechanical Engineering presented on June 19, 2008.

Title: Experimental Study of Two-Phase Gas-Liquid Flow in a Microscale Fractal-Like Branching Flow Network.

Abstract approved

Deborah V. Pence

Two-phase gas-liquid flows in microscale fractal-like branching channel flow networks were experimentally studied to assess the validity of existing void fraction correlations and flow regimes based on superficial gas and liquid velocities. Void fractions were assessed using two different methods. First, void fraction data were acquired using a High-Speed-High-Resolution (HSHR) camera and computed by area-based two-dimensional image analysis. Void fraction data were also computed using a slip ratio, defined as gas velocity over liquid velocity. Liquid velocity represents the bulk-averaged liquid velocity as determined by microscale particle image velocimetry (micro-PIV). Gas velocity was determined by averaging gas-liquid interface velocities made at the channel centerline.

The fractal-like branching channel flow network has five bifurcation levels of different channel widths varying from 400 μm to 100 μm with a fixed channel depth

of 250 μm . Each downstream width decreases by 30% whereas the downstream lengths increase by 40%. The total flow length through a single path is approximately 18 mm. Filtered air and deionized water were used as the gas and liquid working fluids, respectively. Mass flow rates of air and water into each $k=0$ branch were varied from 0.3 g/min to 2.5 g/min and from 5.2×10^{-5} g/min to 1.3×10^{-2} g/min, respectively. These flow rates yielded superficial air and water velocities through the same branch level between 0.007 m/s and 1.8 m/s and between 0.05 m/s and 0.42 m/s, respectively.

For each branching level, due to an increase in flow area, the superficial liquid and gas flow rates change. A two-phase flow regime map was generated for each level of the fractal-like branching flow network and compared to maps developed using the Taitel and Dukler (1976) model and to maps presented in Chung and Kawaji (2004). Flow regime transitions are well predicted with the Taitel and Dukler (1976) model for each branching level.

Void fraction assessed using the slip ratio shows very good agreement with the homogeneous void fraction model for all branching levels. On the other hand, void fraction determined by area-based two-dimensional image analysis shows better agreement with the void fraction correlation of Zivi (1964).

©Copyright by Younghoon Kwak
June 19, 2008
All Rights Reserved

Experimental Study of Two-Phase Gas-Liquid Flow
in a Microscale Fractal-Like Branching Flow Network

by

Younghoon Kwak

A THESIS

submitted to

Oregon State University

in partial fulfillment of
the requirements for the
degree of

Doctor of Philosophy

Presented June 19, 2008
Commencement June 2009

Doctor of Philosophy thesis of Younghoon Kwak presented on June 19, 2008.

APPROVED:

Major Professor, representing Mechanical Engineering

Head of the School of Mechanical, Industrial and Manufacturing Engineering

Dean of the Graduate School

I understand that my thesis will become part of the permanent collection of Oregon State University libraries. My signature below authorizes release of my thesis to any reader upon request.

Younghoon Kwak, Author

ACKNOWLEDGEMENTS

I would like to take the opportunity to thank the people who made contributions to this work. First, I would like to thank Dr. Deborah Pence, my advisor and mentor, and draft reviewer of this dissertation. I will never forget what I have learned from her while completing my Ph.D. degree in Mechanical Engineering at Oregon State University.

Thank you Dr. James Liburdy, Dr. Vinod Narayanan, Dr. Sourabh Apte and Dr. Jhon Nairn for serving on my committee. Specifically, I would like to thank both Dr. Liburdy and Dr. Narayanan for advise they provided me during the completion of this work and for granting me permission to use their experimental equipment.

I would like to thank the graduate students involved in this project, Douglas Heymann, Edwards Lee and Daniel Krebs. I really enjoyed working and sharing time with them. I would like to give special thank to Douglas for developing and sharing with me his image processing code. I also, thank Myeong Chan Jo, my only Korean friend in Mechanical Engineering, for sharing good conversations in Korean over coffee.

Finally, I would like to share my appreciation of my parents, living in my home country, for their support and encouragement with endless love. I owe my deepest gratitude to my wife, Hye-Kyong and to my two sons, Matthew and Joshua living here with me in Corvallis, Oregon. Without their loving support, I could never have finished this work. I dedicate this to them.

TABLE OF CONTENTS

	<u>Page</u>
1 INTRODUCTION	1
2 LITERATURE REVIEW	6
2.1 Straight Microchannel Flows	6
2.1.1 Single-phase flow	7
2.1.2 Two-phase boiling flow	8
2.1.3 Two-phase liquid-gas microchannel flow	10
2.2 Fractal-like Branching Channel Flow Network	14
2.3 PIV and Bubble Velocity Measurements	19
3 EXPERIMENT FACILITY	23
3.1 Test Device	23
3.2 Manifold	26
3.3 Flow Loop	28
3.4 High-Speed-High-Resolution (HSHR) Imaging System	31
3.5 Micro-PIV Setup	32
3.5.1 Laser	33
3.3.2 Flow additives	34
3.3.3 CCD Camera	35
3.3.4 Optics	35
3.3.5 Dantec [®] System Hub	37
4 FLOW REGIME MAPS AND VOID FRACTION CORRELATIONS	38
4.1 Flow Regime Maps	38
4.1.1 Theoretical flow map generation	38
4.1.2. HSHR and micro-PIV test plan	43

TABLE OF CONTENTS (Continued)

	<u>Page</u>
4.2 Void Fraction	48
4.2.1 Void fraction based on slip ratio	48
4.2.2 Void fraction based on HSHR images	49
4.2.3 Existing void fraction correlations	50
5 EXPERIMENTAL PROCEDURES AND DATA ANALYSIS	52
5.1 Experiment Procedure	52
5.1.1 Global measurements	52
5.1.2 HSHR imaging	53
5.1.3 Micro-PIV imaging	56
5.2 Data Analysis	58
5.2.1 Data reduction of global measurements	58
5.2.2 Data reduction from HSHR images	61
5.2.3 Data reduction from PIV images	66
5.2.4 Average liquid velocities	68
5.2.5 Average gas velocities	73
6 RESULTS AND DISCUSSION	76
6.1 Flow Regimes	76
6.2 Void Fraction Correlations and Comparison	92
6.2.1 Slip ratio	92
6.2.2 Void fraction comparison with existing correlations	96
6.2.3 Comparisons of void fractions	98
6.3 Velocity Flow Fields at Bifurcations	103
7 CONCLUSIONS AND RECOMMENDATIONS	113
7.1 Conclusions	113
7.2 Recommendations	115
BIBLIOGRAPHY	117

TABLE OF CONTENTS (Continued)

	<u>Page</u>
APPENDICES	122
APPENDIX A Wave Length Spectra of Fluorescent Particles	123
APPENDIX B Two-Phase Flow Regime Map	126
APPENDIX C Image and Data Analysis Program	132
APPENDIX D Uncertainty Analysis	152

LIST OF FIGURES

<u>Figure</u>	<u>Page</u>
1.1 Fractal-like branching flow network	3
2.1 Label of each branch with channel geometry (Pence (2000))	14
3.1 Fractal-like branching channel pattern with $\gamma = 1.414$	25
3.2 (a) Manifold and (b) vacuum chuck with (c) enlarged view of top surface of vacuum chuck (used, with permission, from Cullion (2005))	27
3.3 Schematic diagram for flow loop	30
3.4 Schematic diagram for gas injector	30
3.5 Schematic diagram of HSHR imaging system	32
3.6 Schematic diagram of micro-PIV system	33
3.7 Schematic diagram of microscope objective	37
4.1 Representative non-dimensional two-phase gas-liquid flow regime map. Stratified wavy, annular dispersed, and dispersed bubble presented with symbols of blue squares, green crosses, red circles, respectively. The intermittent flow regime is blank	42
4.2 Two-phase flow regime maps for each branching level of k in the fractal-like branching channel networks. (a) at $k=0$ with $D_h=308 \mu\text{m}$, (b) at $k=1$ with $D_h=265 \mu\text{m}$	46
Two-phase flow regime maps for each branching level of k in the fractal-like branching channel networks. (c) at $k=2$ with $D_h=222 \mu\text{m}$, (d) at $k=3$ with $D_h=180 \mu\text{m}$	47
Two-phase flow regime maps for each branching level of k in the fractal-like branching channel networks. (e) at $k=4$ with $D_h=143 \mu\text{m}$	48
4.3 Void fraction versus homogeneous void fraction based on four different existing correlations	51

LIST OF FIGURES (Continued)

<u>Figure</u>	<u>Page</u>
5.1 Locations for acquiring HSHR images for each branching channel level	55
5.2 Locations for acquiring PIV images for each branching channel level	57
5.3 Image process for base image for k=0 branching level. (a) original image with liquid only, (b) used contrast enhancement, (c) used noise remove filter, (d) image complement, (e) filling darker pixels inside channel region are brightened, (f) binary image	62
5.4 Image process for creating binary two-phase flow images to determine area averaged void fraction. (a) original image, (b) base image, (c) binary image for bubble only, (d) binary image for liquid film only	63
5.5 . Schematic diagram to understand liquid film observation near corner of channel wall and bubble front. Shaded area can be observed as dark thick liquid film and solid and dash lines represent incoming light and reflected light. (a) side view (flow direction: from left to right), (b) cross-sectional view A-A' (flow direction: into images)	65
5.6 Rectangular geometry with coordinate system and parameter identification	69
5.7 Experimental velocity profiles along the axial direction at the k=0 branch (mass flow rates of gas and liquid are 20 g/min and 0.03 g/min, respectively)	71
5.8 Experimental and analytical fully developed velocity profiles at the k=0 branch	72
5.9 Three-dimensional fully developed velocity profile	72
5.10 Three different types of bubble images at k=0 branching level	74

LIST OF FIGURES (Continued)

<u>Figure</u>	<u>Page</u>
5.11 Interface velocity assessment (a) first image in image pair (b) second image in image pair, and (c) intensity variations in (a) and (b)	75
6.1 Two-phase flow patterns comparisons between (a) Kawaji and Chung (2004) and (b) present study at k=0 branch level	77
6.2 Flow patterns for 12 different gas-liquid flow conditions in branching level of k=0	81
6.3 Flow patterns for 12 different gas-liquid flow conditions in branching level of k=1	82
6.4 Flow patterns for 12 different gas-liquid flow conditions in branching level of k=2	83
6.5 Flow patterns for 12 different gas-liquid flow conditions in branching level of k=3	84
6.6 Flow patterns for 12 different gas-liquid flow conditions in branching level of k=4	85
6.7 Flow regime map comparisons between Taitel and Dukler (1976) and Chung and Kwaji (2004) with flow pattern observations. (a) flow regime maps for k=0 branch, (b) flow regime map for k=1	89
6.8 Flow regime map comparisons between Taitel and Dukler (1976) and Chung and Kwaji (2004) with flow pattern observations. (a) flow regime map for k=2 branch, (b) flow regime map for k=3	90
6.9 Flow regime map comparisons between Taitel and Dukler (1976) for k=4 branch and other studies of (a) Kawahara et al. 100 μm tube and (b) Chung and Kwaji (2004) 96 μm square channel with flow pattern observations	91
6.10 . Centerline bubble velocities based on only (a) leading edges and (b) trailing edges of bubbles appeared in the field of view at k=0 for case 8 (average leading velocity is 0.23 m/s with $\sigma = \pm 0.05$ m/s and average trailing velocity is 0.23 m/s with $\sigma = \pm 0.03$ m/s)	94

LIST OF FIGURES (Continued)

<u>Figure</u>	<u>Page</u>
6.11 Centerline bubble velocities (a) both leading and trailing edges of bubbles appeared in the field of view and (b) velocity differences of between leading and trailing centerline velocities at $k=0$ for case 8. (average leading velocity is 0.24 m/s with $\sigma = \pm 0.04$ m/s and average trailing velocity is 0.24 m/s with $\sigma = \pm 0.04$ m/s)	95
6.12 α_{slip} and α_{image} v.s. β for $k=0$ branching level with void fraction correlations	101
6.13 α_{slip} and α_{image} v.s. β for $k=2$ branching level with void fraction correlations	101
6.14 α_{slip} and α_{image} v.s. β for $k=4$ branching level with void fraction correlations	102
6.15 α_{image} v.s. β for all branching level with void fraction correlations of homogeneous, Zivi (1064), Chung et al. (2004)	102
6.16 Experimental 2-D velocity vector fields at the bifurcation between $k=0$ and $k=1$ with u-v component contour plots. (a) liquid only, (b) bubble presence	107
6.17 Experimental 2-D velocity vectors and contour at bifurcation between $k=0$ and $k=1$. (a) original micro-PIV image, (b) contour plot, (c) vector plot, (d) zoomed in dotted box	108
6.18 Experimental 2-D velocity vectors and contour at bifurcation between $k=0$ and $k=1$. (a) original micro-PIV image, (b) contour plot, (c) vector plot, (d) zoomed in dotted box	109
6.19 Experimental 2-D velocity vector fields at the bifurcation between $k=1$ and $k=2$ with u-v component contour plots. (a) liquid only, (b) bubble presence	110
6.20 Experimental 2-D velocity vectors and contour at bifurcation between $k=1$ and $k=2$. (a) original micro-PIV image, (b) contour plot, (c) vector plot, (d) zoomed in dotted box	111

LIST OF FIGURES (Continued)

<u>Figure</u>	<u>Page</u>
6.21 Experimental 2-D velocity vector fields at the bifurcation between k=3 and k=4 with u-v component contour plots. (a) liquid only, (b) bubble presence	112

LIST OF TABLES

<u>Table</u>		<u>Page</u>
3.1	Channel dimensions	25
4.1	Test plan for HSHR and micro-PIV experiments at $k=0$	45
6.1	Average slip ratios for five different cases for each branching level ..	96

NOMENCLATURE

A	Cross-sectional area
C	Friction factor coefficient
D	Diameter of tube
D_h	Hydraulic diameter, $\frac{4WH}{2(W + H)}$
e	Pixel size of CCD camera
F	Non-dimensional value, $F = \sqrt{\frac{\rho_g}{(\rho_f - \rho_g)}} \frac{j_g}{\sqrt{Dg}}$
f	Frequency
g	Gravitational acceleration
H	Height of channel
h	Height of liquid or gas phase level in a channel
j	Superficial velocity
k	Branching level
L	Length of channel
M	Magnification or molecular weight
\dot{m}	Mass flow rate
n	Index of refraction of medium
NA	Numerical aperture
P	Pressure
p	White pixel in a binarized image
Q	Volumetric flow rate

NOMENCLATURE (Continued)

q	Number of pixels defining the area of interest
\bar{R}	Universal gas constant
Re_D	Reynolds number based on the hydraulic diameter, $\left(\frac{\rho u D_h}{\mu} \right)$
r	Number of frames in a movie
S	Perimeters of channels
T	Non-dimensional value, $T = \left[\frac{\frac{4C_f}{D} \left(\frac{j_f D}{\nu_f} \right)^{-n} \frac{\rho_f j_f^2}{2}}{(\rho_f - \rho_g)g} \right]^{1/2}$
u	Instantaneous velocity in x (streamwise) direction
u_{lead}	Leading edge bubble velocity
u_{max}	Maximum u component of velocity
u_{trail}	Trailing edge bubble velocity
u'	Non-dimensional u component of velocity, u/u_{max}
v	Instantaneous velocity in y (spanwise) direction
ν_f	Specific volume of liquid
ν_g	Specific volume of gas
W	Width of channel
X_{LM}	Two-phase parameter (Lockhart and Martinelli)
x	Streamwise location relative to local coordinate system (μm) / quality

NOMENCLATURE (Continued)

y	Spanwise location relative to local coordinate system (μm)
y'	Non-dimensional $y \left(\frac{y - \left(\frac{1}{2}w_k\right)}{\left(\frac{1}{2}w_k\right)} \right)$
z	Depth relative to local coordinate system

GREEKS

α	Void fraction
α_{slip}	Void fraction based on slip ratio
α_{image}	Void fraction based on area averaged images
α^*	Aspect ratio, $\left(\frac{H}{W} \right)$
β	Homogeneous void fraction
δz	Depth of field
λ	Wavelength
μ	Dynamic viscosity
ν	Kinematic viscosity
ρ	Density
σ	Standard deviation
τ	Shear stress

NOMENCLATURE (Continued)

SUPERSCRIPTS

–	Non-dimensional form
s	Superficial

SUBSCRIPTS

b	Full bubble image
c	Bubble curvature image
f	Liquid phase
fd	Fully developed
g	Gas phase
gi	Gas at gas injector
gm	Gas at flowmeter
i	Gas-liquid interface
k	Branching level index
t	Total region of interest in image
w	Wall of channel

CHAPTER 1

INTRODUCTION

During the past three decades, single-phase and two-phase flows in microchannels have been actively studied for use in many fields and for specific technologies such as electronic cooling, micro-reactors, fuel cell technology, and medical and genetic sensors, among others. Use of microchannels for electronic cooling was first introduced and studied by Tuckerman and Peace (1981). This study was based on single-phase flow through a heat sink with a series of rectangular microchannels aligned in a parallel configuration. This microchannel heat sink was able to dissipate heat up to 790 W/cm^2 . One major advantage of using microchannel arrays in heat sinks is the large number of channels that can be placed in a fixed volume, resulting in a larger convective surface area than that of a single large channel in the same volume. The second major advantage is an increase in the fully developed heat transfer coefficient as the channel diameter is decreased. Even though single-phase flow through straight parallel microchannel heat sinks have been considered to be extremely effective for cooling, there are two potential disadvantages. The first disadvantage is an increase in pressure drop, for a given fluid flow rate, between the inlet and outlet of a microchannel as the diameter of the microchannel is decreased. Therefore, for a fixed flow rate, this higher pressure drop requires a higher pumping power to drive the working fluid through the microchannel. The second disadvantage is the potential for a non-uniform temperature distribution along the wall of the

channel between the channel inlet and outlet. For laminar flow in a microchannel subjected to a constant heat flux applied at the channel walls, the channel wall temperature monotonically increases in the direction of flow. A non-uniform temperature distribution at the interface between the heat sink and an electronic chip could result in permanent damage to the electronic chip.

Two-phase flow boiling in straight parallel microchannels was proposed to take advantage of latent energy exchange, allowing for more heat dissipation than with single-phase flow for the same flow rate. Another advantage to boiling flow heat transfer, depending upon the pressure drop across the channels, is the potential for a more uniform wall temperature distribution, resulting from a smaller difference in bulk fluid temperature between the inlet and exit of the channel. Unfortunately, as was the case for single-phase heat transfer, there are two major disadvantages associated with two-phase boiling flow. For example, for identical flow rates and applied heat fluxes but different inlet fluid temperatures, two-phase flows result in significantly higher pressure drop than do single-phase flows. This is primarily due to the presence of flow acceleration resulting from the dense liquid phase changing to a less dense vapor phase. Also, instabilities inherent to flow boiling may result in flow maldistribution in a parallel array of straight channels, which can affect the overall performance of a heat sink.

To address the increase in pressure drop drawback inherent to single-phase flows in straight parallel microchannels, fractal-like branching channel networks were proposed by Pence (2000, 2002). A representative fractal-like flow network is

provided in Fig. 1.1. The fractal-like flow network proposed by Pence (2000)

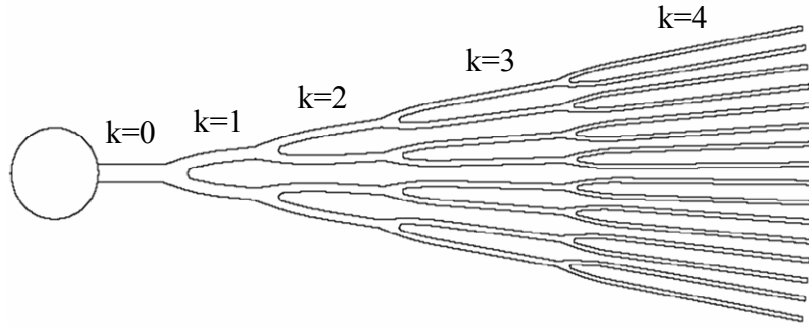


Figure 1.1. Fractal-like branching flow network

is based on fixed length and diameter ratios, ratios that were observed by West et al. (1997) to be constant in a number of naturally occurring flow networks. Using existing one-dimensional pressure drop and heat transfer correlations for macroscopic flows, Pence (2002) concluded that one major advantage of the fractal-like branching channel network for single-phase flows is a lower pressure drop than through an array of straight parallel microchannels subjected to the same applied heat flux and flow rate. In this comparison the convective surface area, channel length and hydraulic diameter of the channel exit were assumed identical between the two types of flow networks. Use of larger diameter channels for part of the network reduces the total pressure drop, because the pressure drop is inversely proportional to the diameter raised to the fourth power for a fixed mass flow rate. Another advantage to using the fractal-like branching channel network is the opportunity for a reduction in streamwise wall temperature variations due to the presence of redeveloping thermal boundary layers.

Daniels et al. (2005) modified the one-dimensional, single-phase, developing

flow model of Pence (2002) to predict pressure drop for two-phase diabatic flow through fractal-like branching networks. This one-dimensional, two-phase model assumes separated flow conditions. It was used to predict and compare both pressure drop and flow power in straight parallel channels and in fractal-like branching channels. As was also demonstrated in Pence (2002), both the pressure drop and flow power in fractal-like branching channels is lower than in straight parallel channels having the same convective surface area, same channel length and same exit channel dimensions.

A logical follow-on study would be to validate the one-dimensional, two-phase pressure drop model by Daniels et al. (2005), as was done by Kwak (2003) and Alharbi et al. (2003 and 2004) for the one-dimensional, single-phase model by Pence (2002). As a first step in this validation process, a study of gas-liquid flows is proposed. This is can be justified because as a number of void fraction correlations used for two-phase boiling flow, including the correlation used in the model of Daniels et al. (2005), were developed using gas-liquid flow data.

The objectives of the present study were (1) to generate two-phase gas-liquid flow pattern maps for each branching level and compare these to existing flow regime maps for similar channel dimensions and (2) to measure void fractions midstream of each branching level and compare these to results from existing correlations. Void fraction was assessed using two-different techniques. One technique for assessing void fraction is based on two-dimensional images acquired from a high-speed-high-resolution movie camera. Analyzing the resulting two-dimensional images as area-

based void fractions (versus the properly defined void fraction based on volume) may yield over-predicted estimates of void fraction, particularly in deep channels. The other option to the HSHR imaging is to project three-dimensional bubbles based on interfacial curvature of the bubble. For the present study, the former option is used. The second technique for assessing void fraction is based on a relationship, presented in Collier and Thome (1996), between void fraction and slip ratio. Slip ratio is defined simply as the gas velocity divided by the liquid velocity. As the liquid velocity varies considerably in the cross-section of a channel, the averaged liquid velocity, acquired using microscale Particle Image Velocimetry (μ PIV), is used in the slip ratio. The average interfacial velocity at the centerline of the channel is used to represent the gas phase velocity.

CHAPTER 2

LITERATURE REVIEW

In this section, review of single-phase and two-phase flows in parallel microchannel and in fractal-like branching microchannel networks are presented. Micro-particle image velocimetry (micro-PIV) studies are also reviewed with an emphasis on new techniques for image processing and on difficulties encountered using micro-PIV for velocity measurements, in both single-phase and two-phase flows.

2.1 Straight Microchannel Flows

Significant enhancement in mass and thermal transport is a primary reason for utilizing microscale channels. The goal of the current research, void fraction correlation validation or development, is an intermediate step in the development and validation of an optimization tool for designing branching channel heat sinks for two-phase heat transfer applications. Therefore, the following literature review includes references to heat transfer applications, even though the present research consists of an adiabatic gas-liquid flow study.

2.1.1 Single-phase flow

Using single-phase liquid water flowing in the laminar regime, Tuckerman and Pease (1981) were the first to investigate a microchannel heat sink for cooling very-large scaled integrated (VLSI) circuits. In their theoretical analysis, thermal resistance was separated into three parts, conductive, convective and advective, with convection providing the highest thermal resistance. The theory was experimentally tested in a silicon heat sink using an array of 100 straight parallel microchannels. Each channel was 50 μm wide and 300 μm deep with a center-to-center space of 100 μm . A maximum temperature rise of 71°C above the inlet water temperature was measured at the exit of the heat sink for a flow rate of 8.6 cm^3/s and a power density of 790 W/cm^2 applied at the surface of the heat sink. Theoretical and experimental data were in good agreement.

A number of single-phase investigations followed the initial investigation by Tuckerman and Pease (1981) in which are reported a wide range of conclusions regarding the Reynolds number transition to turbulence as well as the applicability of macroscale correlations for microscale applications. To address these reported discrepancies, Obot (2000) and Sobhan and Garimella (2001) reviewed the literature on single-phase flow and heat transfer in microchannels. It was concluded that due to insufficient evidence of the contrary, microchannel flows are governed by the same principles as are conventional or macroscale flows. In these review articles, causes for reported discrepancies include differences in experimental conditions among the various investigations such as surface roughness, instrumentation uncertainty,

uncertainty and non-uniformity in channel dimensions and placement of instrumentation.

2.1.2 Two-phase boiling flow

Two-phase boiling flow heat transfer coefficients with Freon R11 and with HCFC123 were studied experimentally in a single smooth 1.96 mm inner diameter copper tube by Bao et al. (2000). A range of parameters were tested, including heat fluxes between 5 kW/m^2 and 200 kW/m^2 , pressures between 200 kPa and 500 kPa and mass fluxes between $50 \text{ kg/m}^2\text{-s}$ and $1800 \text{ kg/m}^2\text{-s}$. Because the boiling heat transfer coefficient did not dependent significantly on either mass flux or vapor quality, but did have a strong positive relationship with heat flux and system pressure, it was concluded that nucleate boiling, as opposed to convective boiling, dominated heat transfer in this minichannel.

In a fundamental study of flow boiling heat transfer and flow pattern identification conducted by Steinke and Kandlikar (2004), a heat sink with six straight parallel channels was employed. The channels, 57 mm long, $214 \text{ }\mu\text{m}$ wide by $200 \text{ }\mu\text{m}$ deep and at a $570 \text{ }\mu\text{m}$ center-to-center spacing, were fabricated in copper with a polycarbonate cover. For the working fluid, deionized and degassed water was used. The experiment was conducted with mass fluxes and heat fluxes, respectively, ranging from 157 to $1,782 \text{ kg/m}^2\text{-s}$ and from 5 to 930 kW/m^2 . In all cases, the inlet temperature was held fixed at 22°C . Except at qualities near zero, the boiling heat transfer coefficient was observed to decrease with increasing exit vapor quality. Based

on macroscale two-phase boiling flow trends, nucleate boiling was concluded to be the dominant mechanism for flow boiling heat transfer.

Qu and Mudawar (2003) also observed a decrease in boiling heat transfer with increasing exit quality. However, it was concluded that although the trends do not follow those of convective dominated heat transfer at the macroscale, the primary flow regime identified was annular flow; therefore, the heat transfer was dominated by convective boiling. In this investigation, a copper heat sink with 21 straight parallel microchannels, 4.48 cm long, 231 μm wide by 713 μm deep and spaced at approximately 475 μm center-to-center and a Lexan cover was used. De-ionized water was used as the working fluid with inlet temperatures ranging from 30°C to 60°C and mass fluxes varying between 135 $\text{kg}/\text{m}^2\text{-s}$ and 402 $\text{kg}/\text{m}^2\text{-s}$.

Wang et al. (2005) experimentally investigated flow boiling heat transfer characteristics of R134a in a mini-tube with an inner diameter of 1.3 mm. Ranges of heat flux from 21 to 50 kW/m^2 , mass fluxes from 310 to 806 $\text{kg}/\text{m}^2\text{-s}$ and saturation pressures from 6.5 to 7.5 bar were studied. The heat transfer coefficient was observed to increase with increasing saturation pressure and increasing heat flux, a trend consistent with nucleate boiling dominated heat transfer for macroscale flows. However, for applied heat flux values less than 30 kW/m^2 , the boiling heat transfer coefficient was observed to increase with increases in exit vapor quality, a trend consistent with convective boiling dominated heat transfer for macroscale flows. Unsatisfied with either convective or nucleate dominated heat transfer, thin film evaporation, a microchannel heat transfer mechanism proposed by Jacobi and Thome

(2002), was suggested as a possible rationale for their observations.

In Jacobi and Thome (2002), contrary to conventional macroscale flow boiling in which nucleate boiling is the dominant mode of heat transfer, thin film evaporation into an elongated bubbles is suggested as the dominant mechanism of heat transfer in microscale flow boiling. A growing elongated bubble, sandwiched between two liquid slugs, was assumed for the two-zone model. Dupont et al. (2004a-b) extended the two-zone model to a three-zone model. The first, second and third zones, respectively, are a liquid slug, an elongated evaporating bubble surround by a thin liquid film, and a region of dry out following the elongated bubble. This three-zone flow boiling model was compared to a variety of experimental heat transfer coefficient data from several papers and found to predict the experimental data to within 67 % +/- 30 %.

2.1.3 Two-phase, gas-liquid flow

Many adiabatic gas-liquid flow studies in microchannels have focused on flow regime maps, typically comparing microchannel flow regimes to existing flow regime maps developed using macroscale flow geometries. One of the more frequently referenced macroscale flow regime maps is that of Taitel and Dukler (1976), in which a theoretical model for predicting transitions between two-phase flow regimes in pipe flow was developed and presented. Using this model, individualized maps for a specific channel size, fluid properties, and inclination angle can be developed for a range of gas and liquid flow conditions. Five different flow patterns are defined in the

model: stratified wavy, intermittent, dispersed bubble, stratified smooth and annular dispersed liquid. Taitel and Duklar (1976) used experimental data from several studies of gas-liquid flows in channels with diameters that ranged from 1.25 cm to 5 cm to compare with model predictions. The model predicted the observed experimental flow regime transitions with good agreement.

Triplett, et al. (1999a and 1999b) conducted an experimental study of air-water, two-phase flows in microchannels. Flow regime maps and two-phase pressure drop and void fraction results in circular and “semi-triangular” cross-section microchannels were presented in Triplett (1999a) and (1999b), respectively. Channel diameters ranged between 1.1 mm and 1.45 mm for the circular cross-section microchannels, with a similar range of hydraulic diameters, between 1.09 mm and 1.49 mm, for the semi-triangular microchannels. The superficial velocities for gas and liquid were varied, respectively, between 0.02 m/s and 80 m/s and between 0.02 m/s and 8 m/s. Except for the transition between slug flow and stratified flow, the Taitel and Dukler (1976) model agreed well with experimentally observed flow regimes (Triplett, 1999a). In Triplett (1999b), experimental void fraction data were compared to a variety of homogeneous and separated flow correlations and experimental pressure drop was compared to models using the same void fraction correlations. Both the experimental void fraction and the experimental pressure drop were best predicted in bubbly and slug flow regimes when the homogeneous flow correlation was used. However, for annular flow conditions in microchannels, use of the homogeneous void fraction correlation resulted in over predictions in both void fraction and pressure drop.

It was concluded that the interfacial momentum transfer for annular flows may be significantly different in microchannels from that in macroscale channels.

A gas-liquid, two-phase study in small diameter microchannels was conducted by Serizawa et al. (2002). Using a mixture of air and water in circular tubes between 20 μm and 100 μm in diameter, superficial liquid and gas velocities were varied from 3 mm/s to 17.5 m/s and from 1.2 mm/s to 295 m/s, respectively. The experimental void fraction data in the 20 μm diameter tube well matched those predicted by the Armand (1946) correlation (as reported in the Russian-to-English translation of Armand (1946) by Beak (1959)), which was developed from data in macroscale tubes. Comparison of experimental void fraction from the other tube diameters to the Armand and Treschev (1946) correlation are not provided.

Nitrogen-water, two-phase flow pattern and void fraction studies were conducted by Xiong and Chung (2007) in rectangular microchannels with hydraulic diameters varying between 0.21 mm and 0.62 mm. Nitrogen superficial velocities were varied from 0.06 m/s to 72.3 m/s whereas the superficial velocities of water ranged from 0.02 m/s to 7.13 m/s. In the larger hydraulic diameter channels of 0.41 mm and 0.62 mm, four different flow patterns were observed and include bubbly slug, slug-ring, dispersed-churn and annular flows. However, in the 0.21 mm size channel, only slug and annular flows were observed. These observations are similar to earlier observations in circular cross-section channels by the same group.

For example, in an earlier investigation, Chung and Kawaji (2004) studied the difference in two-phase flow between microchannels versus minichannels. Nitrogen

and water were mixed and injected into four different circular cross-section microchannels having diameters of 50 μm , 100 μm , 250 μm and 530 μm . Two-phase flow patterns, void fractions and pressure drop for each microchannel diameter were reported. Consistent with their later work, as was reported above, bubbly slug, slug-ring, dispersed-churn and annular flow patterns were observed in the larger circular tubes of 250 μm and 530 μm diameter,. Experimental void fraction was well predicted by the Armand (1946) correlation. In the 50 μm and 100 μm diameter circular tubes slug flow was the dominant flow pattern, and the void fraction data showed little agreement with predictions from the homogeneous model. Based on these observations, a new void fraction correlation was developed for microchannels.

In a simultaneous study, Chung, et al. (2004), investigated the effect of channel geometry on two-phase flow for a single microchannel diameter. A 96 μm square cross-section microchannel was employed in this study and compared with the results for the 100 μm diameter circular tube used in Chung and Kawaji (2004). The two-phase flow patterns and transition maps of the two channels were very similar; however, the transition between the slug-ring and ring-slug regimes was slightly shifted to higher superficial liquid and gas velocities. The measured void fraction in the circular and square channels was also very similar to each other, and best predicted using the model referred to in Chung and Kawaji (2004).

2.2 Fractal-Like Branching Microchannel Flow

Based on studies of bifurcating flow networks found in nature, such as the circulatory and respiratory systems of mammals and the vascular system of plants, West et al. (1997) proposed scaling ratios to characterize the change in duct size prior to and following a bifurcation.

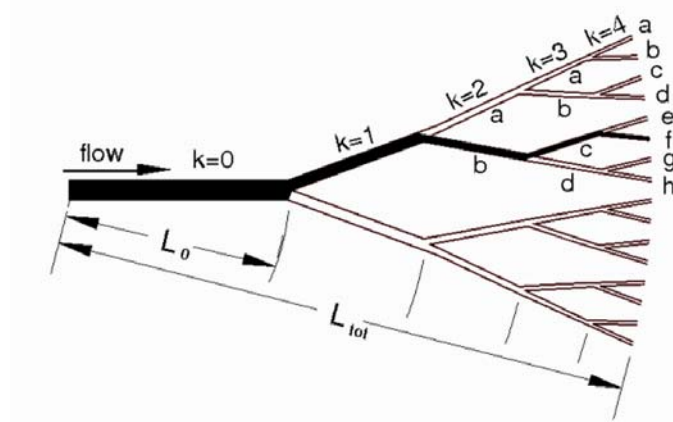


Figure 2.1. Label of each branch with channel geometry (Pence (2000))

Based on fixed length and diameter scaling relations, as were suggested in West et al. (1997), Pence (2000) was the first to introduce use of fractal-like branching channel networks in heat sinks. For ease of fabrication, a disk-shaped heat sink was proposed, with a representative flow network and flow direction shown in Fig. 1.1. In this initial study, the downstream to upstream length ratio and hydraulic diameter ratio were fixed at 0.707 and 0.794, respectively. Results from this study suggested that fractal-like heat sinks have two major advantages over parallel channel heat sinks,

these being the potential for a smaller total increase in streamwise wall temperature and a lower pressure drop between the inlet and exit of the flow network.

Pence (2002) continued the investigation of fractal-like branching microchannel flow networks and implemented a one-dimensional laminar flow model for predicting wall surface temperature and pressure distributions along fractal-like flow networks. Simultaneously developing thermal and hydrodynamic boundary layers were considered in the analysis to account for the newly formed walls following each bifurcation. A 60% lower pressure drop and a 30°C lower maximum wall temperature were reported for a fractal-like flow network than for a parallel array of straight channels subjected to the same applied heat flux, total channel length, convective surface area, exit channel flow area and pumping power. As a network analysis, versus a heat sink analysis, was conducted, energy was applied directly to the walls of the networks.

Alharbi, et al. (2003 and 2004) developed a three-dimensional CFD model to assess fluid flow (2003) and heat transfer (2004) in a heat sink having the branching network shown in Fig. 1.1. The results were used to validate the one-dimensional model proposed by Pence (2002), which was subsequently used in an optimization study by Enfield et al. (2005) and Heymann et al. (2008). Although the one-dimensional model was founded to slightly over-predict the pressure drop compared with the three-dimensional model, primarily due to the ability of the three-dimensional model to resolve the pressure recovery occurring at a bifurcation, this was a consistent observation. In general the one-dimensional and three-dimensional model results

exhibited very similar and consistent trends in both wall surface temperature and the pressure distribution, validating its use for design optimization.

In a parametric study by Pence and Enfield (2004), it was determined that for most applications, in which fixed channel depths would most likely be used, fractal-like flow designs based on fixed width ratios versus fixed hydraulic diameter ratios are more relevant. It was also noted that pressure drop is minimized for a small length scale ratios near 0.7, fortuitously that used in previous investigations, and larger length scale ratios, those near 1.4, result for optimal single-phase heat transfer applications. A width scale ratio close to 0.7 was determined optimal for both heat transfer and pressure drop. These fractal-like ratios are noted in Equations 2.1 through 2.3 below, with Equation 2.2 optimal for low pressure drop applications and Equation 2.3 optimal for single-phase heat transfer applications. In all three equations, n is equal to 2, which represents the number of downstream branches.

$$\frac{W_{k+1}}{W_k} = n^{-1/2} \quad (2.1)$$

$$\frac{L_{k+1}}{L_k} = n^{-1/2} \quad (2.2)$$

$$\frac{L_{k+1}}{L_k} = n^{1/2} \quad (2.3)$$

Daniels et al. (2005) extended the one-dimensional model of Pence (2002) to include a theoretical study of two-phase boiling flow pressure drop for a variety of flow networks. In Daniels et al. (2006), this same model was employed to predict the pressure distribution of adiabatic boiling flow in fractal-like branching channels.

Finally, Cullion et al. (2006 and 2007) reported preliminary data of void fraction variations in two-phase boiling heat transfer in a fractal-like branching heat sink optimized for minimal pressure drop.

In contrast to the repeated geometric-based pattern of fractal-like flow networks, Bejan (1997) developed constructal theory. In constructal theory, the construction of a flow network begins with the smallest volume known as a construct with a goal of filling an entire volume with as many constructs as possible. Two flow networks between one point and many points were constructed in Bejan (1997). One was optimized to maximize conductive heat transfer through a body. The second flow network was optimized to minimize flow resistance. In both cases, the flow resistance was minimized while maintaining fixed mass flow rates and fluid volumes and assuming fully developed laminar flow in circular tubes.

Later, Wechsato, et al. (2002) studied an optimal network based on flow resistance for the disk-shaped configuration introduced by Pence (2000). Like in Pence (2000 and 2002), the flow network originates from one point at the center of the disk and ends at many points at the perimeter of the disk. Unlike the simple fixed length scale ratio imposed by fractal-like flow networks, ratios between downstream and upstream duct lengths are allowed to vary. The flow networks in Wechsato, et al. (2002) were developed using constructal theory while assuming fully developed laminar flow in circular cross-section tubes. It was concluded that the more complex the geometry, the better the performance because the flow resistance was decreased as the number of branching levels increased. For the disk-shaped heat sink, channels that

branch into two new channels (bifurcations) and into three new channels (trifurcations) were considered in the constructal investigation. Using three branches, the flow resistance was decreased by 3.2% from the resistance using two branches, when the size of the disk and the number of the channel outlets were held fixed.

In addition to the previously noted differences between fractal-like and constructal approaches to single-phase heat sink design, the fractal-like optimization algorithm (see Heymann, et al. (2008)) simultaneously considers a wide range of parameters under a range of fabrication and flow constraints to identify a single, optimal flow geometry for a specified disk size.

2.3 PIV and Bubble Velocity Measurements

Particle image velocimetry (PIV) is a well-known flow measurement technique used to measure velocity fields in a wide range of macroscale flows. As summarized in the review article by Adrian (1991), PIV is accomplished by seeding the flow tracer particles that are illuminated either by a pulsed or a continuous light sheet. Using a camera with either a mechanical or an electronic shutter, the position of the tracer particles can be double-exposed on a single image or recorded on two separated images with a known time interval. From the image pairs, the particle displacement can be estimated by statistical correlations. Knowledge of the particle displacement and the time over which this displacement occurs allows for assessment of the velocity field.

Santiago et al. (1998) first introduced particle image velocimetry to microfluidics (micro-PIV). A Hele-Shaw flow field around a 30 μm diameter cylindrical post was studied. Deionized water was used as the working fluid and the flow rate was such that the Reynolds number was much less than unity. The micro-PIV system utilized an epi-fluorescent microscope, 100-300 nm spherical fluorescent particles, a continuous Hg-arc lamp, and a charge-coupled device (CCD) camera to obtain high-resolution images of the particle field. Introduced in this work was the use of the focal depth of an epi-fluorescent microscope instead of a light sheet typically used in macro-scale PIV. The system was limited to low Reynolds number flows due to the long duration of exposure of the CCD camera.

Meinhart, et al. (1999) improved the micro-PIV capabilities of Santiago, et al. (1998) to a one μm spatial resolution capable of measuring a velocity of approximately eight mm/s. They used an inverted epi-fluorescent microscope, a five ns pulsed Nd:YAG laser, 200 nm spherical diameter fluorescent particles, and a cooled interline-transfer CCD camera with 500 ns interval time between two exposures. The test section consisted of a rectangular glass channel with a depth of 30 μm . Two modifications that were implemented to achieve the one μm spatial resolution include a low seed density, as a means to minimize background noise in the flow field, and use of a time-averaging correlation method. This latter modification was necessary to provide sufficiently reliable signals from the particle, a problem introduced with a low seed density.. Using the average correlation method with low seed densities, micro-PIV measurements acquired at mid-depth of a rectangular channel well matched, within 2%, the analytical solution.

Three-dimensional micro-PIV measurements were made by Klank, et al. (2002) by adjusting the focal plane of the microscope lens by ten μm intervals to measure the flow field throughout the fluid depth of interest. The micro-PIV techniques of Meinhart, et al. (1999) were employed; however, there was no need to employ the average correlation method because the volume of the interrogation window contained a sufficient number of fluorescent particles. In this same study, time-resolved, three-dimensional micro-PIV measurements were considered using stereoscopic PIV techniques. The proposed technique included the use of two CCD cameras with significant overlap of the images and a stereo view angle of less than 6%.

Recently, Park, et al. (2004) proposed a three-dimensional micro-PIV measurement technique using a confocal laser-scanning microscope with a very small depth of focus. This technique was used to measure the flow field at multiple depths of creeping Poiseuille flow through a microtube. However, the low rotation speed of the disk with pin-holes inside the confocal microscope is the limiting factor in data acquisition, whereas the limiting factor in traditional PIV is generally the frame rate of the camera. Therefore, this technique is limited to extremely low flow rates. For example, a maximum Reynolds number flow of 0.003 and 0.02 in 99 μm and 516 μm inner diameter tubes, respectively, were investigated.

More recently, researchers have begun to measure two-phase flow fields inside a microchannel. Using micro-PIV, Wang, et al. (2004) reported the liquid velocity field measurements during bubble growth in a single, locally heated microchannel. The microchannel is etched in silicon, having a rectangular cross-section and hydraulic diameter of 140 μm . The study was conducted using a facility consisting of a mercury lamp, a 20x microscope objective, and a 12-bit interline cooled CCD camera with 1300 x 1040 pixel resolution. Fluorescent particles, 0.7 μm in diameter and a volume density of 0.025 %, were used as seed particles in the de-ionized water. To avoid seed particles from adhering to the walls of the microchannel, a 0.1% concentration of surfactant was used.

Polonsky et al. (1999) studied the shape of elongated bubbles and the leading and trailing interface velocities in macroscale two-phase flows. They diluted a very small amount of fluorescent dye (0.001%), whether by volume or by weight was not

indicated, in tap water to obtain a clear interface between the gas and liquid phases. A fluorescent dye is also being used in the present study for the same purpose. In 2005, Kitagawa et al. experimentally investigated the turbulence structure in a horizontal channel flow with gas microbubbles. Simultaneous measurement systems were used. Particle tracing velocimetry (PTV) and a shadow image technique (SIT) were employed to measure bubble velocity while PIV and laser-induced fluorescence (LIF) allowed for measurement of the liquid velocity field. The purpose of using LIF for measuring the liquid velocity field was to minimize light scatterings from the interface between liquid and bubbles.

Measurements of bubble velocity inside glass microchannels were recently acquired by Revellin et al. (2008). Using R134-a as a working fluid in a 500 μm circular cross-section microtubes. Two streamwise staggered lasers, at a known distance, were used for measuring bubble velocity. The lasers were directed through the middle of the microtube and coincident with two photo detectors located on the opposite side of the microchannel. The two photo detectors captured the intensity of laser light, which varied with the presence of vapor and liquid. Use of two lasers allows for both bubble length as well as bubble velocity to be ascertained.

CHAPTER 3

EXPERIMENTAL FACILITY

To gain a better understanding of two-phase gas-liquid flows in a fractal-like branching microchannel network, flow regime maps and void fraction at each branching level are of interest and proposed in this study. Two means of assessing void fraction will be used. One will be based on visual observations of flow whereas the second will involve use of the velocity slip ratio. To determine two-phase flow regimes for mapping purposes and to visually assess void fraction, high-speed-high-resolution (HSHR) imaging will be used. Micro-particle image velocimetry (micro-PIV) will be used to determine the average liquid velocity for use in the slip ratio. The micro-PIV camera will also be used to measure interface velocities. In this chapter, the test device, flow loop and instrumentation are discussed.

3.1 Test Devices

For studying gas-liquid, two-phase flow in a fractal-like branching channel with micro-PIV and HSHR imaging systems, the primary design requirement of the test device is the need for a transparent top surface for introduction of the light from

the laser and halogen light sources. Simultaneously, the transparent top allows for observing the fluoresced light from particles and the dye in the flow.

A fractal-like branching channel network pattern was dry reactive ion etched (DRIE) into a 38 mm diameter silicon wafer to a depth of 250 μm . A Pyrex[®] glass was anodically bonded to the silicon disk, forming the top surface of the channels and allowing for two-phase flow through the network to be observed. Figure 3.1 and Table 3.1 show the pattern of the fractal-like branching network and the channel dimensions, respectively. The flow pattern was designed using the following fixed length and diameter ratio:

$$\gamma = \frac{L_{k+1}}{L_k} = 2^{+1/2} \quad (2.1)$$

$$\beta = \frac{W_{k+1}}{W_k} = 2^{-1/2} \quad (2.2)$$

The water-air mixture enters the flow channels by way of the 2 mm diameter inlet plenum located at the center of the disk. The two-phase mixture then flows through the fractal-like flow network toward the periphery of the disk.

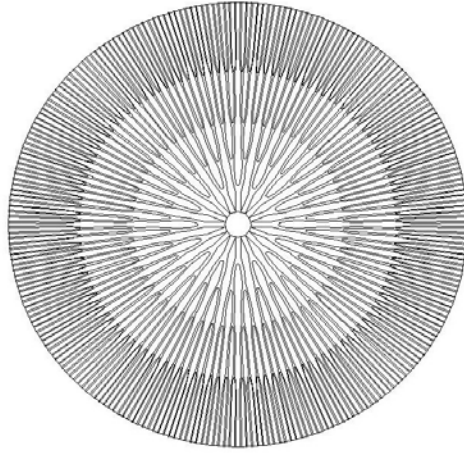


Figure 3.1. Fractal-like branching channel pattern with $\gamma = 1.414$.

Table 3.1. Channel dimensions

k level	No. of branch	Depth (μm)	Width (μm)	D_h (μm)	Length (mm)
0	16	250	400	308	1.6
1	32	250	283	265	2.27
2	64	250	200	222	3.21
3	128	250	141	180	4.54
4	256	250	100	143	6.42

3.2 Manifold

A manifold was designed to direct the two-phase mixture of air and water to the inlet of the test section and to collect and separate, through gravity, the two phases exiting the test section. Figure 3.2a shows the manifold designed and fabricated for use in a previous investigation, and which is more fully explained in Cullion (2005). To hold the test device in place and to provide a leak proof fluid interconnect at the inlet of the test section, the manifold was designed using a vacuum chuck concept. Figure 3.2b shows this part of the manifold, which is here after referred to as the vacuum chuck. The vacuum chuck was machined from polyetheretherketone (PEEK), which has high tensile strength at high temperature of 250°C as well as high electrical and thermal resistances. An enlarged view of the top surface of the vacuum chuck is shown in Fig. 3.2c. A leak proof seal is achieved by placing the test device on top of the vacuum chuck followed by drawing a vacuum using a vacuum pump. The vacuum ports are via a conduit inside the vacuum manifold to a vacuum line shown in the side of the vacuum chuck in Fig. 3.2b. As the test device is pulled down, a seal between the o-rings and the fractal-like branching channel disk is achieved. The manifold was originally designed for microscale flow boiling study in fractal-like branching channel networks; hence the presence of pogo-pins. The pogo pins were not used for the current, adiabatic gas-liquid two-phase study.

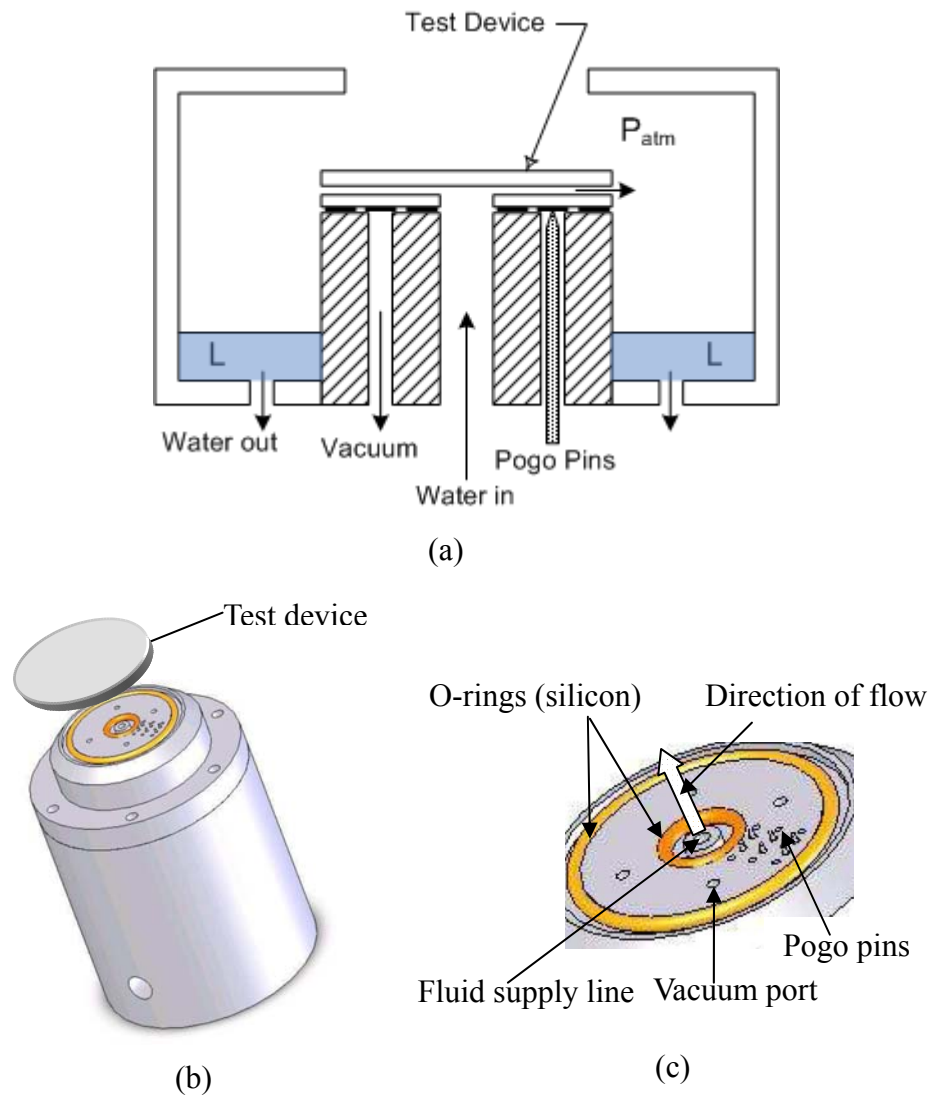


Figure 3.2. (a) Manifold and (b) vacuum chuck with (c) enlarged view of top surface of vacuum chuck (used, with permission, from Cullion (2005))

3.3 Flow Loop

The manifold is integrated in the flow loop, shown schematically in Fig. 3.3. Distilled, degassed and deionized water, seeded with fluorescent particles and dye, is pumped from a reservoir using a Tuthill® 0.11ML/REV micro-gear pump with a maximum flow rate of 126 g/min at 690 kPa. The micro-gear pump is controlled with a DC power supply with a maximum voltage limit of 24 volts. The water flow rate is adjustable via either or both the DC power supply and the needle valve located just downstream of the pump. Prior to injecting air into the water stream, the duct carrying the seeded water is sent through a Branson 2510DTH ultrasonic vibrator set at the maximum power of 130 W and a frequency of 40kHz. At the fastest flow rate used in the present study, this provided a residence time of 8 minutes for the seeded flow in the vibration bath. The purpose of the ultrasonic vibrator is to disperse any agglomerated fluorescent particles evenly in the flow. Just prior to being directed into the manifold, and ultimately into the test device, air is injected into the water stream at the gas injector, shown schematically in Fig. 3.4. To make the gas injector, a cone inside of the gas injector was machined from porous aluminum with an average pore size of 12 μm and average porosity of 15%. The gas injector design is similar in nature to that reported in Xiong and Chung (2007).

The air, supplied by a compressor, is regulated on either side of a surge tank used to damp pressure oscillations. The air is twice filtered, first with a 5 μm filter

prior to the surge tank and with a second 1 μm filter located downstream of the surge tank. The flow of air is controlled by a needle valve.

Flow rates of both the air and water are necessary for determining the superficial flow rates needed to prepare flow regime maps. A Micromotion Coriolis mass flow meter with a flow range of 0 to 1370 g/min and an accuracy of 0.10% of the flow rate is used to measure the inlet water mass flow rate. One of two Gilmont[®] flowmeters are used to measure the volumetric flow rate of the air with an uncertainty of $\pm 2\%$ of reading or \pm one scale division. To assess the mass flow rate of air requires an assessment of density at the volumetric flow meters. Therefore, the pressure and temperature of the air are measured by a Validyne[®] DP15 pressure transducer with an accuracy of $\pm 0.25\%$ of full scale and a T-type thermocouple with an accuracy of ± 1 $^{\circ}\text{C}$.

In addition to measuring the mass flow rates of the gas and liquid streams, the inlet temperature and pressure of the well-mixed gas-liquid two-phase flow are measured as it enters the manifold. Both inlet temperature and pressure are measurement at approximately 7 cm below the inlet of the test device. The inlet temperature is measured with a Therm-X[®], metal sheathed, 4 wires, resistance temperature detector (RTD) with an accuracy of 0.7 $^{\circ}\text{C}$. The inlet pressure is measured with a Kulite Semiconductor pressure transducer with a typical uncertainty in the voltage output of 0.1mV and a maximum sampling rate of 1400 kHz. The calibration curves and uncertainties of the above instruments are provided in Appendix D.

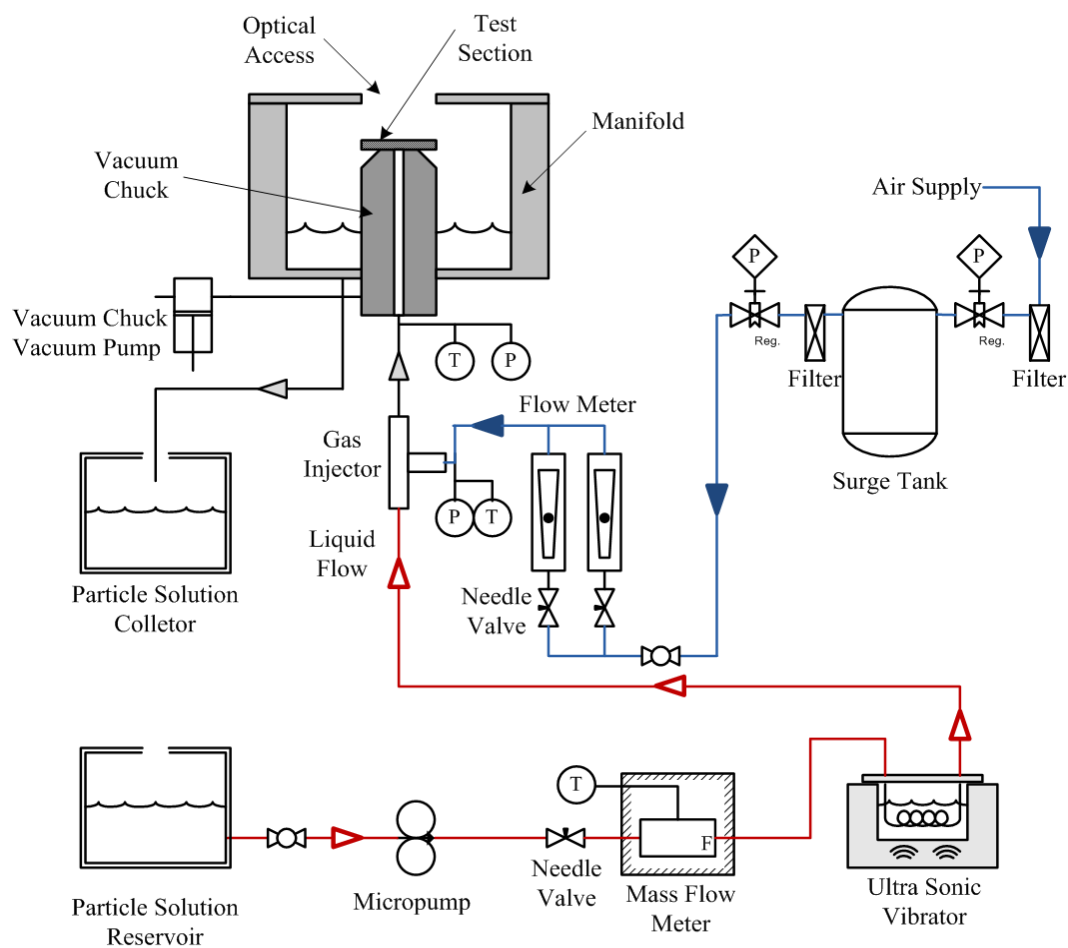


Figure 3.3. Schematic diagram of flow loop

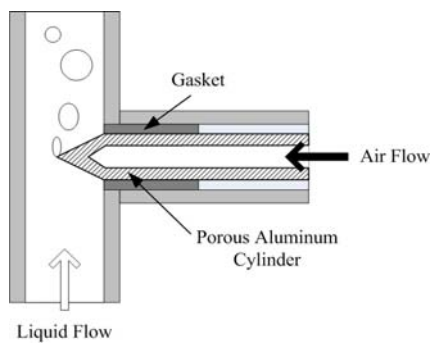


Figure 3.4. Schematic diagram of gas injector

3.4 High-Speed-High-Resolution (HSHR) Imaging System

To observe the two-phase flow patterns in the fractal-like branching microchannels, a high-speed-high-resolution (HSHR) imaging system, shown in Fig 3.5, is used. The HSHR camera is also used to visually assess the void fraction. Light from a halogen source is introduced through a fiber optic cable and a series of optics, including an expander, a diffuser, a dichroic mirror and a 10x microscope objective lens, and then into the test device. Two-phase flow images are recorded using a HSHR Vision Research Phantom[®] V.5 camera. This HSHR camera can record up to 60,000 fps at a resolution of 32x256 pixels and at 1,000 fps at the highest resolution of 1024x1024 pixels. The camera has a temporary memory storage capacity of one GB. Temporarily stored images are extracted and saved on a separate storage drive in Cineon image file format using the Phantom software supplied by manufacturer. These Cineon formatted images are converted to TIFF image format for image processing. The HSHR camera is controlled using a Dell[®] Inspiron 9200 laptop computer.

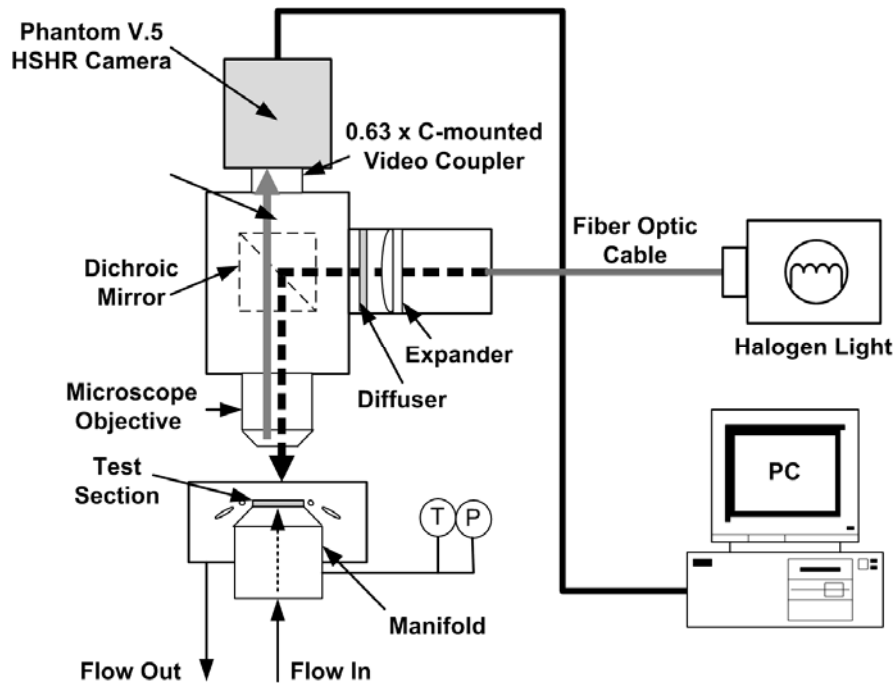


Figure 3.5. Schematic diagram of HSHR imaging system

3.5 Micro-PIV Setup

In general, PIV systems require a pulsed laser sheet, optics, a high-speed CCD camera with a full field image and a data acquisition system. The basic theory of micro-PIV is the same as PIV except for the manner in which lighting is introduced to create a depth of field in which the image is in focus. Micro-PIV uses front lighting, which is introduced into the test device in a direction parallel to the CCD camera, as opposed to a thin laser sheet provided in a plane perpendicular to the CCD camera, as is the case for traditional PIV. For micro-PIV a microscope objective and a dichroic mirror are needed to sufficiently magnify the flow field and to direct the laser beam

toward the test section, respectively. A schematic diagram of a micro-PIV setup used in the present study is shown in Fig. 3.6. The main components of the system, including laser, optics, camera, and the hub as well as the fluid additives are discussed.

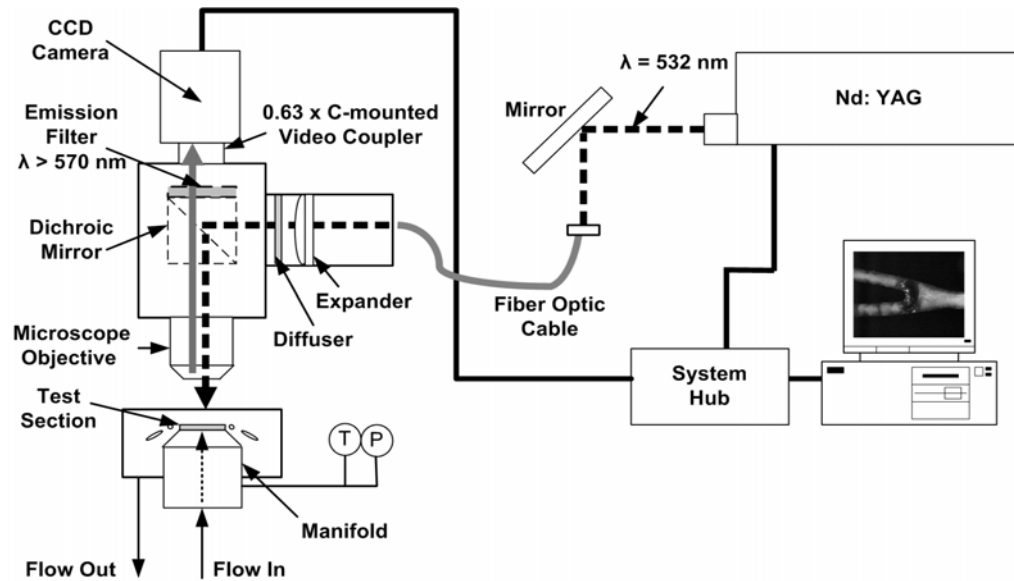


Figure 3.6. Schematic diagram of micro-PIV system

3.5.1 Laser

A double pulsed New Wave Solo PIV III-15 Nd:YAG laser with a major wavelength of 532 nm is used for illuminating both the fluorescent seed particles for fluid velocity measurements and the diluted fluorescent dye used to illuminate the liquid-gas interface. The maximum power and shortest dual pulse are 50 mJ/s and 3 ns, respectively.

3.5.2 Flow additives

The flow was seeded with 1.0 μm diameter fluorescent particles from Duke Scientific Co., catalog number R0100. Based on manufacturer specifications, the density of the fluorescent particles is 1.05 g/ml, which is very close to the 1 g/ml density of water at 20°C. The fluorescent particles came from the manufacturer diluted in a solution consisting of 1.8×10^{10} beads per milliliter of water. The excitation wavelength of the fluorescent particles is 542 nm, which is very close to the major wavelength of 532 nm supplied by the Nd:YAG laser. The emission wavelength of the fluorescent particles is 612 nm.

A Rhodamine B fluorescent dye with excitation and emission wavelengths of 526 nm and 580 nm, respectively, is added to the seeded water to a molarity of 6×10^{-8} . Recall that the purpose of the fluorescent dye is to illuminate and observe a clear interface between water and bubbles, but the concentration must be such that the intensity of fluorescent particles is not compromised. The wavelength spectra of the fluorescent micro-particles and Rhodamine B fluorescent dye are provided in Appendix A.

Finally, to avoid particle agglomeration and prevent attachment of the seed particles to the channel walls, a 0.01% volume concentration of the surfactant, Triton X-100 is added to the seeded water.

3.5.3 CCD Camera

A Hisense MK2 12bit CCD camera with a 1344x1024 pixel resolution and a 6.45x6.45 μm pixel pitch is part of the micro-PIV system. The pulse interval range of the CCD camera is as low as 300 ns, and its full frame rate is 12.2 Hz. The CCD camera and pulsed Nd:YAG laser are synchronized using a Dantec[®] system hub.

3.5.4 Optics

Leitz[®] PLAN 10x and a 20x objectives are used to obtain expansive and focused images. For general observations, the 10x objective is used. For a higher magnification and a more refined depth of field measurement, the 20x objective is used.

Meinhart, et al. (1999) discussed the total depth of field, δz , which is the visible range that gives a clear particle image throughout the optical measurement system. The equation used to assess the total depth of field is

$$\delta z = \frac{n\lambda}{NA^2} + \frac{ne}{M \cdot NA} \quad (3.3)$$

where

$$NA = n \sin(\theta) \quad (3.4)$$

For the present optical measurement system, the index of refraction, n , of air, the medium between the micro-fluidic device and the objective lens is 1.003, the wavelength of the light emitted from the fluorescent particles, λ , is approximately 600 nm, and the average pixel spacing of the CCD camera, e , is 6.45 μm . The total

magnification, M , varies with the microscope objective. For the 10x and 20x objectives with a 0.63x reducer, the total magnification is 6.3 and 12.6, respectively. In assessing the numerical aperture, NA, using Eq. 3.4, θ represents the angle between the surface normal and the edge of the objective lens, as shown in Fig. 3.7. Also shown in this figure are the aperture diameter, working distance, focal plane, and depth of focus.

The numerical apertures (NA) for the 10x and 20x objectives are 0.25 and 0.4, respectively, yielding a depth of focus of approximately 14 μm for the 10x objective and approximately 5 μm for the 20x objective

A 570 nm optical emission filter is used for filtering out wavelengths below 570nm. Higher wavelengths, including the 612 nm and 580 nm wavelengths emitted from the fluoresced particles and the Rhodamine B dye, respectively, are allowed to pass through the emission filter, the video coupler and into the CCD camera.

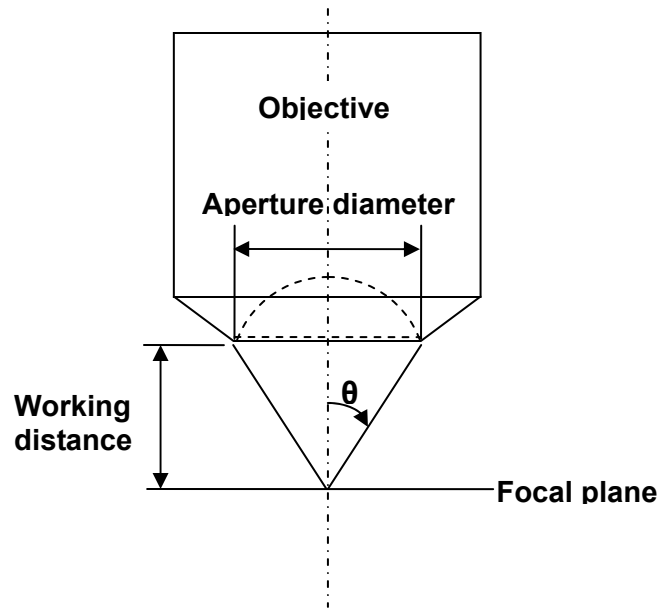


Figure 3.7. Schematic diagram of microscope objective

3.5.5 Dantec[®] System Hub

Dantec[®] system hub connects the laser and camera with the computer and provides a means for synchronizing the laser pulse with the camera exposure time. The system hub is capable of storing 1.5 Gb of images in temporary memory. The Dantec[®] system hub is controlled by the computer via setting parameters in Dantec Flow Manager[®], a software package supplied by the manufacturer of the hub that also has PIV analysis tools that were used for the present study.

CHAPTER 4

FLOW REGIME MAPS AND VOID FRACTION CORRELATIONS

In this chapter, two-phase gas-liquid flow regime maps, generated using the theoretical model developed by Taitel and Duklar (1976), for each level of the fractal-like branching flow network are presented. Using the two-phase flow regime maps, test plans for both HSHR imaging and micro-PIV experiments are devised. In addition, two different methods for assessing void fraction are discussed, as are the correlations to which the experimental void fraction results will be compared in Chapter 6.

4.1 Flow Regime Maps

4.1.1 Theoretical flow map generation

Using the theoretical model by Taitel and Dukler (1976), two-phase liquid-gas flow regimes at each level in the fractal-like branching channel network were generated as a function of superficial gas and liquid flow rates. This mathematical model is based on physical concepts to determine transition lines between the various flow regimes as a function of channel diameter, fluid properties, and orientation of the flow relative to gravity. In this model, five different two-phase flow regimes are assumed for macroscale flows: stratified smooth, stratified wavy, intermittent, dispersed bubble and annular dispersed liquid. Intermittent flow includes slug, plug

and elongated bubble flows.

In their model, Taitel and Dukler (1976) assume identical pressure drop in both the liquid and gas phase momentum balances, which for a horizontally oriented circular tube results in

$$\tau_{wg} \frac{S_g}{A_g} - \tau_{wf} \frac{S_f}{A_f} + \tau_i S_i \left(\frac{1}{A_f} + \frac{1}{A_g} \right) = 0 \quad (4.1)$$

where τ represents the shear stress and subscripts w, g, f and i represent wall, gas, liquid and the interface of gas-liquid phase, respectively. Additionally, S and A represent perimeters and cross-sectional area, respectively. The wall shear stresses for the gas phase, liquid phase, and the interfacial shear stress are

$$\tau_{wf} = f_f \frac{\rho_f u_f^2}{2} \quad \tau_{wg} = f_g \frac{\rho_g u_g^2}{2} \quad \tau_i = f_i \frac{\rho_g (u_g - u_i)^2}{2} \quad (4.2)$$

where variables f, ρ and u in Eq. 4.2 are friction factor, density and velocity, respectively. The friction factors for the gas phase and liquid phase are

$$f_f = C_f \left(\frac{D_{hf} u_f}{\nu_f} \right)^{-n} \quad f_i \approx f_g = C_g \left(\frac{D_{hg} u_g}{\nu_g} \right)^{-m} \quad (4.3)$$

and the interfacial friction factor is approximately equal to that of the gas phase, for gas velocities much larger than liquid velocities. In Eq. 4.3, D_h , ν , C, m and n represent hydraulic diameter, kinematic viscosity, friction factor coefficient and exponents for gas and liquid, respectively. For laminar flow conditions, C is equal to 16 and m and n are both set to unity, whereas for turbulent flows, C is set equal to 0.046 and m and n are both set equal to 0.2. Laminar and turbulent flows are

determined using Reynolds numbers based on actual velocities and hydraulic diameters of each phase.

Substituting Eqs. 4.2 and 4.3 into Eq. 4.1 and non-dimensionalizing yields

$$X_{LM}^2 \left[\left(\bar{u}_f \bar{D}_{hf} \right)^n \bar{u}_f^2 \frac{\bar{S}_f}{\bar{A}_f} \right] - \left[\left(\bar{u}_g \bar{D}_{hg} \right)^m \bar{u}_g^2 \left(\frac{\bar{S}_g}{\bar{A}_g} + \frac{\bar{S}_i}{\bar{A}_f} + \frac{\bar{S}_i}{\bar{A}_g} \right) \right] = 0 \quad (4.4)$$

where X_{LM} is a two-phase parameter introduced by Lockhart and Martinelli (1949). The overbars in Eq. 4.4 denote the non-dimensional form of a variable, where D , D^2 , j_f and j_g are used as scaling parameters. The Lockhart and Martinelli parameter is a ratio of superficial pressure drop of liquid over that of gas and is expressed as

$$X_{LM} = \left[\frac{\frac{4C_f}{D} \left(\frac{j_f D}{v_f} \right)^{-n} \frac{\rho_f (j_f)^2}{2}}{\frac{4C_g}{D} \left(\frac{j_g D}{v_g} \right)^{-m} \frac{\rho_g (j_g)^2}{2}} \right]^{1/2} = \left[\frac{\left(\frac{dP}{dx} \right)_f^s}{\left(\frac{dP}{dx} \right)_g^s} \right]^{1/2} \quad (4.5)$$

where j is superficial velocity, D is tube diameter, and $(dP/dx)^s$ is the pressure drop assuming the represented phase is flowing alone through the pipe.

Employing the Kelvin-Helmholtz stability theory, the authors developed stratified wavy to intermittent and stratified wavy to annular-dispersed liquid transition criteria based on a Froude number modified by a two-phase density ratio. The authors denote this dimensionless number as F . Likewise a dimensionless number, T , relating the turbulent forces to gravity forces is used as the transition criteria between intermittent and dispersed bubble regimes. The liquid height relative to the tube diameter ratio solely determines the transition between the annular-dispersed liquid regime and the dispersed bubble and intermittent regime, and is characterized

by a fixed Lockhart and Martinelli parameter. Although the transition between smooth stratified and wavy stratified flow is considered by Taitel and Dukler (1976), it is not considered in the present study due to the lack of reported smooth stratified flow regimes observed in microchannels. Each transition line is uniquely defined for a given X and F or T value, depending upon the transition regime.

Shown in Fig. 4.1 is a representative two-phase gas-liquid flow regime map for a horizontally oriented microtube. Stratified wavy flow, intermittent, dispersed bubble flow and annular dispersed liquid regimes are presented as a function of the Lockhart and Martinelli parameter on the abscissa versus one of the non-dimensional values, T or F .

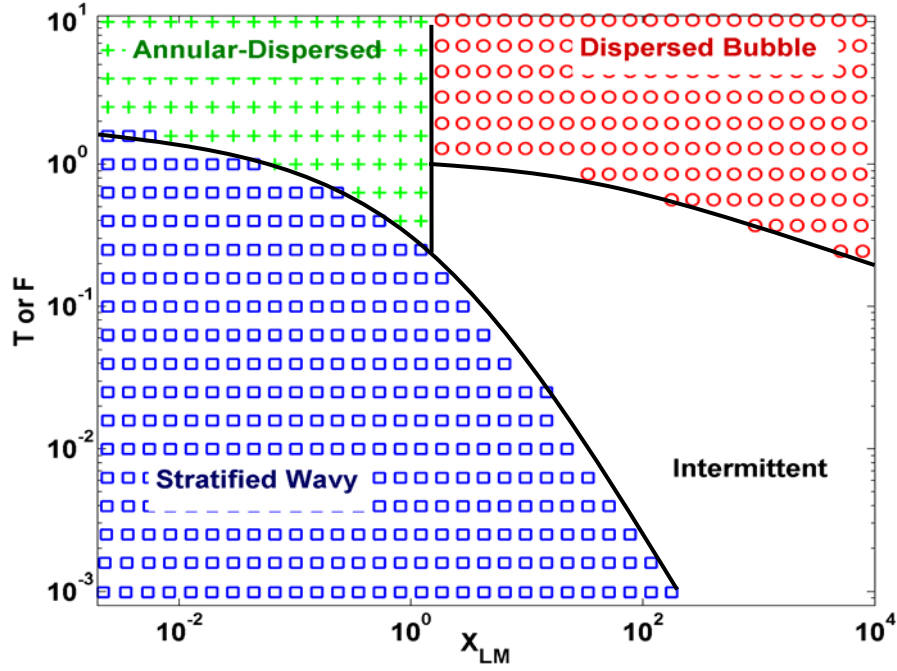


Figure 4.1. Representative non-dimensional two-phase gas-liquid flow regime map. Stratified wavy, annular dispersed, and dispersed bubble presented with symbols of blue squares, green crosses, red circles, respectively. The intermittent flow regime is blank.

Stratified wavy flow occurs when the following criterion is met:

$$F^2 \left[\frac{1}{(1 - \bar{h}_f)^2} \frac{\bar{u}_g \left(\sqrt{1 - (2\bar{h}_f - 1)^2} \right)}{\bar{A}_g} \right] < 1 \quad (4.6)$$

where $F = \sqrt{\frac{\rho_g}{(\rho_f - \rho_g)}} \frac{j_g}{\sqrt{Dg}}$ and $\bar{h}_f = h_f / D$

Intermittent flow occurs when the following three conditions are met:

$$F^2 \left[\frac{1}{(1 - \bar{h}_f)^2} \frac{\bar{u}_g \left(\sqrt{1 - (2\bar{h}_f - 1)^2} \right)}{\bar{A}_g} \right] \geq 1 \quad \& \quad \bar{h}_f \geq 0.5$$

$$\& T^2 < \left[\frac{8\bar{A}_g}{\bar{S}_i \bar{u}_f^2 (\bar{u}_f \bar{D}_f)^{-n}} \right] \quad (4.7)$$

$$\text{where } T = \left[\frac{\frac{4C_f}{D} \left(\frac{j_f D}{v_f} \right)^{-n} \frac{\rho_f j_f^2}{2}}{(\rho_f - \rho_g)g} \right]^{1/2}$$

For dispersed bubble flow, the mathematical criteria are

$$T^2 \geq \left[\frac{8\bar{A}_g}{\bar{S}_i \bar{u}_f^2 (\bar{u}_f \bar{D}_f)^{-n}} \right] \quad \& \quad \bar{h}_f \geq 0.5 \quad (4.8)$$

Finally, annular dispersed liquid flow occurs when

$$F^2 \left[\frac{1}{(1 - \bar{h}_f)^2} \frac{\bar{u}_g \left(\sqrt{1 - (2\bar{h}_f - 1)^2} \right)}{\bar{A}_g} \right] \geq 1 \quad \& \quad \bar{h}_f < 0.5 \quad (4.9)$$

The Matlab[®] code and flow chart used to generate flow regime maps are provided in Appendix B

4.1.2. HSHR and micro-PIV test plan

One test plan for generating flow regime maps and one for assessing void fraction correlations is needed. Ideally, a single test plan that covers all four flow regimes and spans a wide range of β ratios in each branch level is preferred. The ratio β is defined as the volumetric flow rate of the gas divided by the total volumetric flow rate of liquid plus gas. The flow regime map in Fig. 4.1 is rather inconvenient for

selecting gas and water mass flow rate ranges for a test plan. Rather, plotting the same criteria in Eqs. 4.6 through 4.9 on a superficial velocity axes allows for ease of selection of a test plan.

Flow regime maps under laminar-laminar, turbulent-laminar, laminar-turbulent, and turbulent-turbulent liquid-gas flow conditions were developed for each of the five branch levels: $k=0$ through 4. As will be shown in Chapter 6, the turbulent-turbulent maps best fit the experimental data; therefore, turbulent-turbulent maps for each branch level, based on the hydraulic diameters reported in Table 3.1, are provided in Fig. 4.2 and are used in developing a test plan. The two-phase flow regime maps in Fig. 4.2 are plotted on a log-log scale with liquid superficial velocity on the ordinate and superficial gas velocity on the abscissa.

In Fig. 4.2a, a flow regime map generated for the $k=0$ branch, three different liquid superficial velocities and four different air superficial velocities were identified that spanned three flow regimes. These twelve velocity combinations are plotted as black solid circles on the same figure. The lower limit of the superficial liquid velocity was set to maintain pump stability, i.e., constant liquid flow. The remaining superficial velocity limits were selected based on a desire to have (1) a wide range of homogenous flow rates for correlation assessment and (2) a wide range of flow regimes for map assessment. As the flow area at each downstream branch level increases, the superficial velocities identified in Fig. 4.2a also decrease with each branch level. The same velocity combinations in Fig. 4.2a are shown in Figs. 4.2b through 4.2e, but at their reduced value through that branch level. In the first three

branch levels, three different flow regimes are expected, with the stratified flow omitted. Only in the terminal branch level are all four flow regimes anticipated, with only one case expected to yield a stratified flow.

These twelve cases compose the test plan for the HSHR experiments, for purposes of identifying two-phase flow patterns and assessing void fractions using image processing. The test cases are listed in Table 4.1 based on superficial flow rates in the $k=0$ branch level. Those cases shown in italic font are also to be used for the micro-PIV and bubble velocity measurements necessary to determine the void fraction based on the slip ratio. Study of higher gas velocities was not possible due to foam generation at the disk periphery due to the presence of the surfactant in micro-PIV studies. In Chapter 6, experimental flow regime results from HSHR images are compared with the Taitel and Dukler model results and to other two-phase flow regime maps.

Table 4.1. Test plan for HSHR and micro-PIV experiments at $k=0$

	Superficial air velocity (m/s)			
Superficial liquid velocity (m/s)	0.007	0.014	0.104	1.80
0.42	Case 1 ($\beta=0.02$)	Case 6 ($\beta=0.03$)	Case 7 ($\beta=0.20$)	Case 12 ($\beta=0.82$)
0.21	Case 2 ($\beta=0.03$)	Case 5 ($\beta=0.06$)	Case 8 ($\beta=0.33$)	Case 11 ($\beta=0.90$)
0.05	Case 3 ($\beta=0.12$)	Case 4 ($\beta=0.21$)	Case 9 ($\beta=0.67$)	Case 10 ($\beta=0.97$)

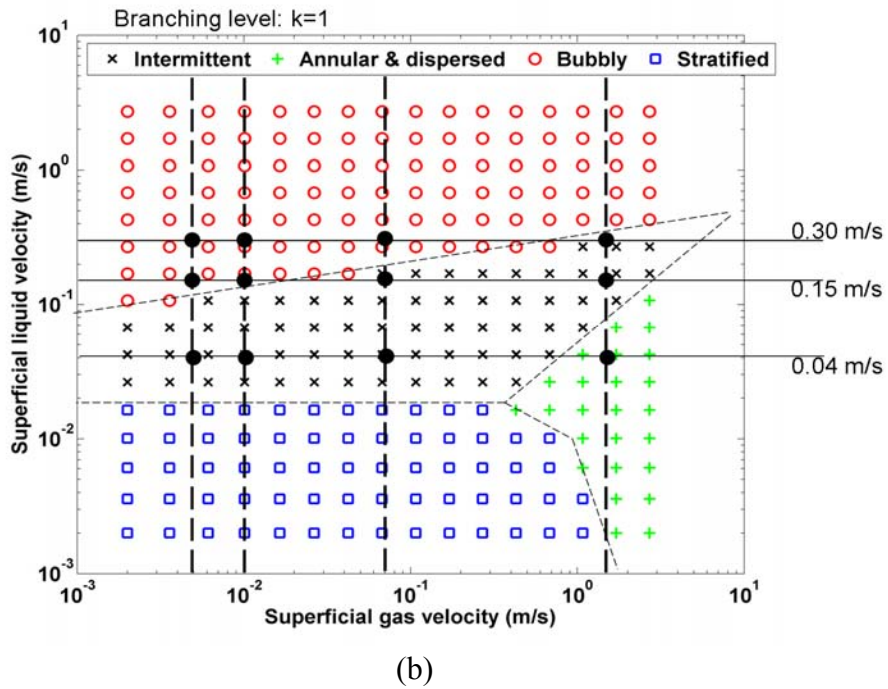
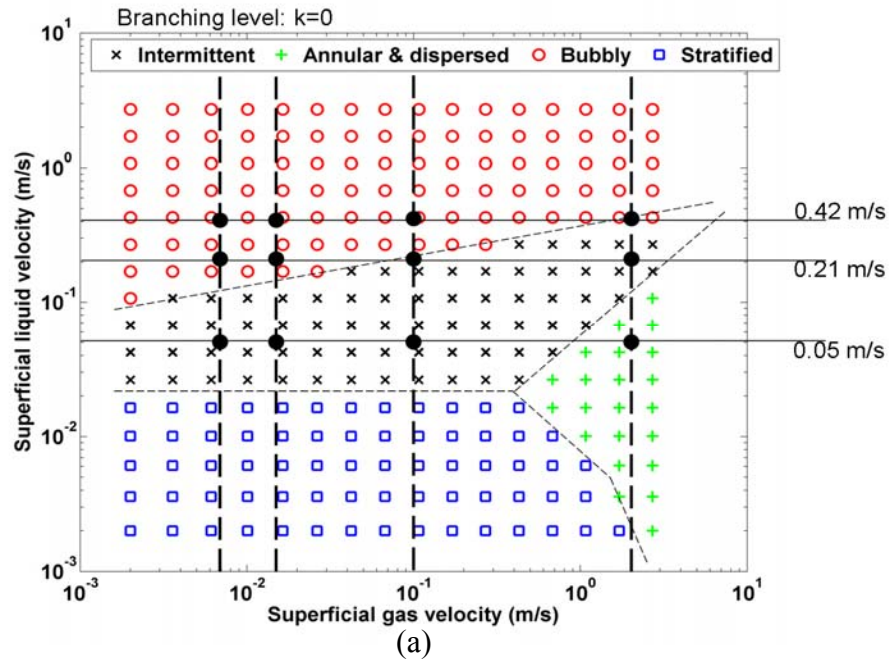


Figure 4.2: Two-phase flow regime maps for each branching level of k in the fractal-like branching channel networks. (a) at $k=0$ with $D_h=308 \mu\text{m}$, (b) at $k=1$ with $D_h=265 \mu\text{m}$.

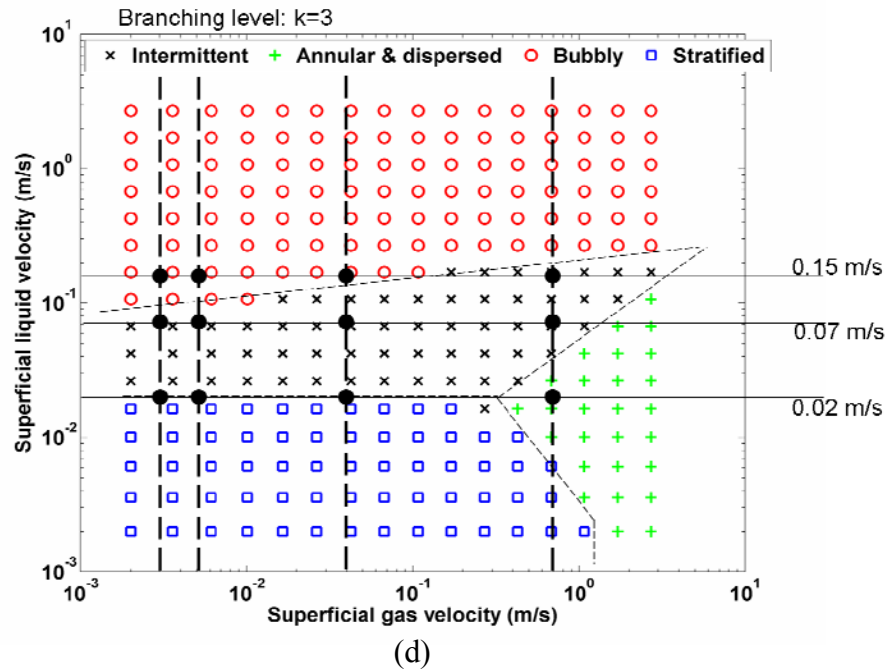
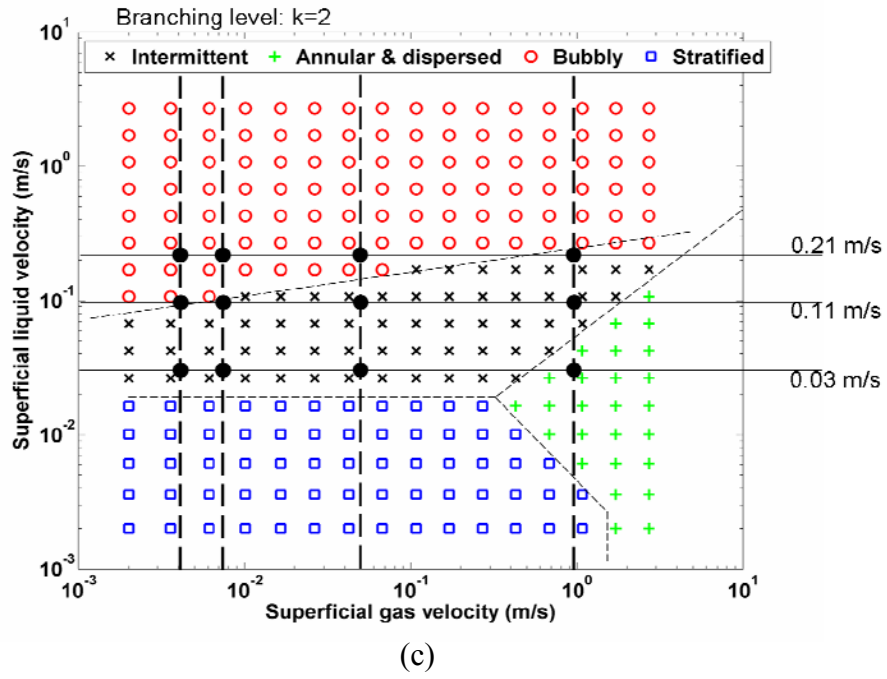


Figure 4.2. Two-phase flow regime maps for each branching level of k in the fractal-like branching channel networks. (c) at $k=2$ with $D_h=222 \mu\text{m}$, (d) at $k=3$ with $D_h=180 \mu\text{m}$.

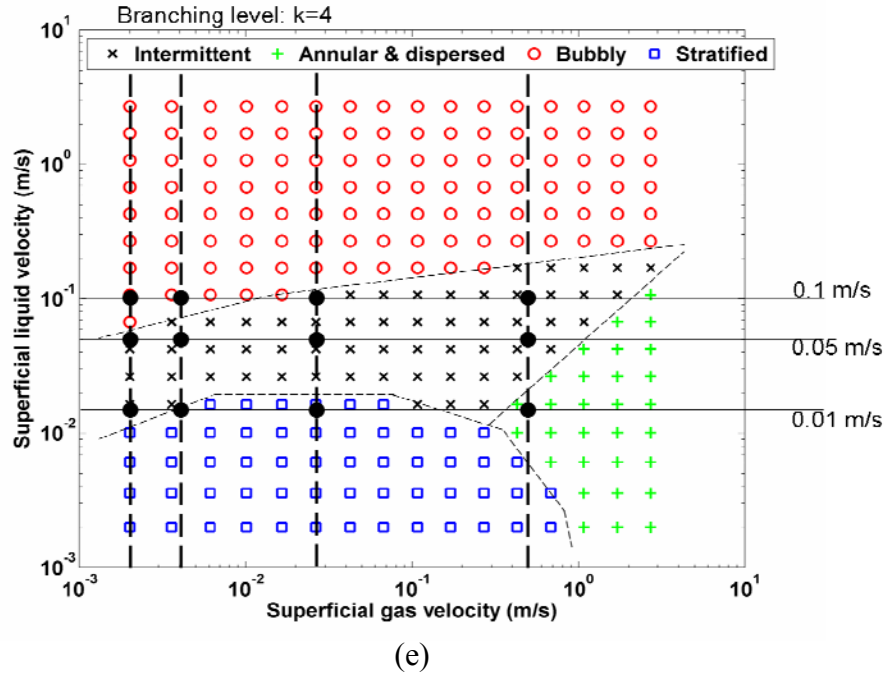


Figure 4.2. Two-phase flow regime maps for each branching level of k in the fractal-like branching channel networks. (e) at $k=4$ with $D_h=143 \mu\text{m}$.

4.2 Void Fraction

4.2.1 Void fraction based on slip ratio

Void fraction is defined as the ratio of gas volume to total volume, and can be expressed in terms of slip ratio. The slip ratio is defined as

$$\text{Slip ratio} = \frac{u_g}{u_f} \quad (4.10)$$

where u_g and u_f are the local gas and liquid velocities, respectively. The relationship between void fraction and slip ratio starts from the basic definition of slip ratio in Eq .4.10. Rewriting the velocities in the slip ratio in terms of mass flow rate, density

and void fraction yields

$$\frac{u_g}{u_f} = \frac{\dot{m}_g \rho_f (1 - \alpha)}{\dot{m}_f \rho_g \alpha} \quad (4.11)$$

Equation 4.11 rewritten in terms of void fraction is

$$\alpha_{slip} = \frac{1}{1 + \left(\frac{u_g}{u_f} \right) \left(\frac{1 - x}{x} \frac{\rho_g}{\rho_f} \right)} \quad (4.12)$$

where α_{slip} is void fraction computing from the slip ratio, and x represents quality.

Recall that quality is the ratio of the mass flow rate of gas over the total mass flow rate.

4.2.2 Void fraction based on HSHR images

As noted earlier, void fraction is defined as the volume ratio of gas to total volume. As HSHR images are two-dimensional, there are two options for assessing void. In both cases, a region is defined for each branch level near the center of the channel. The void in this region is averaged in space and over time, i.e., the spatially averaged void of a number of time sequenced images are again averaged. The first void assessment option is an area based averaged void fraction, in which case the ratio of the plan form area of gas to total area defining the channel is used. The second option is to project a three-dimensional bubble volume and relate it to the volume of the channel. The second option includes several assumptions about bubble depth. In the first option, all bubbles are assumed to span the depth of the channel. The first option is used in this investigation, with the understanding that these numbers may be slightly high.

4.2.3 Existing void fraction correlations

In Chapter 6, the void fractions computed from experimental slip ratio and image processing are plotted against homogeneous void fractions, where the homogenous void fraction is defined as the ratio between gas and total volumetric flow rates

$$\beta = \frac{Q_g}{Q_g + Q_f} = \frac{j_g}{j_g + j_f} = \frac{u_g \alpha}{u_g \alpha + u_f (1 - \alpha)} = \frac{x \rho_f}{x \rho_f + (1 - x) \rho_g} \quad (4.13)$$

In Chapter 6, experimental void fraction is also compared with predictions from the four existing void fraction correlations listed below;

$$\alpha = 0.833\beta \quad \text{Armand(1946)} \quad (4.14)$$

$$\alpha = \frac{1}{1 + \left(\frac{1-x}{x} \right) \left(\frac{v_f}{v_g} \right)^{\frac{2}{3}}} \quad \text{Zivi(1964)} \quad (4.15)$$

$$\alpha = \left[1 + \sqrt{1 - x \left(1 - \frac{\rho_f}{\rho_g} \right) \left(\frac{1-x}{x} \right) \left(\frac{\rho_g}{\rho_f} \right)} \right]^{-1} \quad \text{Chisholm (1973)} \quad (4.16)$$

$$\alpha = \frac{0.03\sqrt{\beta}}{1 - 0.97\sqrt{\beta}} \quad \text{Chung et al. (2003)} \quad (4.17)$$

The four void fraction correlations in Eq 4.14 through 4.17 are plotted in Fig. 4.3. The void fraction correlations of Armand (1946) and Zivi (1964) have similar trends in that they exhibit a fairly linear relationship between α and β . The correlations of Chisholm (1973) and Chung et al. (2004), on the other hand, exhibit an exponential increase in void fraction with increases in the homogeneous void fraction. Further discussion of

these trends and the means under which each correlation were developed are presented in Chapter 6 with the experimental results of the present study.

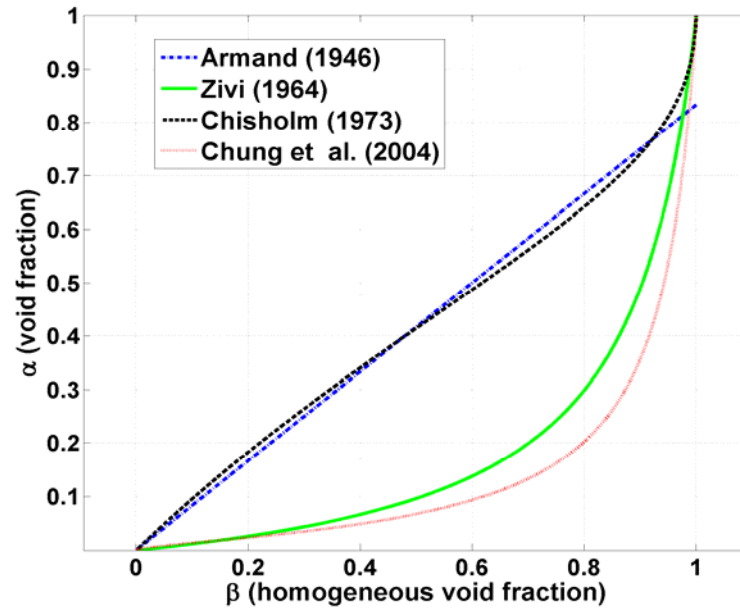


Figure 4.3. Void fraction versus homogeneous void fraction based on four different existing correlations.

CHAPTER 5

EXPERIMENTAL PROCEDURES AND DATA ANALYSIS

The detailed experimental procedures for acquiring global measurements, and high-speed-high-resolution (HSHR) and micro particle image velocimetry (micro-PIV) images are discussed in the first half of this chapter. In the second half of the chapter, data analyses of void fraction, assessed using the slip ratio and using area averaged two-dimensional flow images, are discussed. In the previous chapter, Chapter 4, slip ratio was defined as gas velocity over liquid velocity and was proposed (originally by Collier and Thome et al. (1996)) as a means to determine void fraction. For slip ratio assessment, average liquid and gas velocities are necessary and are determined by micro-PIV velocity analysis and image analysis, respectively.

5.1 Experimental Procedure

5.1.1 Global measurements

Volumetric flow rate of the air was measured upstream of the gas injector. This was accomplished using a rotometer. To convert this volumetric flow rate to mass flow rate, the air pressure and temperature were measured just downstream of the rotometer in order to calculate density. The pressure and temperature were recorded at 200 Hz, for 5 seconds, and were replicated 2000 times. The flow rate of water was measured using a Coriolis mass flow meter. The frequency setting of this instrument

was used due to the low liquid flow rates studied. This mode provides the highest accuracy for low flow rates. In frequency mode, a “gate” is opened for five seconds and the frequency is measured and translated to a mass flow rate based on a manufacturer supplied calibration curve.

5.1.2 HSHR imaging

Two important preparations prior to conducting experiments were necessary. First, the solution was prepared by mixing deionized and distilled water with surfactant at a volume concentration of 0.01% and black food dye at a volume concentration of 0.08%. Use of the surfactant, Triton[®] X-100, and the black food dye were for creating identical liquid properties as those used for the micro-PIV experiments and for improving image contrast to observe the liquid-gas interfaces in the fractal-like branching network, respectively. The second important preparation was cleaning of the test device. Prior to each experimental run, the fractal device was cleaned by soaking in laboratory grade isopropyl alcohol for one day followed by several rinses with deionized water. The test device was then placed in a beaker filled with deionized water and cleaned using ultrasonic vibration for approximately 10 seconds followed by another flush with deionized water. This last process was repeated four times. The cleaned test device was then set on the vacuum chuck in the manifold, which was connected to a vacuum pump used to draw air from between the O-ring seals and the disk, as was discussed in Chapter 3. The prepared liquid solution was driven into the test device by a micro-pump in the flow loop and adjusted using a

needle valve to the desired liquid flow rate.

The building air was first filtered by a 5 μm pneumatic air filter prior to its arrival in a surge tank at approximately 410 kPa. The compressed, filtered air was then driven through a 1 μm size air filter before reaching the rotometers. Two rotometers were used. One was for a lower gas range from 0.046 ml/min to 8.821 ml/min and the other for a higher flow range from 3.440 ml/min to 312.1 ml/min. If a high gas flow rate was desired, the gas flow could be easily switched from the lower to higher range rotometer by turning on or off valves. The flow loop was run for approximately 40 minutes to stabilize the flow rate, a time determined sufficient from a running average of global measurement data.

The HSHR imaging system was usually prepared while the flow was being stabilized. A video coupler of 0.63X magnification was attached to the front of the HSHR camera. The video coupler has male C-mount threads, which allowed for installation on the HSHR camera. The video coupler and HSHR camera were placed on top of the microscope. A micro-objective lens with 10x magnification was used to view two-phase flow in all levels in the fractal-like flow network. A 20x objective lens was also used in the acquisition of flow higher resolution images in the $k=3$ and $k=4$ branch levels.

Acquiring images was controlled by Phantom[®] software that came with the HSHR camera and was loaded on the laptop. The Phantom[®] software was set at the slowest frame rate of 20 frames per second (fps), with two different fields of view. One field of view was set to 1024x512 pixels for acquiring images from the branch

levels between $k=0$ and $k=3$. Except for the $k=0$ branch level, this 1024x512 pixel field of view included a pair of branching channels. For the $k=4$ branch level, a different field of view covered a pair of branching channels. This field of view, 1024x256 pixels, is half that used for $k=0$ through $k=3$ branch levels. It should be noted that the pixel resolution for each objective remained fixed, regardless of the field of view setting. These resolutions were 1 μm per pixel for the 10x objective and 2 μm per pixel for the 20x objective.

The locations at which HSHR images were acquired are shown in Fig. 5.1. A field of view, shown as a black box and approximately to scale, is located near the middle of each branch level.

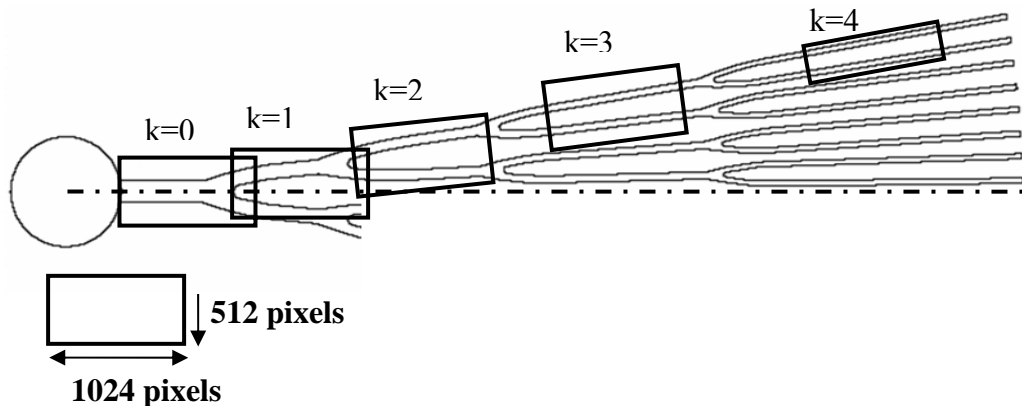


Figure 5.1. Locations for acquiring HSHR images for each branching channel level

To maintain a consistent focal plane at the mid-depth of the channel during repositioning of the camera along the fractal-like channel network, it was necessary to level the test device before taking image data. A bubble level on top of the test device served this purpose. The test device was set parallel to the base of the microscope

using a level adjustment stage attached to an x-y translation stage. Small imperfections on the Pyrex surface of test device were used as focal points in this alignment process.

A total of 2038 images at a frame rate of 20 fps were taken for each of the $k=0$ through $k=3$ branch levels for each flow condition. For the $k=4$ branch level, 4076 images were taken. The smaller image size of the 1024x256 pixel field of view allowed twice as many images to fit into the fixed temporary memory of the camera. In total, twelve different flow rate conditions were studied, using the test plan provided in Table 4.1.

5.1.3 Micro-PIV imaging

For micro-PIV imaging, a solution of water with fluorescent microspheres, surfactant and fluorescent dye was prepared. Fluorescent spherical microbeads on the order of 1 μm in diameter were well mixed with deionized water at a volumetric seed density of 0.02%. For preventing fluorescent particle agglomeration during the experiments, Triton X-100 surfactant was added to the particle solution prepared above at a 0.01% volumetric concentration. Rhodamine B was added at a molarity of 6×10^{-8} and used for creating better contrast between liquid and gas phases for image processing.

The Nd:YAG laser used in the study required a warm up period of approximately 30 minutes to reach consistent full power. The same procedures for liquid and gas flow loop preparation and setup as were discussed for image acquisition were also used for micro-PIV acquisition, except for the preparation of liquid solution.

In addition, for micro-PIV, a long pass optical filter was installed inside of microscope and located right before the video coupler shown in Fig. 3.6. The long pass filter filters out wavelengths lower than 570 nm. The HSHR camera discussed above was replaced with the MK II Hisense PIV camera. The same 0.63x video coupler was installed as discussed previously. Leveling of the test device and focusing on the mid-depth of each microchannel were also accomplished as discussed previously. Both 10x and 20x microscope objectives were used for acquiring micro-PIV image data. The details are discussed below.

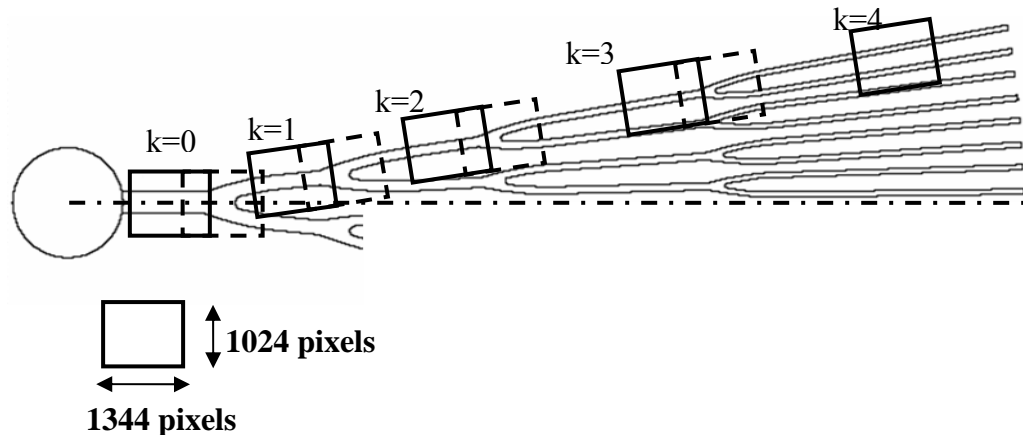


Figure 5.2. Locations for acquiring PIV images for each branching channel level

The PIV camera was connected to the Dantec[®] system hub, which was used to synchronize and trigger the Nd:YAG laser and PIV camera. The system hub was controlled by Flow Manager software, which came with the Dantec[®] PIV system. The time interval between sequential images was computed for each flow condition using an average particle displacement of 5 pixels. For measuring interfacial velocities, the time interval was set to achieve an approximate 100-pixel displacement of the bubble,

assuming the bubbles to travel at the same velocity of the liquid, i.e., homogeneous flow behavior. The laser power was set to 19 mJ/pulse and the external trigger option was selected. A total of 500 sequential PIV images were taken at five different channel levels (solid boxes in Fig. 5.2) and four different bifurcation sections (dashed boxes in Fig. 5.2) for each flow condition with the 10x microscope objective lens. Using the 20x microscope objective lens, another 500 sequential images were taken for the k=3 and k=4 branch levels to achieve higher spatial liquid velocity resolution. For measuring the interface (or bubble) velocities, 500 sequential images were taken for each branch level.

5.2 Data Analysis

5.2.1 Data reduction of global measurements

Superficial velocities are needed for generation of flow regime maps, whereas flow qualities and phase densities are needed to assess the homogenous void fraction used in void fraction correlations. Flow quality, defined as the ratio of the mass flow rate of air over the total combined air and water mass flow rates, is

$$x = \frac{\dot{m}_g}{\dot{m}_g + \dot{m}_f} \quad (5.1)$$

The mass flow rate of water was measured directly, but the volumetric flow rate of the air was measured using a rotometer. As rotometers are greatly affected by the operating pressure, the values read from the flow meter require modification. The

modification equation supplied by Gilmont, the manufacturer of the rotometer, requires the pressure and temperature of the gas measured just downstream of the meter, i.e., at the gas injector. The correction equation is

$$Q_{gi} = Q_{gm} \sqrt{\frac{P_{gm}}{760} \frac{530}{T_{gm}}} \quad (5.2)$$

where Q, P and T are the volumetric flow rate, pressure and temperature, respectively, in units of ml/min, mm of Hg and °R. Subscripts gi and gm refer to gas at the gas injector and gas at the meter.

To assess the actual gas flow rate at the test device, Q_g , requires a mass balance between the gas injector and the inlet of the test device,

$$\dot{m}_g = \rho_g Q_g = \rho_{gi} Q_{gi} \quad (5.3)$$

where ρ represents density and subscript g denotes gas at the inlet of the test device. As the temperature and the pressure of the two-phase mixture is not known at the inlet of the test device, neither is the density known at this location. However, an average of the pressure, hence average density, between the inlet of the manifold and the exit of the test device should provide a good estimate. Air densities at the gas injector, inlet to the manifold and exit of the test device were calculated assuming ideal gas behavior

$$\rho = \frac{PM}{RT} \quad (5.4)$$

and 25°C. For the record, the largest measured pressure drop between the manifold inlet and the device exit was 5 kPa, resulting in an inlet pressure estimate of 2.5 kPa. Using the ideal gas equation of state, a 2.5 kPa pressure yields a density value of 0.03

kg/m³. Therefore, if the inlet pressure estimate was 100% off, i.e., the true pressure at the inlet of the device was actually 5 kPa rather than the estimated 2.5 kPa, the maximum error in the inlet density calculated from the ideal gas relation is about 2.5%

Superficial velocity of a phase is the velocity that would exist if the total flow rate of that phase passed through the total channel cross-sectional flow area. Assuming a fixed total mass flow rate through each of the branching levels, the superficial velocities through each branch, k , can be computed from

$$j_{f,k} = \frac{\dot{m}_f}{\rho_f N_k H_k W_k} \quad \& \quad j_{gk} = \frac{\dot{m}_g}{\rho_g N_k H_k W_k} \quad (5.5)$$

where

$$N_k = 16(2^k) \quad (5.6)$$

The coefficient 16 in Eq. 5.6 represents the number of $k=0$ branches at the inlet plenum, and H and W are the channel depths and widths, respectively. The total flow rates in Eq. 5.5 are those entering the manifold; hence entering the inlet of the test device.

Recall the definition of homogenous void fraction from Eq. 4.13, repeated here for convenience,

$$\beta = \frac{x\rho_f}{x\rho_f + (1-x)\rho_g} \quad (5.7)$$

Water density, ρ_f , at standard temperature and pressure was assumed, i.e., 997 kg/m³.

Finally, the slip ratio

$$Slip\ ratio = \frac{u_g}{u_f} \quad (5.8)$$

used in

$$\alpha_{slip} = \frac{1}{1 + \left(\frac{u_g}{u_f} \right) \left(\frac{1-x}{x} \frac{\rho_g}{\rho_f} \right)} \quad (5.9)$$

requires knowledge of the local liquid and gas velocities. These data reduction techniques are discussed in sections 5.2.3 ad 5.2.4, respectively.

5.2.2 Data reduction from HSHR images

HSHR images were analyzed using the Image Processing Toolbox in Matlab[®]. As a first step, the area over which the void fraction was to be determined was defined. This was accomplished by taking one image that was completely filled with deionized water from the 2038 (or 4076) images in a movie at each level for each flow condition. This same image was also used as a “base image”, the purpose of which is discussed shortly. To define the region of interest, this selected image was loaded into an image processing code, written in Matlab[®] by a fellow student, Douglas Heymann and modified slightly from Heymann et al. (2007), and converted to a black and white image using the following Matlab capabilities and functions: histogram equalization, two-dimensional noise removal filter, image complement, image fill, median filter and a user defined black and white threshold level. These steps are shown in Fig. 5.3 as they occur to the base image in Fig. 5.3(a).

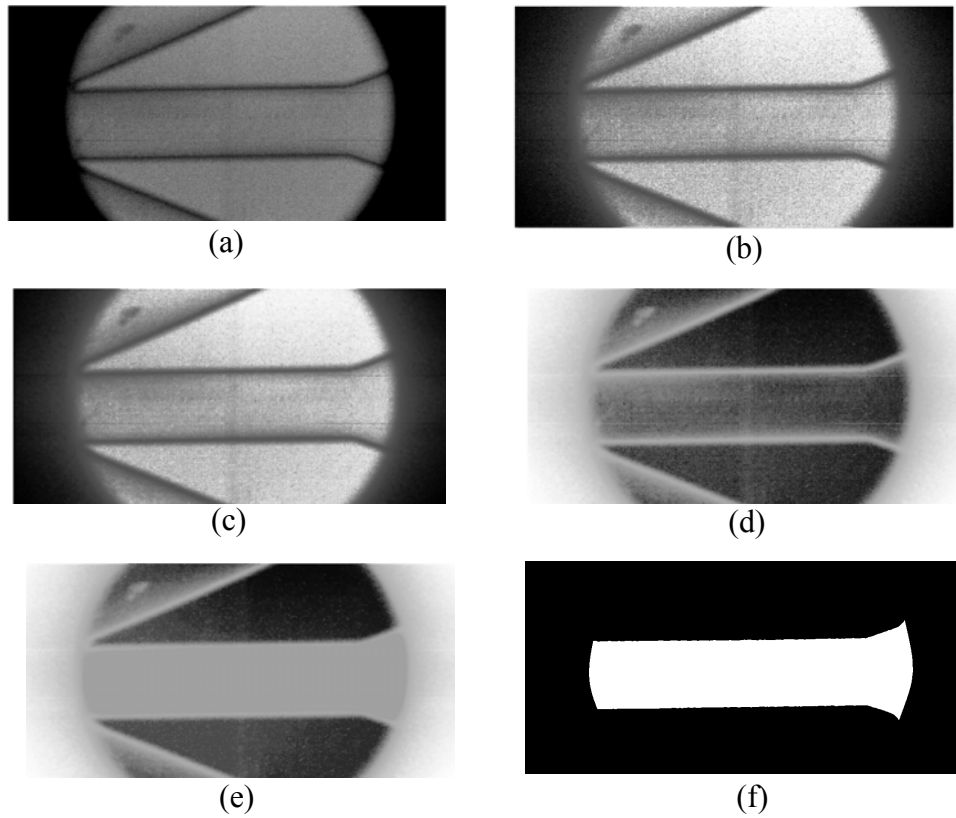


Figure 5.3. Image process for base image for $k=0$ branching level. (a) original image with liquid only, (b) used contrast enhancement, (c) used noise remove filter, (d) image complement, (e) filling darker pixels inside channel region are brightened, (f) binary image.

Figure 5.3a shows an original image taken by HSHR camera that is completely filled with water. The histogram equalization filter works to enhance the contrast of the image, as is observed from Fig. 5.3b. Two-dimensional noise removal and median filters were used for minimizing noise on the grayscale and binary images. See Fig. 5.3c. Image processing Matlab[®] functions called image complement (imcomplement) and image fill (imfill) were also used in analysis of the base image. The image complement function inverts gray scale intensities, i.e., black and white

intensities to opposite intensities of white and black, as is noted in Fig. 5.3d. The image fill function replaces an area of dark pixels inside the channel with lighter pixels, as can be observed in Fig. 5.3e. Finally, applying the black and white threshold level, a clear definition of the region of interest for image processing is created, as observed in Fig. 5.3f.

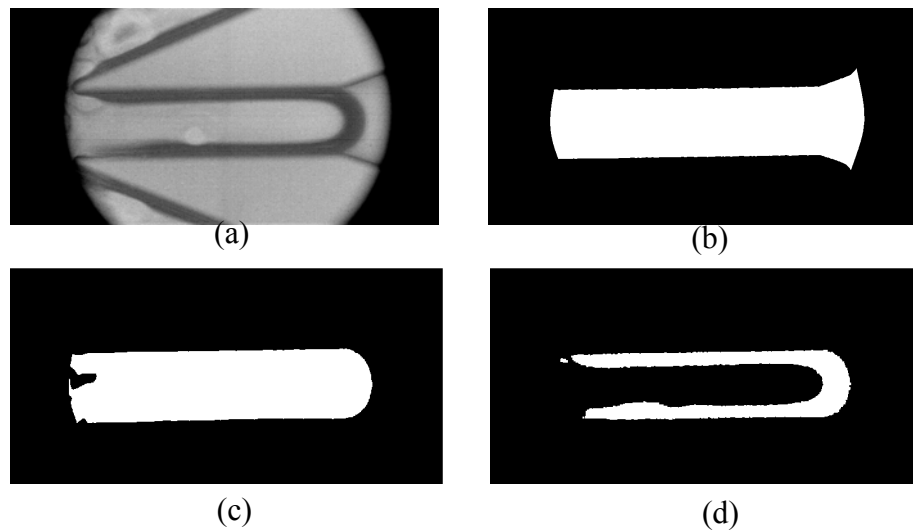


Figure 5.4. Image process for creating binary two-phase flow images to determine area averaged void fraction. (a) original image, (b) base image, (c) binary image for bubble only, (d) binary image for liquid film only.

To process each image in a movie sequence for void analysis, the base image is subtracted from the image under investigation. If no bubble is present, the image under investigation and the base image should have the same pixel intensity. When subtracted, there should be a null value of intensity at each pixel. However, if a bubble is present, pixel intensities between the base image and the image under investigation will differ and result in a non-zero value upon subtraction. These non-zero values for

gas and zero values for liquid allow bubble detection. If necessary, the resulting image is enhanced with contrast enhancement and filter options prior to binarization, at which point gas is displayed as white pixels and water as black pixels. Because the bubble is known to have a degree of curvature, the threshold value plays a significant role in how the bubble is defined. For example, a bubble is clearly obvious in Fig. 5.4a. Depending upon the intensity of the image corresponding with the center of the bubble, a certain threshold value may yield a solid white area defining a bubble, as is observed in Fig. 5.4c. Using a different threshold level, the dark region observed around the bubble in Fig. 5.4a shows up similar to Fig. 5.4d. Sometimes, simple thresholding is not sufficient to define the bubble as it should be defined, e.g., as in Fig. 5.4c. In this case it is necessary to close and fill the bubble outline in Fig. 5.4d.

In addition to providing a means of defining a bubble, the outline in Fig. 5.4d, which represents the curvature of the bubble or liquid film thickness surrounding the bubble, provides an opportunity to correct the apparent or two-dimensional void fraction assessments. Figure 5.5 provide a schematic diagram of a bubble in a channel in an effort to explain the presence of the dark region around bubble that is observed in Fig. 5.4a. Figure 5.5 is also used explain how this region

of curvature will be in void fraction assessment. Physically, the dark region is caused by light reflections at the curvature of the interface between gas and liquid phases. The light reflections at the curved gas-liquid interface differ from the reflections of liquid phase only or when the liquid film between a bubble and the Pyrex surface is flat. Figure 5.5a and 5.5b represent side and cross-sectional views, respectively, of a

rectangular microchannel with a representative bubble present. Included in these figures are representative light reflections at the gas-liquid interface.

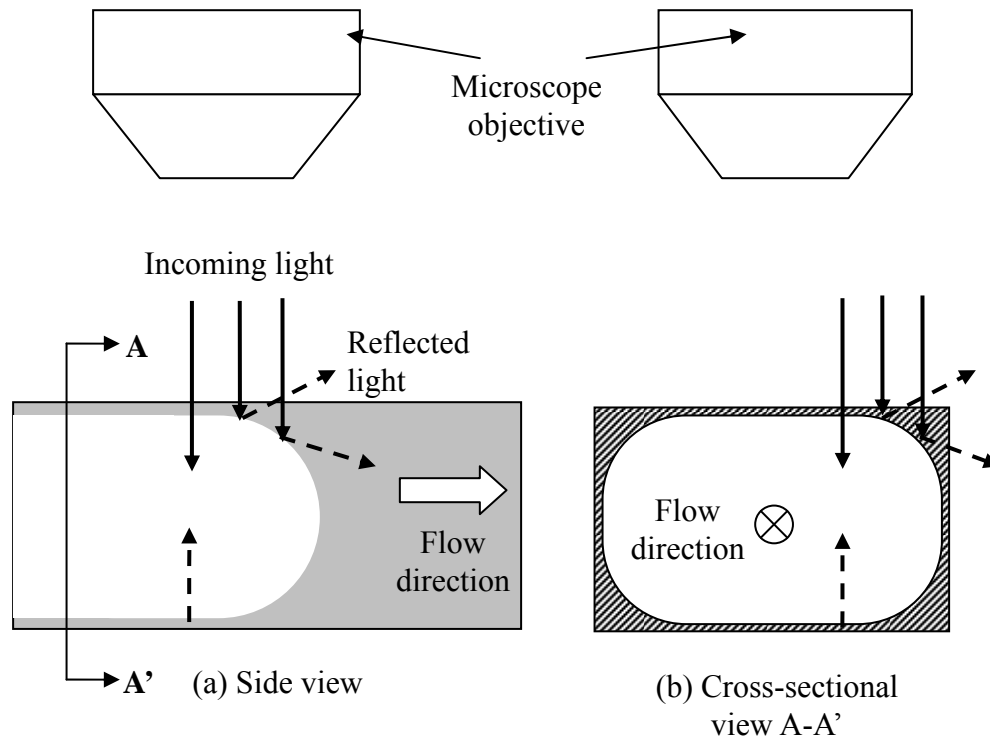


Figure 5.5. Schematic diagram to understand liquid film observation near corner of channel wall and bubble front. Shaded area can be observed as dark thick liquid film and solid and dash lines represent incoming light and reflected light. (a) side view (flow direction: from left to right), (b) cross-sectional view A-A' (flow direction: into images)

Incoming light passes directly pass through the flat liquid film and gas and then reflects back in the opposite direction of the incoming light. However, light reflects from a surface at the same angle relative to the surface normal. This reduces the light detected by the microscope lens, explaining the dark region surrounding the bubble. The bubble curvature, which is not detected in Fig. 5.4c, will result in an overestimation of the void fraction. To correct this overestimation, one-half of the

bubble curvature area, such as that shown Fig. 5.4d, is subtracted from the total bubble area, as is shown in Fig. 5.4c.

Therefore, to assess the two-dimensional, area-averaged void fraction, the bubble area in each region of interest of each frame in a movie is defined. From this value, half of the area defining the liquid film surrounding the curved part of the bubble is subtracted. This difference is summed over each image in a movie and then divided by the total number of images in the movie. This results in an average value of the corrected bubble area. An area-averaged void fraction is computed by dividing the average value of the bubble area by the area of interest that was determined from the base image. In equation form and in terms of pixels,

$$\alpha_{imag} = \frac{\sum_{i=1}^r \sum_{j=1}^q (p_b - 0.5 p_c)}{r \sum_{i=1}^q p_t} \quad (5.10)$$

where p represents a white pixel in a binarized image, r is the number of frames in a movie, and q represents the number of pixels defining the area of interest in which the image based void fraction, α_{imag} , is being assessed. Subscripts b, c, and t represent the full bubble image, the bubble curvature image, and the total region of interest in which the analysis is being conducted.

5.2.3 Data reduction from PIV images

Recall from Eq. 5.9, the second means to assess void fraction, that α_{slip}

requires knowledge of the slip ratio. The slip ratio is defined in Eq. 5.8. To measure interfacial velocities, the average of which will represent the gas velocity, and to measure average liquid velocities for use in the slip ratio requires micro-PIV analysis techniques.

In those image pairs with no gas present, the two sequential PIV images in the pair were analyzed by Dantec Flow Manager[®] software using an adaptive cross correlation function to create a velocity vector field of the liquid. For vector analyses, the interrogation window size was set to 32x32 pixels with a 50% overlap. This is the smallest interrogation window size used for 10x micro-objective lens. For the image pairs acquired with the 20x micro-objective lens, at the k=3 and k=4 branch levels, an interrogation window size of 128x32 pixels with a 50% overlap was used. The rationale for this larger interrogation window is due to the need for sufficient fluorescent particle density in the interrogation window to generate velocity vectors. Masks of the bubble area and channel area required definition by the user. This step was done to prevent the software from attempting to calculate velocity vectors inside the masked regions. This masking function is provided as an option in the Dantec Flow Manager[®] software.

Approximately, 27 velocity vectors were generated across the channel at the k=0 branch and 8 velocity vectors across the channel at the k=4 were generated from images acquired with the 10x objective lens. For the 20x objective lens images, the numbers of velocity vectors at the k=3 and k=4 branch levels were 19 and 14, respectively. How these velocity fields were used to assess an average liquid velocity

is discussed in the next section.

5.2.4 Average liquid velocities

For each of the imaging fields shown as solid line-type boxes in Fig. 5.2, experimental liquid velocity profiles were generated from micro-PIV flow fields. The downstream locations at which these profiles were generated are in the fully developed region, as was confirmed by

$$\frac{x_{fd}}{D_h} \approx \frac{0.6}{1 + 0.035 \text{Re}_D} + 0.056 \text{Re}_D \quad (5.11)$$

from White (1991) where x_{fd} is the streamwise distance at which the flow becomes fully developed, D_h is the hydraulic diameter and Re_D is the Reynolds number based on the hydraulic diameter. These liquid velocity profiles were normalized by the maximum or centerline velocity and then compared with an analytical solution of the fully developed velocity profile at the centerline of a rectangular duct. The analytical solution used for this analysis is that proposed for macro-size ducts by Shah and London (1978). If the experimental velocity profile was found to well match the analytical solution, a three-dimensional velocity profile can be analytically generated. In Fig. 5.6, the coordinate system and channel aspect ratio, α^* , are shown. The x-y-z coordinate system is located at the mid-depth in the channel. The x and y axes are in the streamwise and spanwise directions, respectively. The z axis is in the direction of channel depth. The equation representing the analytical solution of a non-dimensional,

fully developed velocity profile in the rectangular channel with no-slip boundary condition is

$$u' = \frac{u}{u_{\max}} = \left[1 - \left(\frac{z}{b} \right)^n \right] \left[1 - \left(\frac{y}{a} \right)^m \right] \quad (5.12)$$

where u' is the non-dimensional form of the streamwise component of velocity, u , and u_{\max} is the maximum (centerline) velocity. Variables a and b represent half of the channel width and channel depth, respectively, as shown in Fig. 5.6.

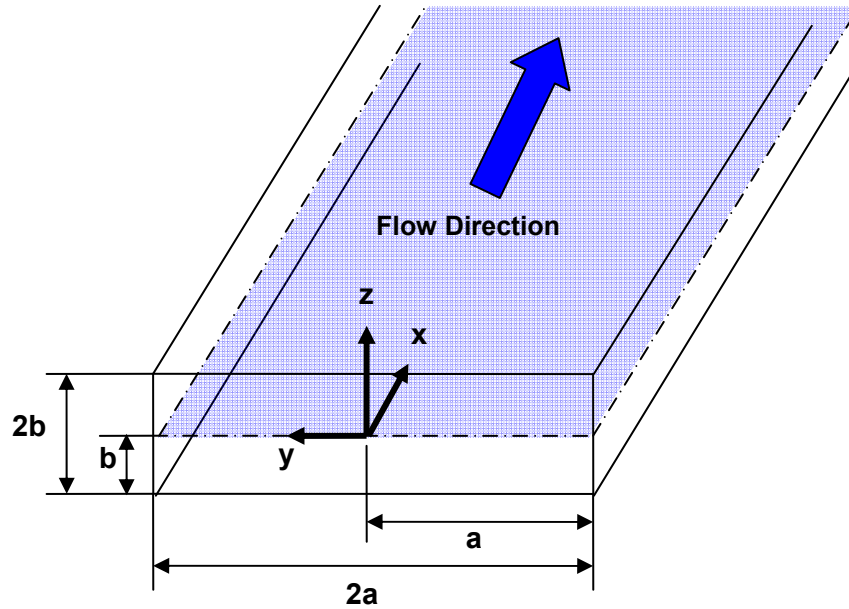


Figure 5.6. Rectangular geometry with coordinate system and parameter identification

The

exponents of m and n are evaluated by

$$m = 1.7 + 0.5 (\alpha^*)^{-1.4} \quad (5.13)$$

$$n = \begin{cases} 2 & \text{for } \alpha^* \leq 1/3 \\ 2 + 0.3 (\alpha^* - 1/3) & \text{for } \alpha^* \geq 1/3 \end{cases}$$

where α^* is the aspect ratio of the rectangular channel

$$\alpha^* = \frac{2b}{2a} = \frac{b}{a} \quad (5.14)$$

For the $k=0$ branch level, the half-width of the channel, a , is $215 \mu\text{m}$ and the aspect ratio of a channel in this branch level is approximately 0.58. From Eq. 5.13, m and n values are founded to be 2.8 and 2.1, respectively.

Figure 5.7 shows several experimental mid-depth velocity profiles at various positions, x , along the axial direction in the $k=0$ branch level. For completeness, the mass flow rates of gas and liquid are 20 g/min and 0.03 g/min , respectively. Note that x is measured from the edge of the field of view, corresponding with the first velocity vector column in each velocity vector field. Developing flow velocity profiles are shown for several local axial locations between $16 \mu\text{m}$ and $978 \mu\text{m}$. Fully developed conditions are observed to occur between x -locations of $1141 \mu\text{m}$ and $1304 \mu\text{m}$. This corresponds with the estimate of $1160 \mu\text{m}$ determined from Eq. 5.11.

Figure 5.8 shows a theoretical fully developed velocity profile at the channel midplane compared to the experimental spanwise velocity data at an x location of $1250 \mu\text{m}$ in the $k=0$ level. Both profiles are normalized by the maximum value. As is observed in Fig. 5.8, the fully developed analytical and experimental velocity profiles show good agreement. This is the case for all branching levels, with average standard deviation between the analytical and experimental profiles of $\pm 6.0 \text{ mm/s}$ (or $\pm 3\%$). To yield an average liquid velocity, u_f , the three-dimensional analytical solution is used

$$u_f = \frac{u_{\max}}{\left(\frac{m+1}{m}\right)\left(\frac{n+1}{n}\right)} \quad (5.15)$$

where the constants of m and n are found from Eq. 5.13, and the maximum experimental velocity value is used for u_{\max} . Finally, Figure 5.9 shows a three-dimensional fully developed velocity profile using the analytical solution with the maximum velocity value obtained from experimental data.

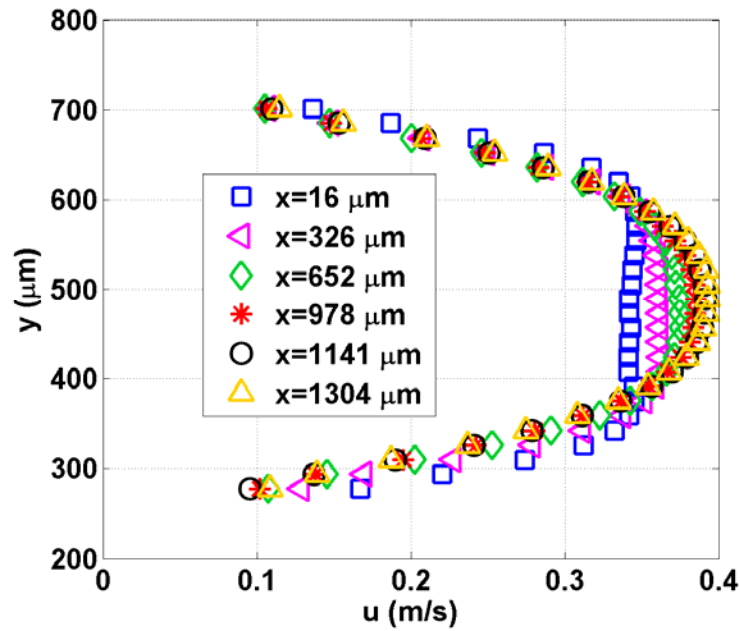


Figure 5.7. Experimental velocity profiles along the axial direction at the $k=0$ branch (mass flow rates of gas and liquid are 20 g/min and 0.03 g/min, respectively)

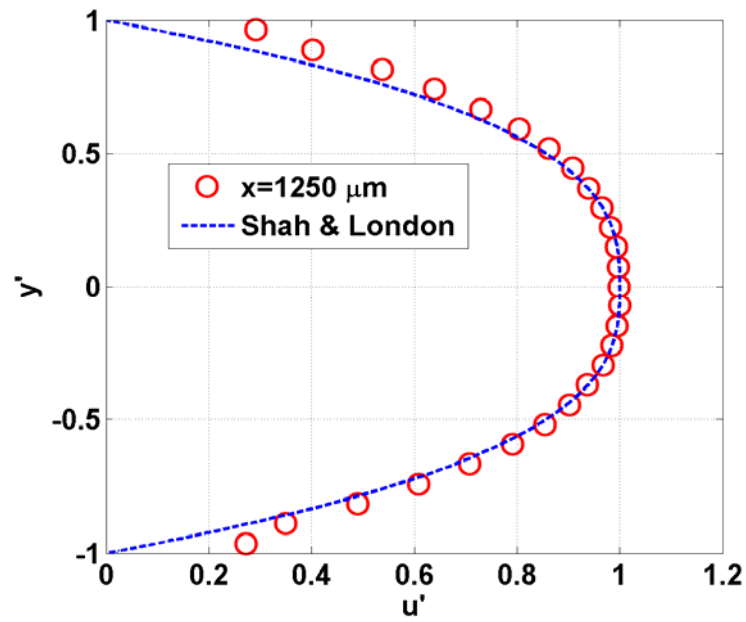


Figure 5.8. Experimental and analytical fully developed velocity profiles at the $k=0$ branch

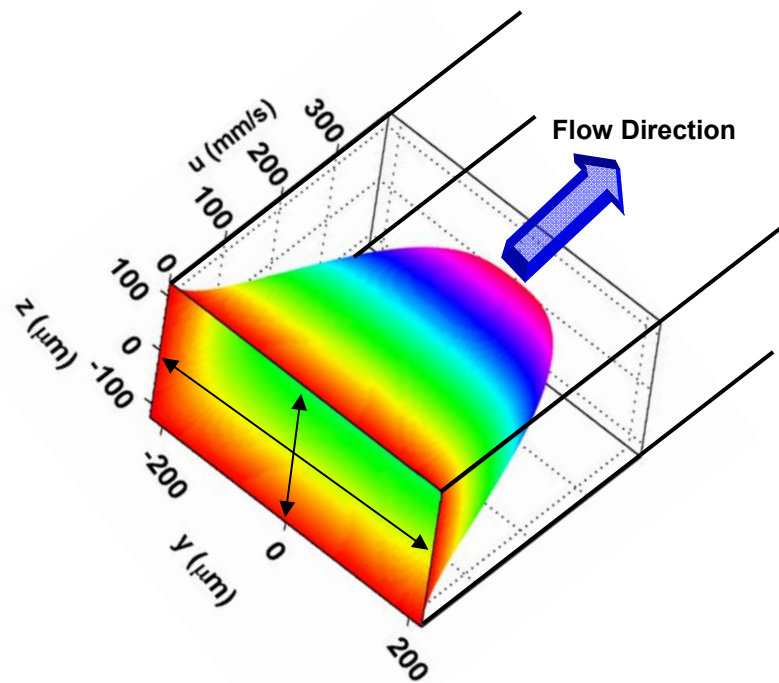


Figure 5.9. Three-dimensional fully developed velocity profile

5.2.5 Average gas velocities

To provide an assessment of the average bubble velocities, it was determined that measurement of the interface velocity at the centerline of the channel was sufficient. Tracking of the leading and trailing interfaces to account for variations in interface shape yielded results within the uncertainty of the technique employed.

Using a bubble sorting program devised for this project and written in Matlab[®], image pairs with single bubbles in both images were successfully isolated from liquid only and multiple bubble images. Single bubble images fit into one of the three different bubbles categories shown in Fig. 5.10. All images in this figure were acquired at the $k=0$ branch level. The first type of bubble image is one in which the entire single bubble is captured in the field of view for both images in an image pair. A representative bubble in its entirety is shown in Fig. 5.10a. The second type of bubble image, shown in Fig. 5.10b, is that when a single bubble is entering the field of view. As in all cases presented flow is from left to right, the interface represents the leading edge of bubble as it appears in the left side of each field of view. The last bubble image type is characterized when only the trailing edge of bubble is recorded in both of the image pairs. This type of bubble is observed at the right side of the field of view for each image in the image pair. A representative trailing edge of a bubble is shown in Fig. 5.10c.

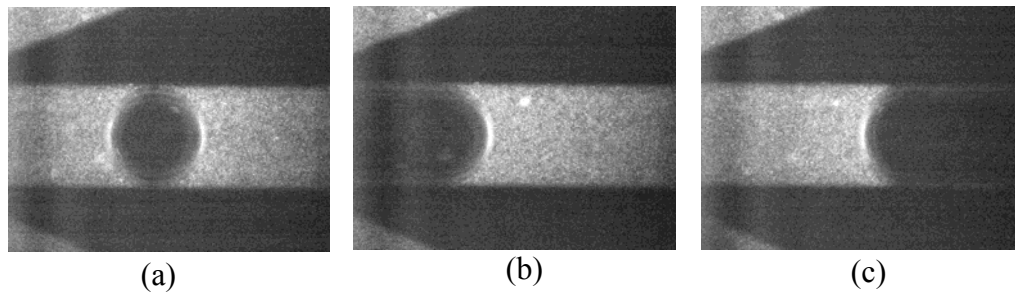


Figure 5.10. Three different types of bubble images at $k=0$ branching level

Separately, each type of bubble was analyzed using image processing techniques. In the image processing algorithm, histogram equalization was employed on both of the sequential images in the image pair in order to enhance the contrast between the gas and liquid and to minimize noise. The image pairs were subsequently filtered with 10x10 pixels median filter. Figures 5.11a and 5.11b show sequential image pairs at the $k=0$ level and that have undergone these image processing steps. Recall that the time interval between these two sequential images is $480 \mu\text{s}$. Figure 5.11c shows intensity variations along the channel centerlines for both the original and second images in Figs. 5.11a and 5.11b, respectively. The intensity profiles are provided as a function of the downstream location in the channel defined by the field of view. The highest intensities indicate the bubble interfaces. The streamwise location of the leading interface in Fig. 5.11a is identified with a solid red line in Fig. 5.11c. Likewise, the location of the leading interface, $480 \mu\text{s}$ later, is identified with a blue dashed line. The spatial displacement of the interface divided by the time interval between the image pairs yields the centerline velocity of the interface. Velocity

assessments of leading only, trailing only, and both leading and trailing velocities of “entire” bubbles are provided in Chapter 6. Averaged together, these provide the gas velocity used in the slip ratio.

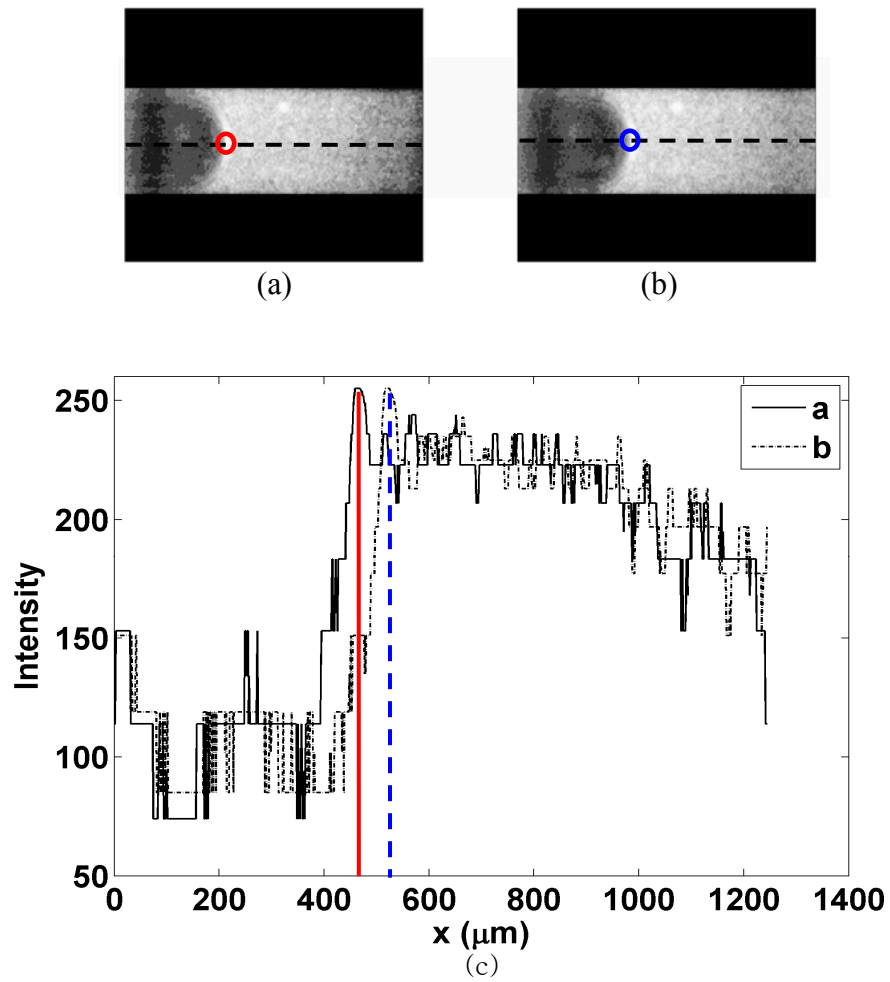


Figure 5.11. Interface velocity assessment (a) first image in image pair (b) second image in image pair, and (c) intensity variations in (a) and (b)

CHAPTER 6

RESULTS AND DISCUSSION

In this chapter two-phase flow patterns, void fraction, and flow fields near bifurcations in a fractal-like branching channel network are discussed. The results are present in three sections: (1) flow regimes, (2) void fraction comparisons with correlations, and (3) liquid velocity fields at bifurcations. In the first section, two-phase flow patterns are discussed and located on flow regime maps, as was proposed in Chapter 4. Pattern observations at each branch level are compared with flow regime maps from other studies. The second section of this chapter includes results of void fraction for each channel using two different measurement techniques: HSHR and micro-PIV. Experimental void fraction results, based on slip ratios and area-averaged two-phase images, are compared with existing void fraction correlations. In the last section of this chapter are presented general observations of two-phase liquid flow fields at the bifurcation sections.

6.1 Flow Regimes

From the two-phase flow images acquired at the $k=0$ branch level, four different flow patterns were observed. Figure 6.1 shows flow pattern observations at the $k=0$ branch level along side a schematic of flow regimes identified in Kawaji and

Chung (2004). As is evident from this figure, the flow patterns observed in Kawaji and Chung (2004) are very similar to the two-phase flow patterns observed in the $k=0$ branch level in present study. To be consistent with other studies, the pattern nomenclature in Kawaji and Chung (2004) is being modified slightly in this study.

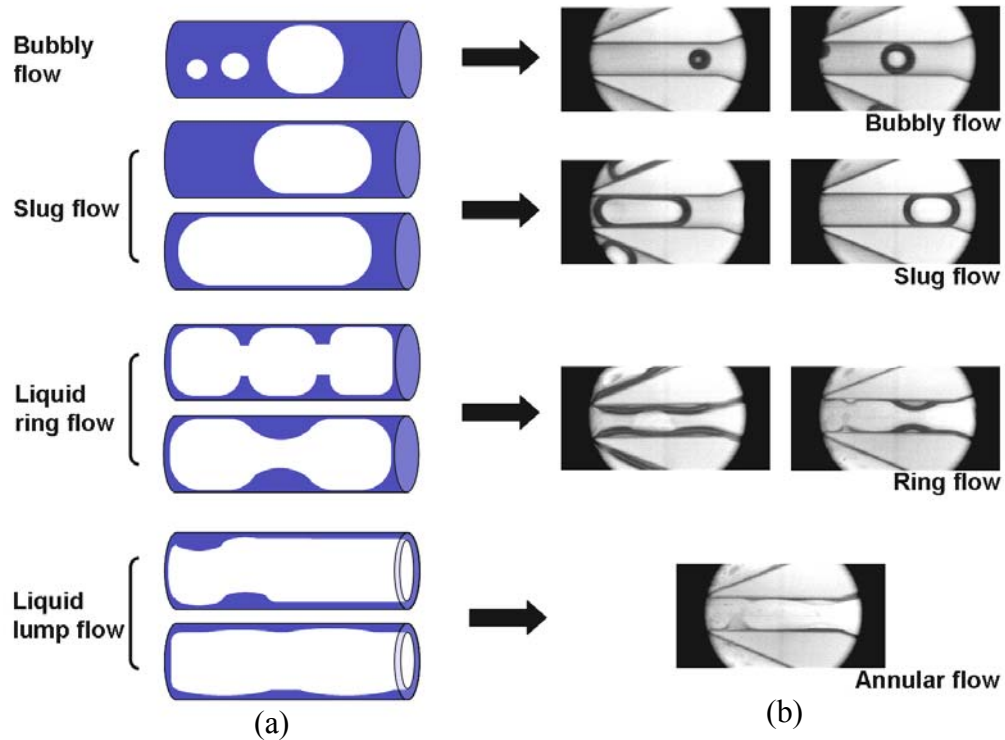


Figure 6.1. Two-phase flow patterns comparisons between (a) Kawaji and Chung (2004) and (b) present study at $k=0$ branch level

Four different two-phase flow patterns, (bubbly, slug, liquid ring and liquid lump flows) were used in Kawaji and Chung (2004). However, in the present study, ring and annular flows are used instead of liquid ring and liquid lump flows, respectively. Bubbly flow is defined as the presence of one or more bubbles, each having a diameter equal to or smaller than the channel width. Slug flow is defined when the bubble

length is larger than the width of channel, but short enough not to occupy the entire channel. The ring flow pattern represents a bubble filling an entire channel length (i.e., the flow field) with a very thick liquid film. This thick liquid film has a symmetrical wave pattern about the centerline of the channel. Finally, annular flow patterns are defined when an irregular, very thin liquid film occurs around a gas core and the bubble extends the entire length of the field of view.

Figure 6.2 shows two-phase flow patterns in the $k=0$ level and over the range of gas and liquid superficial velocities corresponding to the test plan reported in Table 4.1. Figures 6.3 through 6.5 show similar results for the remaining branch levels, $k=1$ through $k=4$, respectively. Recall that a superficial velocity is defined as the total volumetric flow rate of a phase, assuming it independently, i.e., in absence of the other phase, flows through the actual cross-sectional area of the channels. Mathematically, these velocities are defined in Eq. 5.5, and change at each branch level as a result of a change in flow area following each bifurcation.

Figure 6.2 shows flow patterns for 12 different gas-liquid two-phase flow conditions in the branch level $k=0$. Reported along the top row are superficial gas velocities, with superficial liquid velocities reported in the first column. For the higher superficial liquid velocities, between 0.208 m/s and 0.417 m/s, with superficial air velocities ranging from 0.007 m/s to 0.104 m/s, bubbly and slug flow patterns are mainly observed. These velocity combinations correspond with test cases 1, 2, 5, 6, 7 and 8. When the superficial liquid velocities are reduced for these same superficial gas velocities, slug flow patterns are observed, as in the experimental test cases of 3, 4 and

9. Case 11 and case 12 show mixed gas-liquid patterns of slug and ring flows, which occur with an increase in superficial gas velocity while holding the superficial liquid velocities constant. Cases exhibiting multiple flow regime patterns are considered to be in the transitional region between these regimes. The experimental test case 10, in Fig. 6.2, shows both ring (top) and annular flow (bottom) patterns.

Flow patterns for the same mass flow rates, but in the first branch level of $k=1$, are provided in Fig. 6.3. Two channels of the $k=1$ level, which share the same upstream ($k=0$) channel, are shown in each field of view. Flow pattern observations for all 12 different cases at the $k=1$ branch level are very similar to the flow patterns observed in Fig. 6.2.

Figure 6.4 shows two-phase flow patterns for the branch level of $k=2$. Two channels narrower and longer than those in the $k=1$ branch level are shown in each field of view. Again these channels share an upstream bifurcation, hence they share the same upstream channel. Each channel width is approximately $200\text{ }\mu\text{m}$ and it is about half the width of the $k=0$ channels. The most prevalent flow pattern is slug flow, observed for liquid and gas superficial velocity ranges between 0.03 m/s and 0.11 m/s and between 0.004 m/s and 0.052 m/s , respectively. These flow conditions are identified as the following test cases: 2, 3, 4, 5, 8, 9, and 12. Bubbly and slug flow patterns are observed in the experimental test cases 1, 6 and 7, corresponding with the higher superficial liquid velocity of 0.21 m/s . Cases 12, 11 and 10 show slug, slug and ring, and ring and annular flow patterns, respectively. There is a clear transition in flow patterns with a decrease in superficial liquid velocities, from 0.21 m/s and 0.03

m/s for a fixed superficial gas velocity of 1 m/s. The mixed flow patterns, such as slug-ring and ring-annular, can be explained as undergoing a transition between two-phase flow regimes.

Two-phase flow observations at the branch levels of $k=3$ and $k=4$ are shown in Figs. 6.5 and 6.6, respectively. For these very small channels, having hydraulic diameters of 180 μm and 143 μm , respectively, mostly slug flows are observed. The two exceptions occur for the same cases, case 10 and case 11, in both the $k=3$ and $k=4$ branch levels. The channel widths of the $k=3$ and $k=4$ levels are 141 μm and 100 μm , respectively. It is believed that slug flow is caused by surface tension dominating the forces in the second smallest and smallest channel widths. As the superficial liquid velocity is decreased while holding the highest superficial air velocity constant, transitions between slug and ring flows in case 11 and between slug, ring and annular flows in case 10 appear to be occurring. For example, both slug and ring flow patterns are observed in case 11. Three different two-phase flow patterns of slug, ring and annular are observed in case 10.

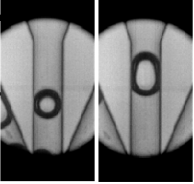
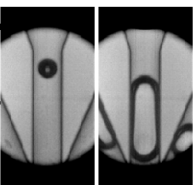
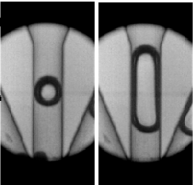
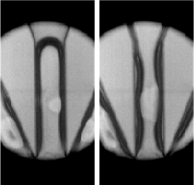
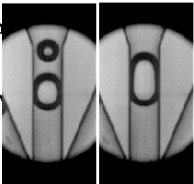
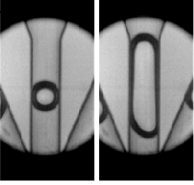
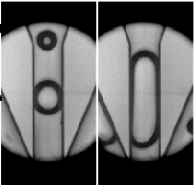
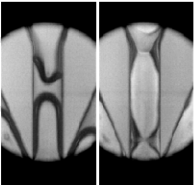
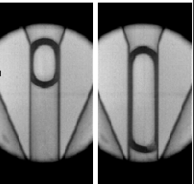
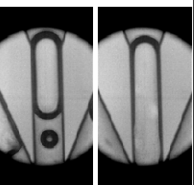
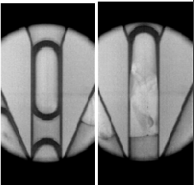
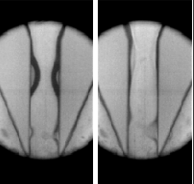
Branching Level k=0	Superficial air velocities			
Liquid flow rate (superficial vel.)	~0.007 m/s	~0.014 m/s	~0.104 m/s	~1.844 m/s
~40 g/min (~0.42 m/s)	Case 1 Bubbly & Slug 	Case 6 Bubbly & Slug 	Case 7 Bubbly & Slug 	Case 12 Slug & ring 
	Case 2 Bubbly & Slug 	Case 5 Bubbly & Slug 	Case 8 Bubbly & Slug 	Case 11 Slug & ring 
~20 g/min (~0.21 m/s)	Case 3 Slug 	Case 4 Slug 	Case 9 Slug 	Case 10 Ring & annular 
~5 g/min (~0.05 m/s)				

Figure 6.2. Flow patterns for 12 different gas-liquid flow conditions in branching level of k=0

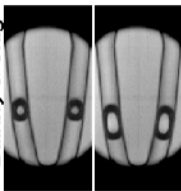
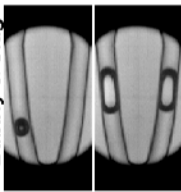
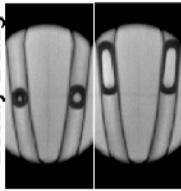
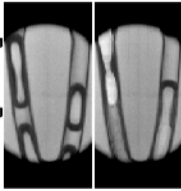
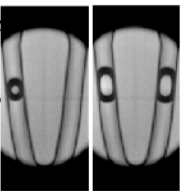
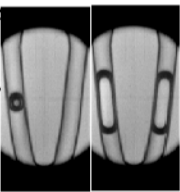
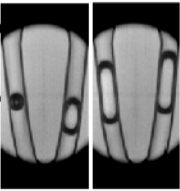
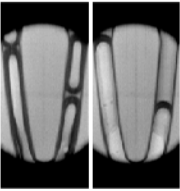
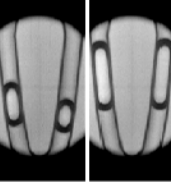
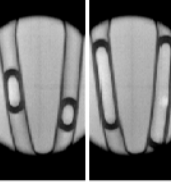
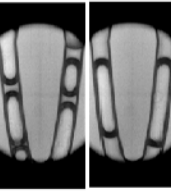
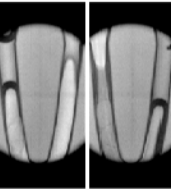
Branching Level k=1	Superficial air velocities				
	Liquid flow rate (superficial vel.)	~0.005 m/s	~0.010 m/s	~0.074 m/s	~1.303 m/s
~40 g/min (~0.30 m/s)		Case 1 Bubbly & Slug 	Case 6 Bubbly & Slug 	Case 7 Bubbly & Slug 	Case 12 Slug & ring 
	~20 g/min (~0.15m/s)	Case 2 Bubbly & Slug 	Case 5 Bubbly & Slug 	Case 8 Bubbly & Slug 	Case 11 Slug & ring 
~5 g/min (~0.04 m/s)		Case 3 Slug 	Case 4 Slug 	Case 9 Slug 	Case 10 Ring & annular 

Figure 6.3. Flow patterns for 12 different gas-liquid flow conditions in branching level of k=1

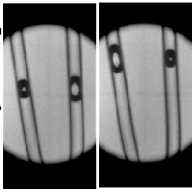
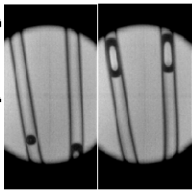
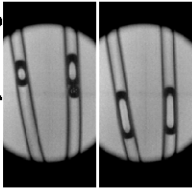
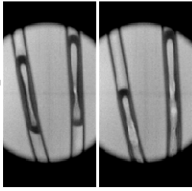
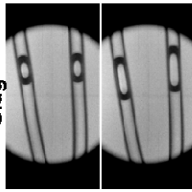
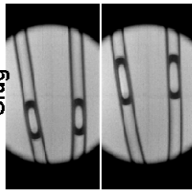
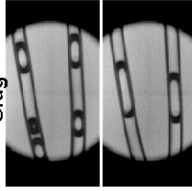
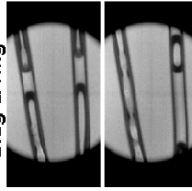
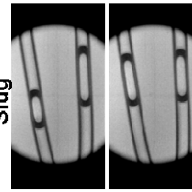
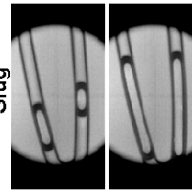
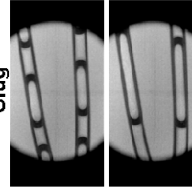
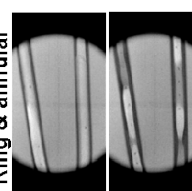
Branching Level k=2	Superficial air velocities			
Liquid flow rate (superficial vel.)	~0.004 m/s	~0.007 m/s	~0.052 m/s	~0.922 m/s
~40 g/min (~0.21 m/s)	Case 1 Bubbly & Slug 	Case 6 Bubbly & Slug 	Case 7 Bubbly & Slug 	Case 12 Slug 
	Case 2 Slug 	Case 5 Slug 	Case 8 Slug 	Case 11 Slug & ring 
~20 g/min (~0.11 m/s)				
	Case 3 Slug 	Case 4 Slug 	Case 9 Slug 	Case 10 Ring & annular 
~5 g/min (~0.03 m/s)				

Figure 6.4. Flow patterns for 12 different gas-liquid flow conditions in branching level of k=2

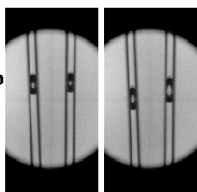
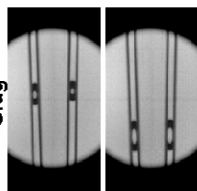
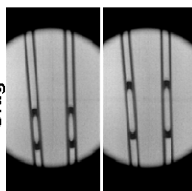
Branching Level k=3		Superficial air velocities			
Liquid flow rate (superficial vel.)		~0.003 m/s	~0.005 m/s	~0.037 m/s	~0.654 m/s
~40 g/min (~0.15 m/s)	Case 1 Slug		Case 6 Slug	Case 7 Slug	Case 12 Slug
	Case 2 Slug		Case 5 Slug	Case 8 Slug	Case 11 Slug & ring
~20 g/min (~0.07 m/s)					
~5 g/min (~0.02 m/s)	Case 3 Slug		Case 4 Slug	Case 9 Slug	Case 10 Slug, ring & annular

Figure 6.5. Flow patterns for 12 different gas-liquid flow conditions in branching level of k=3

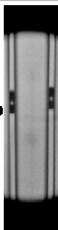
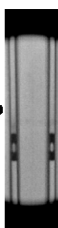


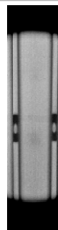
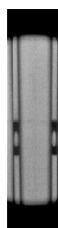

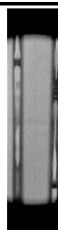

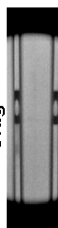
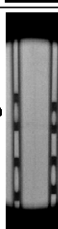



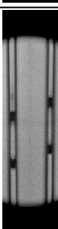
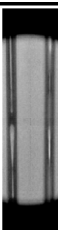
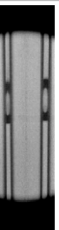
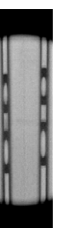

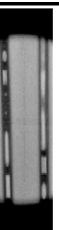




Branching Level k=4		Superficial air velocities			
Liquid flow rate (superficial vel.)		~0.002 m/s	~0.004 m/s	~0.026 m/s	~0.461 m/s
~40 g/min (~0.10 m/s)		Case 1 Slug 	Case 6 Slug 	Case 7 Slug 	Case 12 Slug 
					
~20 g/min (~0.05m/s)		Case 2 Slug 	Case 5 Slug 	Case 8 Slug 	Case 11 Slug & ring 
					
~5 g/min (~0.01 m/s)		Case 3 Slug 	Case 4 Slug 	Case 9 Slug 	Case 10 Slug, ring & annular 
					

Figure 6.6. Flow patterns for 12 different gas-liquid flow conditions in branching level of k=4

Two-phase, gas-liquid, flow pattern observations made in a fractal-like branching channel network are compared to existing two-phase flow regime maps. Flow regime maps are plotted as a function of superficial gas and superficial liquid velocities on logarithmic axes. Figure 6.7 shows two-phase flow patterns for all 12 test cases at the (a) $k=0$ and (b) $k=1$ branch levels. Regimes for the present study are identified by symbols on the maps.

Using the hydraulic diameters of the $k=0$ and $k=1$ level channels, which are $308\text{ }\mu\text{m}$ and $265\text{ }\mu\text{m}$, respectively, flow regime maps were created using the Taitel and Dukler (1976) model and are overlain on Fig 6.7a and 6.7b, respectively. Experimental results from Chung and Kawaji (2004), acquired using a $250\text{ }\mu\text{m}$ diameter tube, are also included on both figures for comparison purposes. The transition lines on the Chung and Kawaji (2004) experimental flow regime map are displayed as dashed gray lines, with flow regimes identified in gray font enclosed in parentheses. Taitel and Dukler (1976) flow regime maps are presented as solid blue lines with blue font. In Fig. 6.7, Taitel and Dukler (1976) flow regimes are identified as dispersed bubble, intermittent and annular-dispersed flows, which can also be expressed as bubbly, slug and annular flows. The latter terminology is that used in the present study.

Evident from Fig. 6.7 is that the Taitel and Dukler (1976) flow regime maps show good agreement with the flow pattern observations in the $k=0$ and $k=1$ branch levels of the fractal-like branching channel network. Most of the observed slug flow patterns are inside of intermittent regime defined by the Taitel and Duklar (1976) model and inside the slug flow regime of the Chung and Kawaji (2004) map. The

mixed flow patterns consisting of bubbly and slug flows, earlier characterized as a transitional flow regime, are within the Taitel and Duklar (1976) regime of dispersed bubble flow. However, these data are very close to the transition line between the two flow regimes. The transition line between bubbly and slug flow regimes identified in the map of Chung and Kawaji (2004) is located at higher superficial liquid velocities than the region predicted by Taitel and Dukler (1976). ; The experimental test conditions in the present study extend to much lower superficial gas velocities than those studied by Chung and Kawaji (2004). Slug and annular flow regimes in both the $k=0$ and $k=1$ branch levels match well with the predicted regimes of Taitel and Dukler (1976).

In Fig. 6.8, flow pattern observations at the (a) $k=2$ and (b) $k=3$ branch levels are provided, as are maps predicted using the theoretical model of Taitel and Dukler (1976). Hydraulic diameters for the $k=2$ and $k=3$ level channels that were used in the model are $222\text{ }\mu\text{m}$ and $180\text{ }\mu\text{m}$, respectively. Also included in Fig. 6.8 is the experimental map of Chung and Kawaji (2004), created using a $250\text{ }\mu\text{m}$ diameter tube. As before, solid blue lines identify regime transitions for the Taitel and Dukler (1976) map, and dashed lines and regime labels enclosed in parentheses belong to the Chung and Kawaji (2004) map. Although the transition between intermittent and annular-dispersed flows on the Taitel and Dukler (1976) map is fairly insensitive to decreases in hydraulic diameter, there is a clear downward shift (i.e., decrease in superficial liquid velocity) in the transition between the dispersed bubble and intermittent flow regimes.

As is evident from Fig. 6.8b and consistent with pattern observations presented in Fig. 6.5, bubbly flow is absent from the flow regime map. Also, introduced in Fig. 6.8b is a replacement of ring-annular flow with slug-ring-annular flow. Both the Taitel and Dukler (1976) and Chung and Kawaji (2004) maps agree well with experimental observations.

Finally, two-phase flow observations in the $k=4$ branch level are compared with a map generated using the Taitel and Dukler (1976) model with a hydraulic diameter of $143\text{ }\mu\text{m}$. This map is replicated in both Figs. 6.9(a) and 6.9(b). For the $k=4$ level channels, slug flow was the predominant flow regime observed for the range of superficial velocities comprising the experimental test cases. Likewise, it was the flow regime most predicted by the Taitel and Dukler (1976) model for the same flow conditions. The transitional flow regimes of slug-ring and slug-ring-annular are observed near the transition lines separating slug (intermittent) and annular (annular-dispersed) flow regimes.

The experimental observations from the $k=4$ branch level are also compared with the flow regime maps from (a) Kawahara et al. (2002) based on a $100\text{ }\mu\text{m}$ circular tube and (b) Chung and Kawaji (2004) based a $96\text{ }\mu\text{m}$ square channel. According to both Kawahara et al. (2002) and Chung and Kawaji (2004), slug-ring flow regimes are predicted for the flow conditions in the present investigation. Most of data in the present investigation were acquired at much lower superficial gas velocities than those studied by either Kawahara et al. (2002) or Chung and Kawaji (2004).

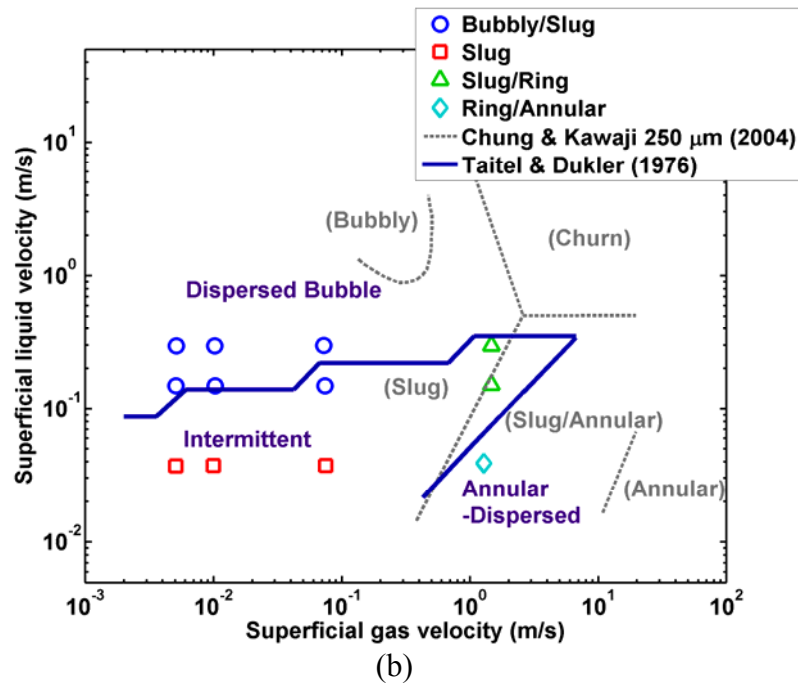
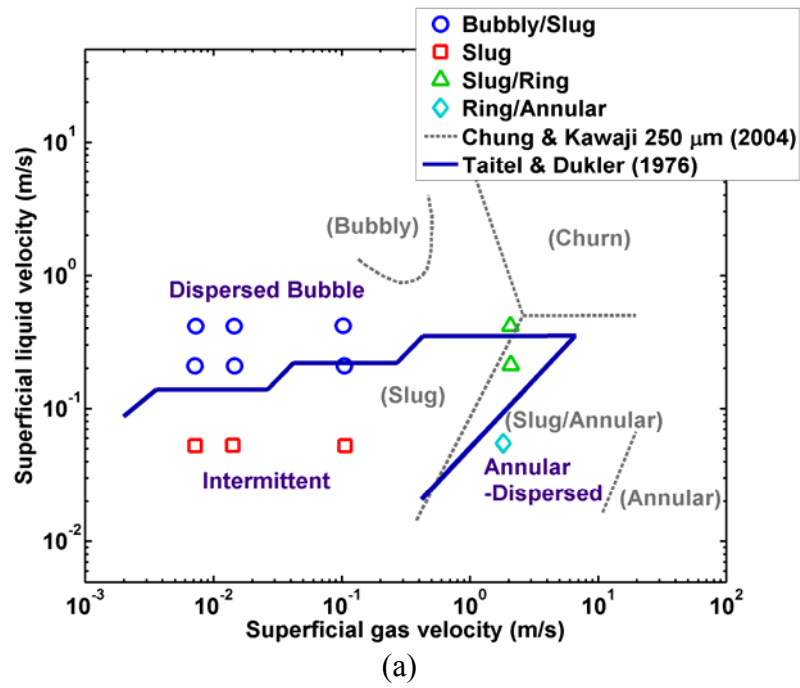


Figure 6.7. Flow regime map comparisons between Taitel and Dukler (1976) and Chung and Kwaji (2004) with flow pattern observations. (a) flow regime maps for $k=0$ branch, (b) flow regime map for $k=1$.

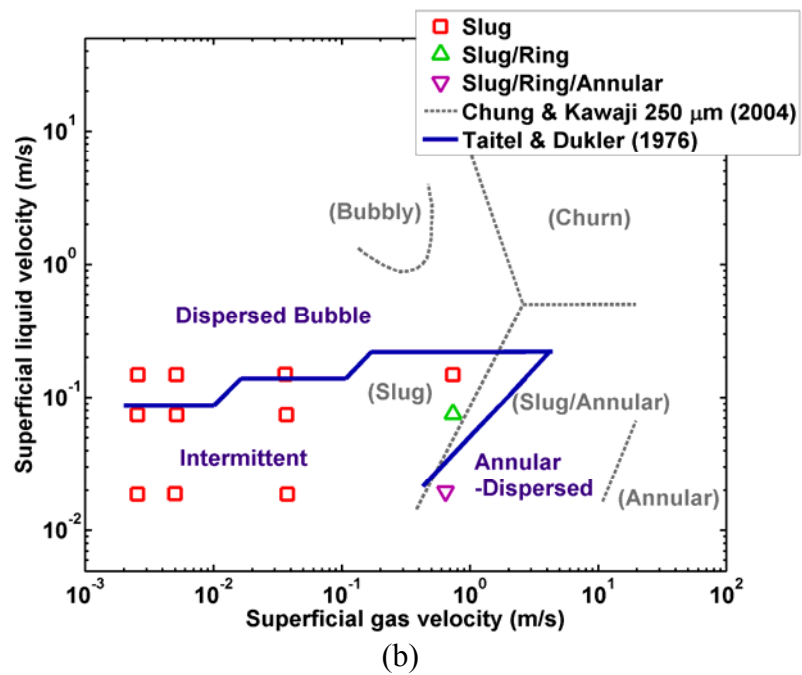
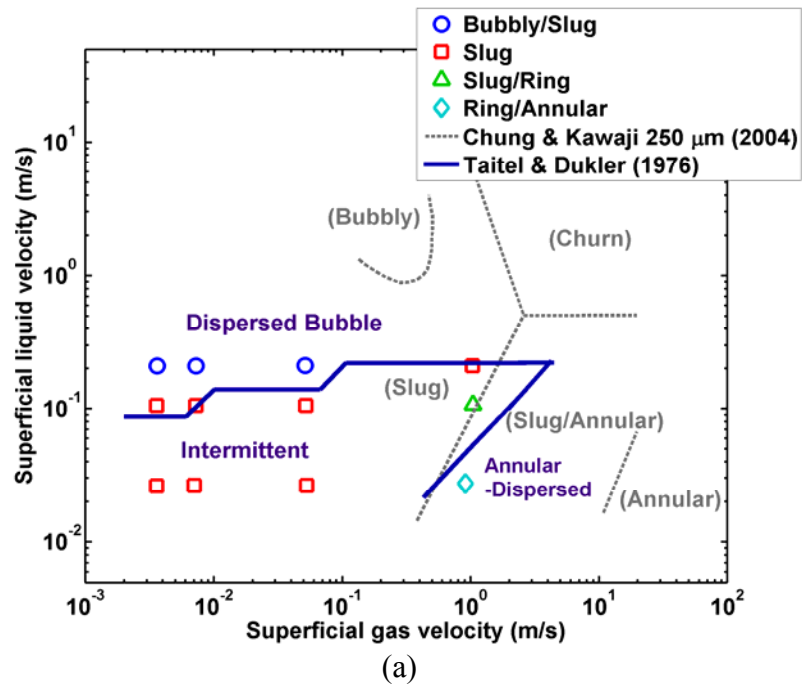


Figure 6.8. Flow regime map comparisons between Taitel and Dukler (1976) and Chung and Kwaji (2004) with flow pattern observations. (a) flow regime map for $k=2$ branch, (b) flow regime map for $k=3$.

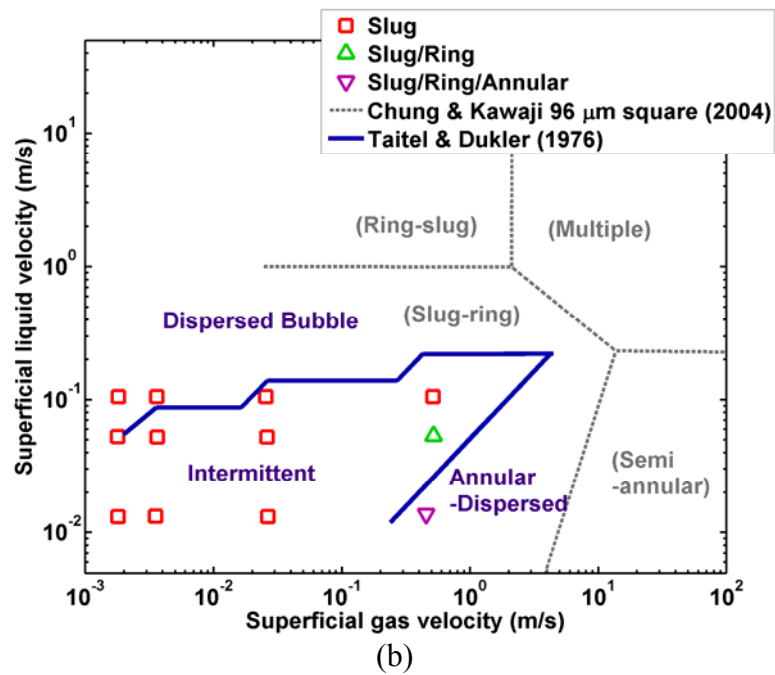
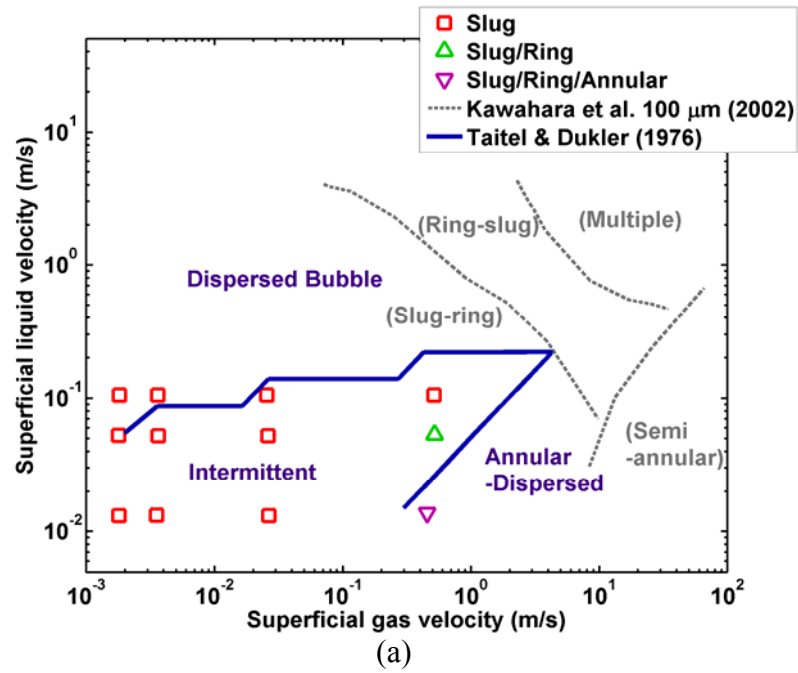


Figure 6.9. Flow regime map comparisons between Taitel and Dukler (1976) for $k=4$ branch and other studies of (a) Kawahara et al. 100 μm tube and (b) Chung and Kwaji (2004) 96 μm square channel with flow pattern observations.

6.2 Void Fraction Correlations and Comparison

In this section, results from two void fraction techniques, discussed previously in Chapter 4, are presented and compared with existing void fraction correlations. Void fraction is assessed using the slip ratio, as determined by local liquid and gas velocities. Void fraction is also assessed using two-dimensional images.

6.2.1 Slip ratio

To compute the slip ratio, local average liquid velocities and bubble velocities are used. Local liquid velocities are determined using Eq. 6.1 and the experimentally measured maximum velocity obtained from micro-PIV.

$$u_f = \frac{u_{\max}}{\left(\frac{m+1}{m}\right)\left(\frac{n+1}{n}\right)} \quad (6.1)$$

Average centerline interface velocities, as determined from image processing, are used for the gas velocity. The void fraction based on slip ratio, α_{slip} , is computing from Eq. 6.2 using the experimentally assessed slip ratio.

$$\alpha_{\text{slip}} = \frac{1}{1 + \left(\frac{u_g}{u_f}\right)\left(\frac{1-x}{x} \frac{\rho_g}{\rho_f}\right)} \quad (6.2)$$

Figures 6.10a and 6.10b show leading edge and trailing edge interface (hereafter referred to as bubble) velocities, respectively, at the k=0 branch level for case 8. A reminder is provided here that these values are based on interface

displacements measured at the centerline of the channel. Recall that three cases were considered: leading edge only, trailing edge only, and both leading and trailing edges. These cases are consistent with a bubble entering the region of interest, leaving the region of interest, and completely within the region of interest, respectively. Leading edge bubbles were observed for 40 image pairs in the $k=0$ level. Leading edge bubble velocities determined for each of these cases are shown in Fig. 6.10a. The average and standard deviation are 0.23 m/s and ± 0.05 m/s, respectively.

Figure 6.10b shows trailing edge velocities. The average trailing edge velocity is 0.23 m/s with a standard deviation of ± 0.03 m/s. Figure 6.11 shows (a) leading and trailing velocities and (b) the differences between leading and trailing velocities. Recall that for this case, both leading and trailing edges of the bubble appeared in each image of the image pair. Both leading and trailing edge bubble velocities have the same average velocity of 0.24 m/s and the same standard deviation of ± 0.04 m/s. The average of all the interface velocities are used as the gas velocity in computing the slip ratio and in Eq. 5.3 for assessing the void fraction using the slip ratio. The slip ratios for five different flow conditions and for each branch level are listed in Table 6.1.

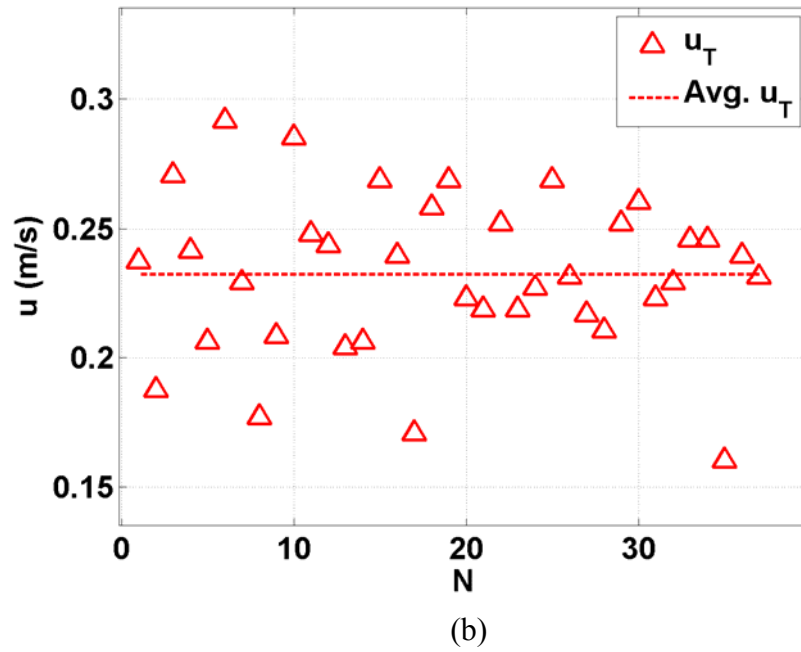
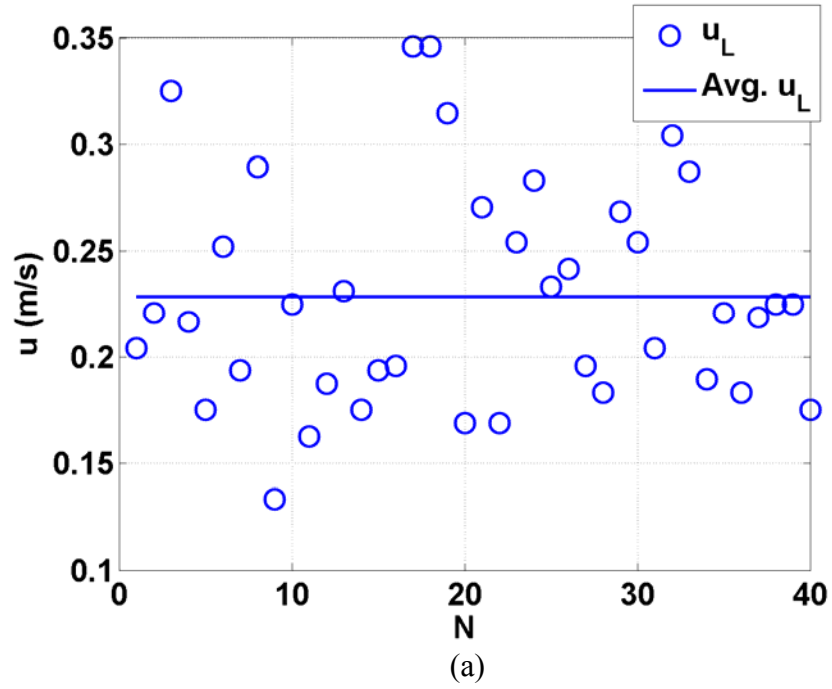


Figure 6.10. Centerline bubble velocities based on only (a) leading edges and (b) trailing edges of bubbles appeared in the field of view at $k=0$ for case 8 (average leading velocity is 0.23 m/s with $\sigma = \pm 0.05$ m/s and average trailing velocity is 0.23 m/s with $\sigma = \pm 0.03$ m/s)

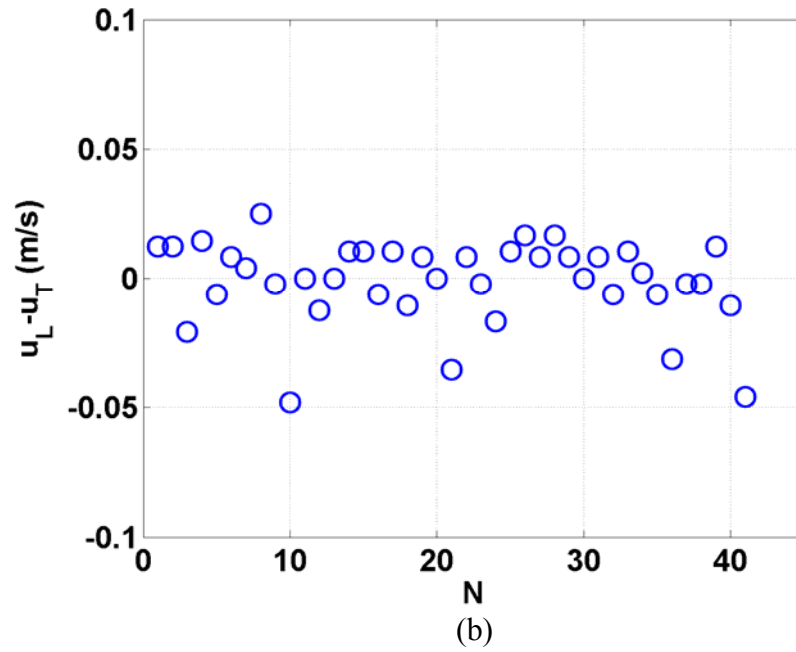
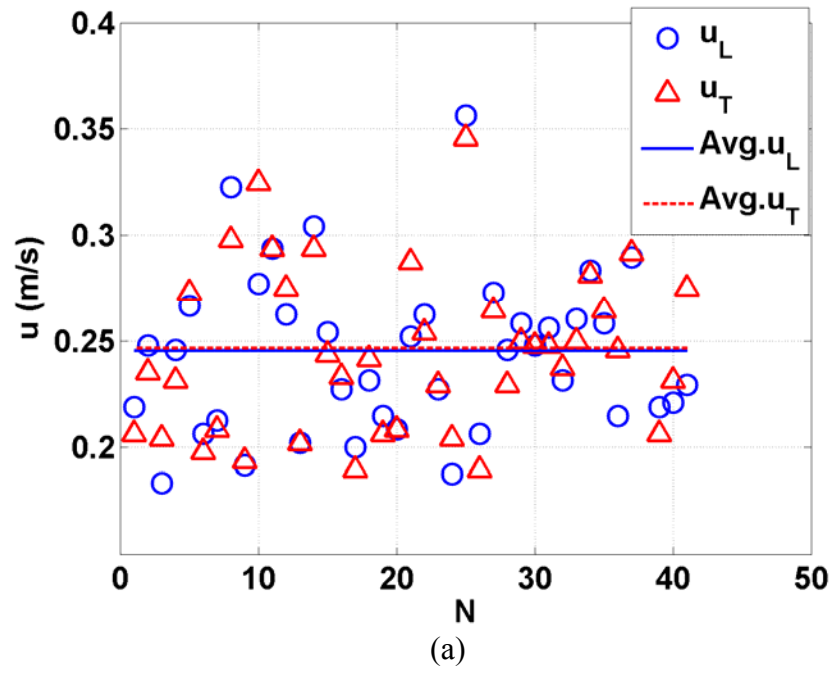


Figure 6.11. Centerline bubble velocities (a) both leading and trailing edges of bubbles appeared in the field of view and (b) velocity differences of between leading and trailing centerline velocities at $k=0$ for case 8. (average leading velocity is 0.24 m/s with $\sigma = \pm 0.04$ m/s and average trailing velocity is 0.24 m/s with $\sigma = \pm 0.04$ m/s)

Table 6.1. Slip ratios for five different cases for each branching level.

Experimental Cases	Branching Level (k)				
	k=0	k=1	k=2	k=3	k=4
Case 2	1.0	1.0	1.0	1.1	1.3
Case 4	1.0	0.7	1.0	1.0	1.0
Case 5	1.0	1.0	0.9	1.2	1.1
Case 6	1.2	1.0	1.0	1.2	1.3
Case 8	1.1	1.0	0.9	1.1	1.2

6.2.2 Void fraction comparison with existing correlations

Five different void fraction correlations are briefly discussed again in this section. The first void fraction correlation is known as the homogenous void fraction correlation, based on an assumption that local liquid and gas phase velocities are identical. In such a case, the slip ratio would result in unity. Revellin et al. (2006) investigated two-phase flow boiling of R134-a in a 500 μm tube and determined the void fraction using the slip ratio. The vapor velocity was measured using a pair of lasers and photo-detectors. The cross-sectional void fraction was determined by superficial gas velocity and vapor velocity using Eqs. 6.3 and 6.4.

$$j_g = \frac{xG}{\rho_g} \quad (6.3)$$

$$\alpha = \frac{j_g}{u_g} \quad (6.4)$$

The experimental void fraction data, based on the slip ratio, followed the homogenous void fraction model predictions.

The second void fraction correlation considered is that proposed by Armand (1946). This void fraction correlation was generated by a fit to experimental results acquired from two-phase flows of air and water. A pipe of diameter of 26 mm was used and positioned horizontally. The void fraction was determined by measuring the mass of a two-phase mixture in a known volume. The homogenous void fraction was determined using water and air mass flow rates with their respective densities.

$$\beta = \frac{x\rho_f}{x\rho_f + (1-x)\rho_g} \quad (6.5)$$

Recall that the quality, x , is defined as the ratio of gas mass flow rate over total mass flow rate. The experimental void fraction was plotted as a function of homogeneous void fraction values, β , up to 0.9. A linear relationship between α and β was found. Void fraction correlation developed by Armand (1946) is

$$\alpha = 0.833\beta \quad (6.6)$$

which predicts void fractions slightly below those from the homogenous model.

The third void fraction correlation, proposed by Zivi (1964), was mathematically derived by taking the derivative of the two-phase kinetic energy flux with respect to void fraction. To get a relation for void fraction, the derivative of the kinetic energy flux was set by zero, the result corresponding to the minimum kinetic energy. The void fraction equation is computed from the quality and density (or

specific volume) ratio of the two phases. In Eq. 6.7, specific volume is used instead of using density.

$$\alpha = \frac{1}{1 + \left(\frac{1-x}{x} \right) \left(\frac{v_f}{v_g} \right)^{\frac{2}{3}}} \quad (6.7)$$

The fourth void fraction correlation is that proposed by Chisholm (1973). The void fraction is based on the homogeneous theory and a basic mass balance. In this case, the slip ratio is defined in terms of the square root of the density ratio instead of a velocity ratio.

$$\alpha = \left[1 + \sqrt{1 - x \left(1 - \frac{\rho_f}{\rho_g} \right) \left(\frac{1-x}{x} \right) \left(\frac{\rho_g}{\rho_f} \right)} \right]^{-1} \quad (6.8)$$

The fifth, and last, void fraction correlation was developed from experimental results from nitrogen gas and water two-phase flow studies in a 100 μm tube acquired by Chung et al. (2004). The experimental void fraction was determined by time-averaging bubble area using image processing. As in the present investigation, these are two-dimensional or apparent void fractions.

$$\alpha = \frac{0.03\sqrt{\beta}}{1 - 0.97\sqrt{\beta}} \quad (6.9)$$

6.2.3 Comparisons of void fractions

Figure 6.12 shows void fractions computed with the slip ratio, α_{slip} , and void fractions determined from two-dimensional images, α_{image} , plotted as a function of

homogenous void fraction, β . Results in Fig. 6.12 are restricted to the $k=0$ branch level. Black squares represent the experimental void fraction resulting from slip ratio, and pink circles represent experimental void fraction based on area-averaged images. Also, shown in Fig. 6.12 are the homogeneous, Armand (1946), Zivi (1964), Chisholm (1973) and Chung et al. (2004) void fraction correlations. The experimental void fraction determined using the slip ratio, α_{slip} , follows the homogeneous behavior, a result also observed by Revellin et al. (2006). However, the experimental void fraction determined using the area-averaged images, α_{image} , has a noticeably different trend from that predicted for homogeneous flow. Rather, the image based void fractions are slightly underpredicted by both the Zivi (1964) and Chung et al. (2004) void fraction correlations between the homogeneous void fraction values of 0.2 and 0.7. In Figs. 6.13 and 6.14, the experimental void fractions versus homogeneous void fraction are plotted for $k=2$ and $k=4$ branch levels, respectively. Void fraction data based on the slip ratio, in both Figs. 6.13 and 6.14, exhibit behavior similar to homogeneous. This trend was previously observed in Fig. 6.12. The image-based void fraction data from in Figs. 6.13 and 6.14 are better predicted with Zivi (1964) correlation than the image-based void fraction observed in Fig. 6.12. Figure 6.15 shows α versus β plots of image-based void fraction data for all levels of k . Generally speaking, most void fraction data based on area-averaged images follow better predictions from the Zivi (1964) void fraction correlation than they do the homogenous or Chung et al. (2004) correlations. On the other hand, area-averaged void fraction data from this study also exhibit a similar trend as that predicted by Chung et al. (2004). As is evident from Fig.

6.15, Chung et al. (2004) seems to underestimated void fraction for the present study more than does the correlation by Zivi (1964). This may be a consequence of the diameter of the channel used in the study of Chung et al. (2004). It was a 100 μm diameter tube, which is smaller than the smallest hydraulic diameter of 143 μm at the $k=4$ level in present study.

In summary, the experimental void fractions based on slip ratios, both in the present study and in Revellin et al. (2006) demonstrate linear variations with the homogenous void fraction and, therefore, agree best with predictions from the homogeneous flow correlation and the Chisholm (1973) correlation. The correlation of Chisholm (1973) incorporates the slip ratio. On the other hand, the imaged-based void fraction data in the present study agree best with those correlations based on image processing and on kinetic energy theory, as reported in Chung et al. (2004) and Zivi (1964), respectively. A suggestion as to which void fraction correlation should be used in pressure drop models requires a comparison of predictive models using several different void fraction correlations with pressure drop values measured experimentally. The closest study performed in a similar fractal-like flow network is that of Daniels et al. (2008) for adiabatic flow boiling, i.e., with vapor and liquid. The void fraction correlation in the pressure drop model that best predicted experimental results was that of Zivi (1964) and Chung et al. (2004). The two-phase multiplier used also was found influence the results. Direct comparison between the two studies is not possible due to differences in length scale ratios, which is 1.4 for the present study and 0.71 in Daniels et al. (2008), and in the type and rates of flow of the two phases.

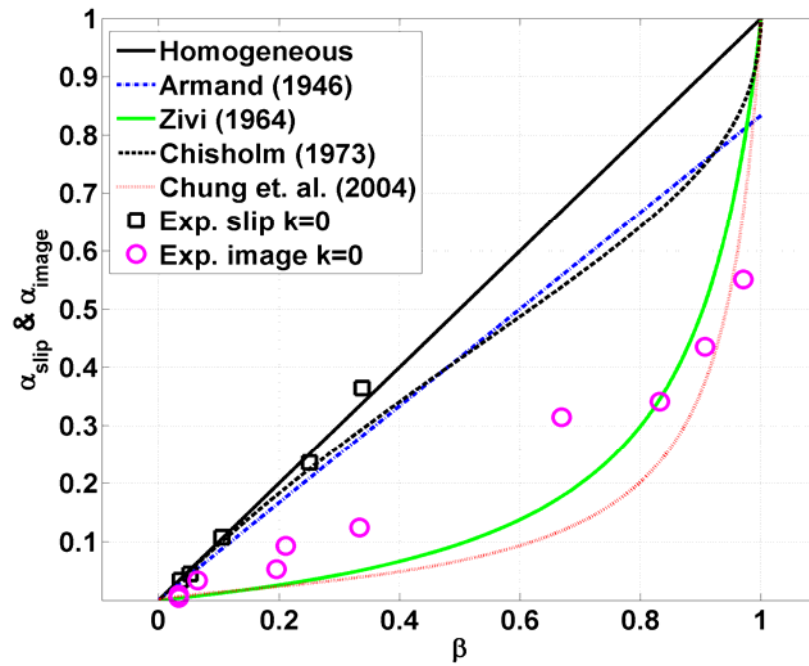


Figure 6.12. α_{slip} and α_{image} v.s. β for $k=0$ branching level with void fraction correlations

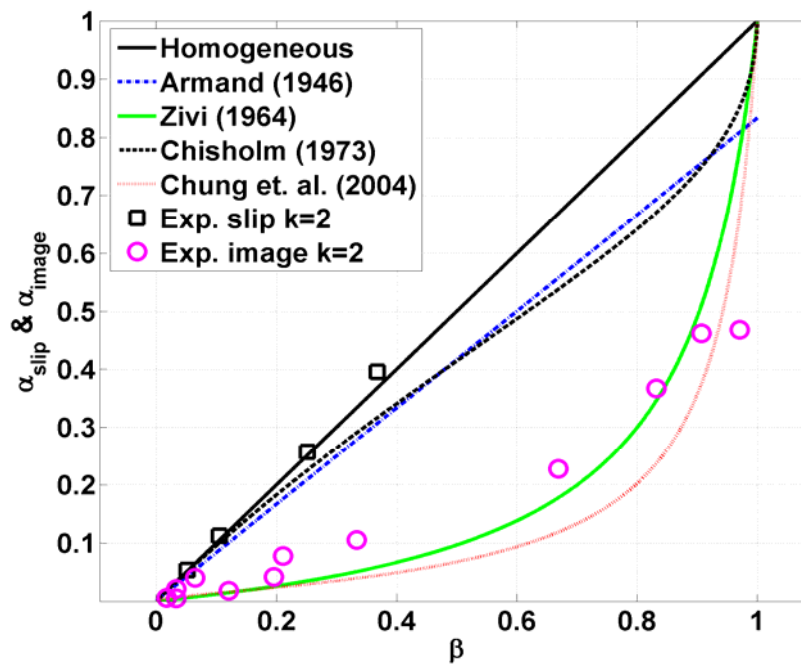


Figure 6.13. α_{slip} and α_{image} v.s. β for $k=2$ branching level with void fraction correlations.

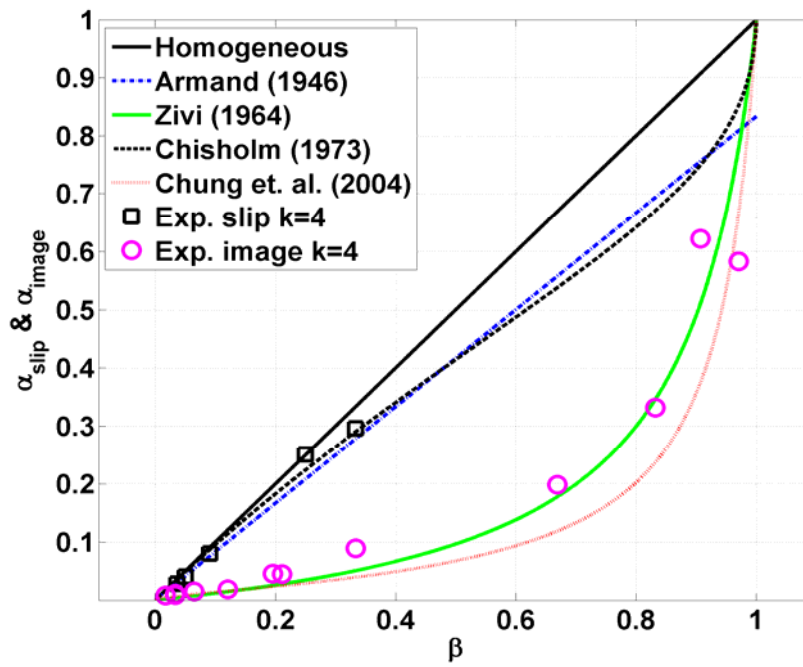


Figure 6.14. α_{slip} and α_{image} v.s. β for $k=4$ branching level with void fraction correlations.

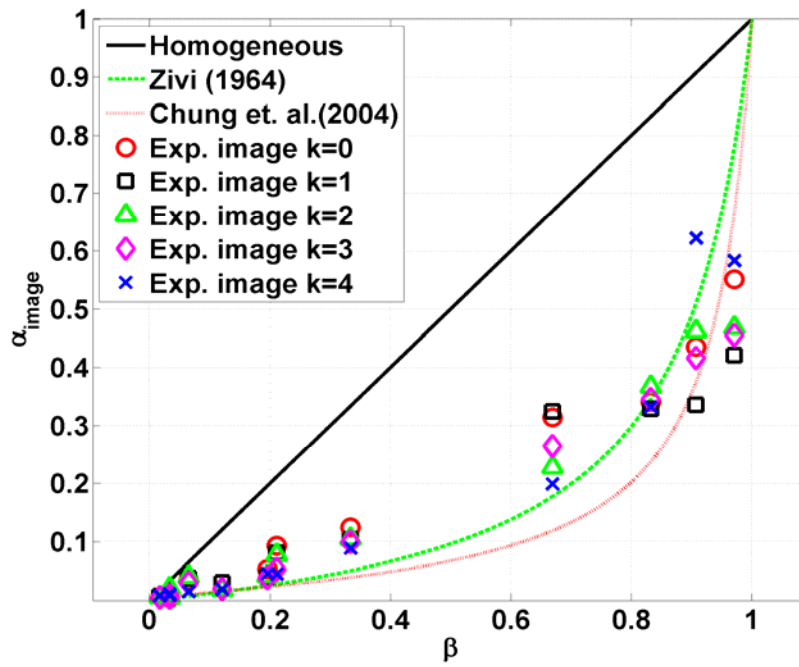


Figure 6.15. α_{image} v.s. β for all branching level with void fraction correlations of homogeneous, Zivi (1964), Chung et al. (2004).

6.3 Two-Phase Velocity Vector Fields

In this section, two-phase velocity vector fields and contours are discussed at three of the four different bifurcation regions. For this qualitative study, water and air inlet mass flow rates were set to 20 g/min and 0.01 g/min, respectively. These flow rates correspond with test case 8. As noted from Table 4.1, these experimental mass flow rates yield, in the $k=0$ level, the highest superficial gas velocity of 0.113 m/s and a superficial liquid velocity of 0.21 m/s. Figure 6.16 shows two-dimensional velocity vector fields at the bifurcation between the $k=0$ and $k=1$ level. The streamwise, u , and spanwise, v , velocities are the two components contributing to the magnitudes shown on contour plots. Figure 6.16a shows a liquid only flow field at the bifurcation. The left-most figure shows the original PIV image, in which the seeding is clearly visible throughout the bifurcation. The middle image in fig. 6.16a is a velocity vector field and the right-most figure represents the u - v component contour plots of the velocity magnitude. The maximum liquid velocity, approximately 0.45 m/s, is observed at the center of the $k=0$ channel. An overall decrease in velocity magnitudes is observed in the bifurcation section as a result of the increasing cross-sectional flow area. The liquid flow then accelerates as it enters the two downstream $k=1$ level channels. Flow acceleration is strongest near the stagnation point (or inner walls) splitting the two downstream flow channels. The strongest deceleration occurs near the outer walls inside the bifurcation section. Such a finding suggests a region of potential hot spots when used for cooling applications and, hence, the need for continued design studies.

Figure 6.16b presents two phases flowing through the same bifurcation shown in Fig. 6.16a. Evident from the raw micro-PIV images is that a relatively long slug recently passed through the bifurcation section and symmetrically split between the $k=1$ branching channels. In this figure that slug is about to be pinched into two new slugs. Meanwhile, another slug flow is observed entering the bifurcation section. Evident from the velocity vector and contour plots are that velocities are highest at the leading edge of this slug.

Another instance of symmetric two-phase flow in this same bifurcation between the $k=0$ and $k=1$ branch levels is shown in the raw image shown in Fig. 6.17a. Two small bubbles with similar diameters of approximately $200\text{ }\mu\text{m}$ are observed in the $k=0$ channel and just inside the bifurcation. Recall that the $k=0$ level channels are approximately $400\text{ }\mu\text{m}$ wide. Also observed in Fig. 6.17a is a slug that symmetrically split into the two $k = 1$ branch levels. In Fig. 6.17c, secondary flow structures are observed at the bifurcation between the $k = 0$ and $k = 1$ levels. Figure 6.17d is an enlarged view of the flow field near outer wall of the $k=1$ channel. This region, identified by a dashed red box in Fig. 6.17c, clearly experiences reverse flow between the wall and the edge of the bubble. In this enlarged view, the liquid near the inside wall of the $k=1$ channel is observed to accelerate toward the bubble interface. This local liquid acceleration causes liquid to be drawn from the thick liquid film between the outer wall and the bubble, resulting in liquid backflow and recirculation around the trailing interface of the bubble.

Figure 6.18 shows a case in which the two phases exhibit asymmetrical flow at this same bifurcation between the $k=0$ and $k=1$ levels. Although, in general, large slugs were observed to symmetrical split at a bifurcation, smaller bubbles do not. Observed in the raw image in Fig. 6.18a, a small bubble moves into the right channel following the bifurcation. Due to the flow resistance caused by its presence, a slightly larger bubble approaching from behind tends toward the left channel following the bifurcation. The smaller bubble begins to accelerate in the right channel, as the flow area in this channel is considerably smaller than that in the bifurcation. A region of high velocity flow is observed from the velocity magnitude contour in Fig. 6.18b. As the larger bubble tries to squeeze past the smaller bubble into the left channel, a region of rotational flow is observed in the triangular region between the two bubbles and the outer wall of the bifurcation.

Figure 6.19 presents, at the bifurcation section between the $k=1$ and $k=2$ levels, (a) a liquid only flow field and (b) a two-phase flow field exhibiting symmetrical flow behavior. Included are raw images, u - v velocity vector fields, and u - v velocity magnitude contours. Evident from Fig. 6.19a is a maximum velocity along the centerline of the $k=1$ channel that is approximately 0.34 m/s. As in the upstream bifurcation, liquid flow in front of a bubble is observed to accelerate in Fig. 6.19b. Likewise, reverse flow occurs in the thick liquid film between the wall and the trailing edge of a recently split bubble, as is evident from Fig. 6.20.

Single phase and two-phase flows in the last bifurcation section, i.e., between the $k=3$ and $k=4$ levels, are shown in Fig. 6.21a and 6.21b, respectively. Again these

images were taken under flow conditions corresponding to case 8. The image in Fig. 6.21a was acquired when no bubbles were in the flow field, i.e., only a liquid phase is present. This is evident from the raw image in which the entire flow field is seeded. As in previous figures, both velocity vectors and velocity magnitude contours are also shown in Fig. 6.21a. According to the magnitude contour plot, the flow through the left downstream channel of the $k=4$ branch appears less than that through the right downstream channel. This is likely due to the presence of a vapor bubble located near or at the exit of this channel, the surface tension of which causes a flow resistance different from that experienced by the right downstream channel.

In Figure 6.21b, asymmetric two-phase flow is observed at the bifurcation section. A bubble inside the bifurcation appears to find the instantaneous flow resistance to enter the left downstream $k=4$ channel lower than the resistance to enter the right channel. As the bubble squeezes into the left channel, the flow resistance is sufficient to accelerate the liquid into the right channel of the $k=4$ level.

In general, gas slugs were observed to split uniformly into downstream channels at the bifurcation sections, whereas bubbles tended not to split. The presence of downstream bubbles, either inside the flow network or adhering to the periphery of the disk, is hypothesized as a possible cause flow resistances and, hence, a possible cause for the non-uniformity of flow through the channels within the same branch level.

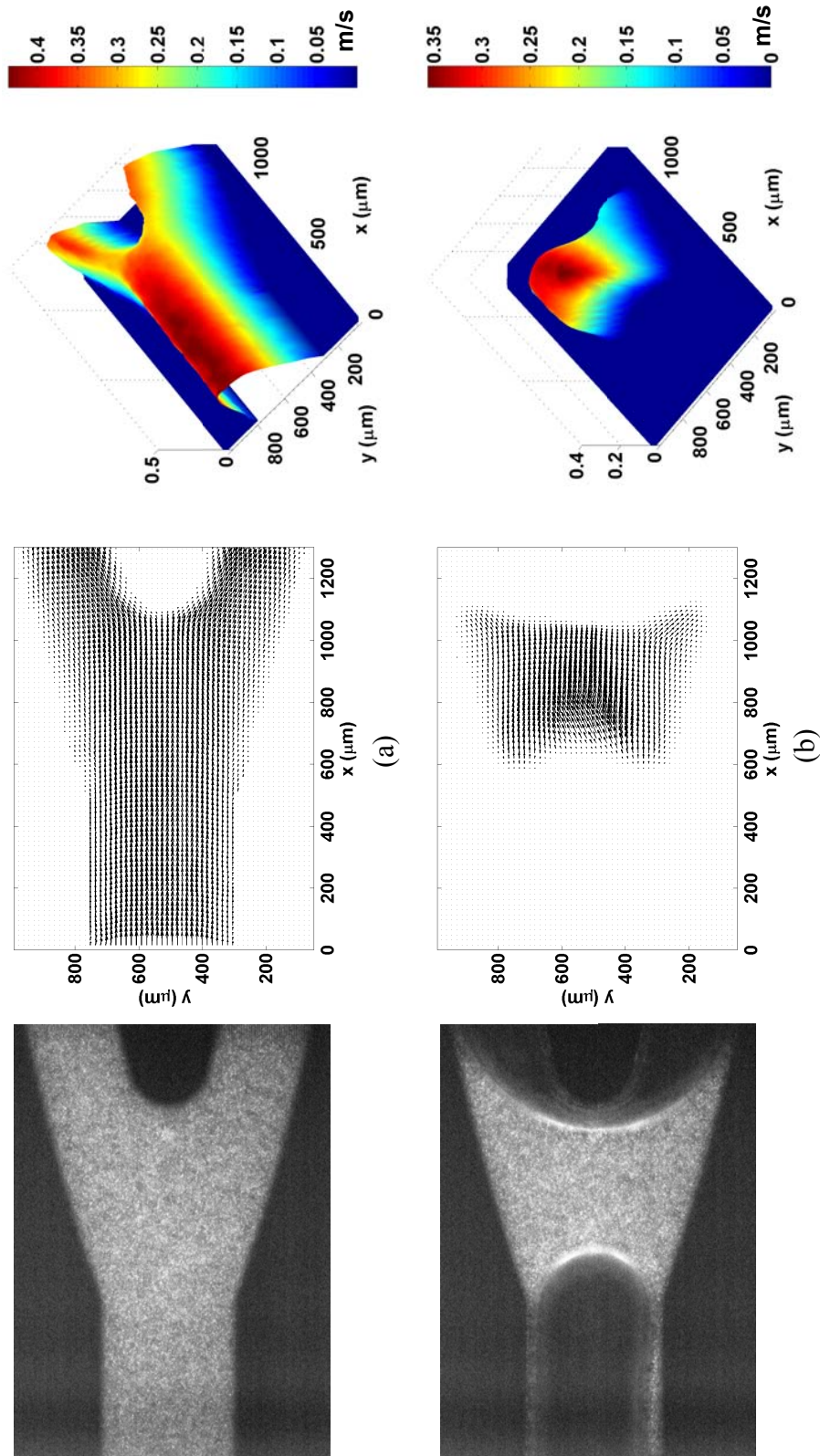


Figure 6.16. Experimental 2-D velocity vector fields at the bifurcation between $k=0$ and $k=1$ with u - v component contour plots. (a) liquid only, (b) bubble presence.

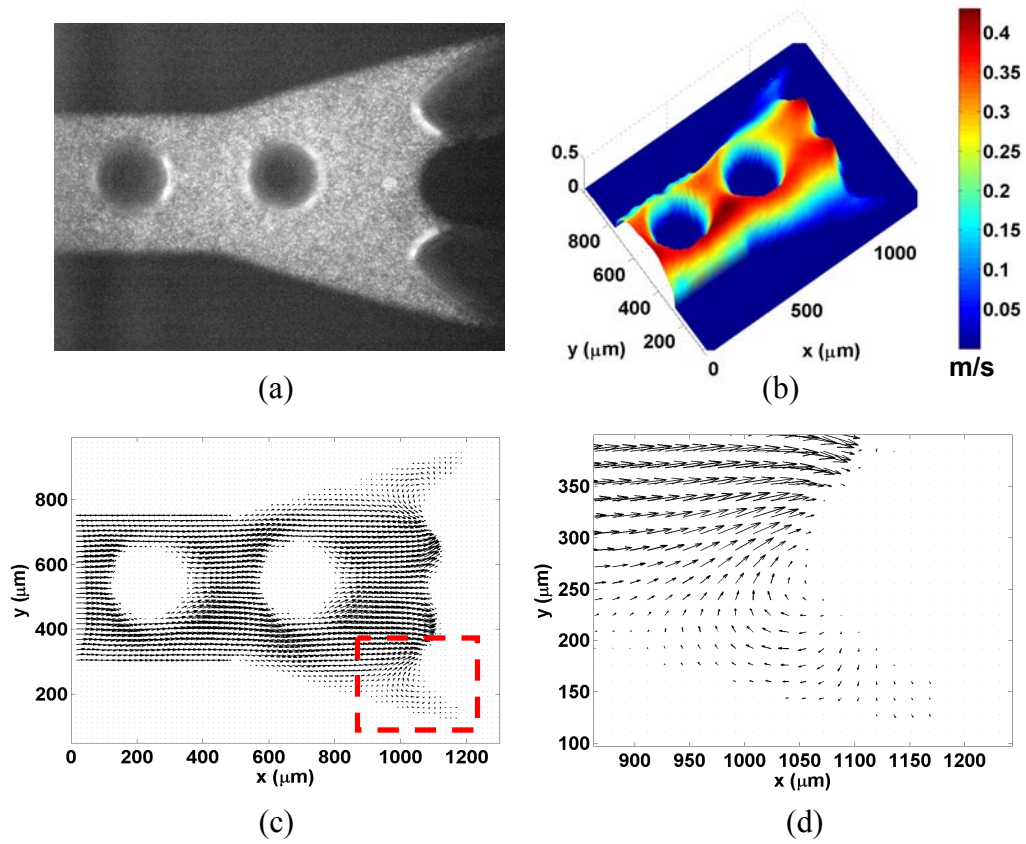


Figure 6.17. Experimental 2-D velocity vectors and contour at bifurcation between $k=0$ and $k=1$. (a) original micro-PIV image, (b) contour plot, (c) vector plot, (d) zoomed in dotted box.

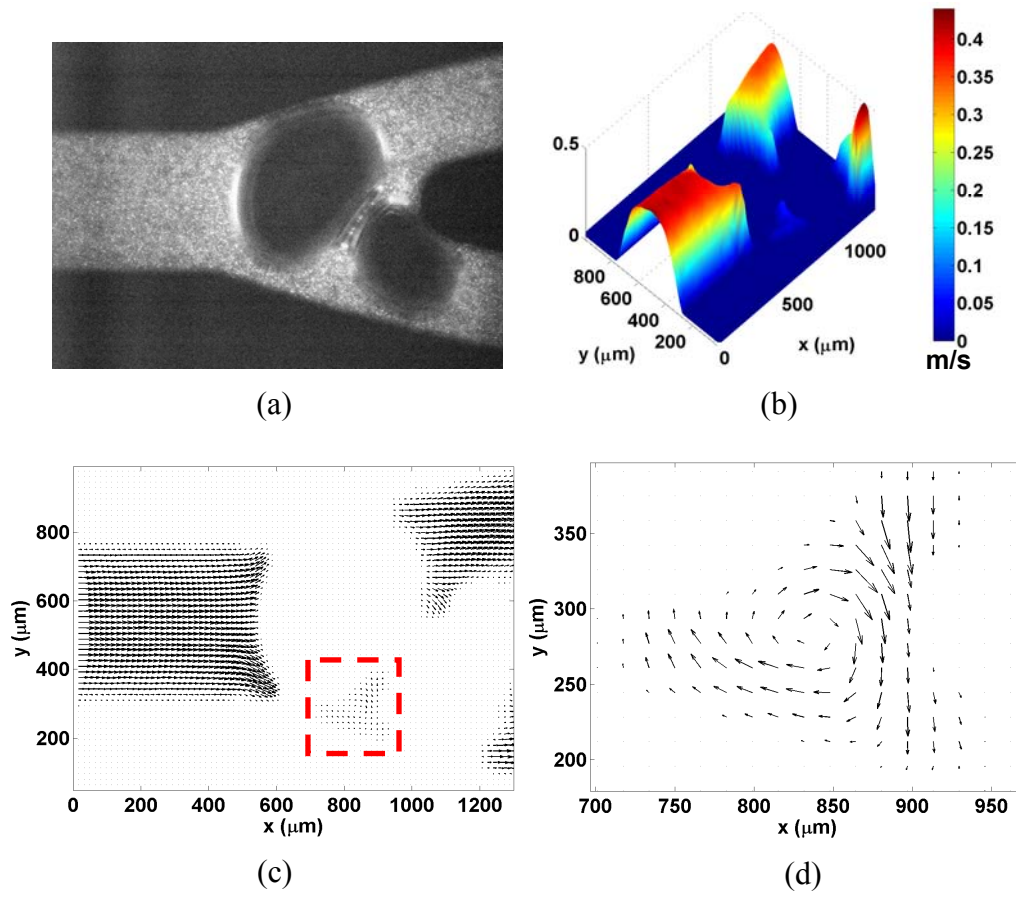


Figure 6.18. Experimental 2-D velocity vectors and contour at bifurcation between $k=0$ and $k=1$. (a) original micro-PIV image, (b) contour plot, (c) vector plot, (d) zoomed in dotted box.

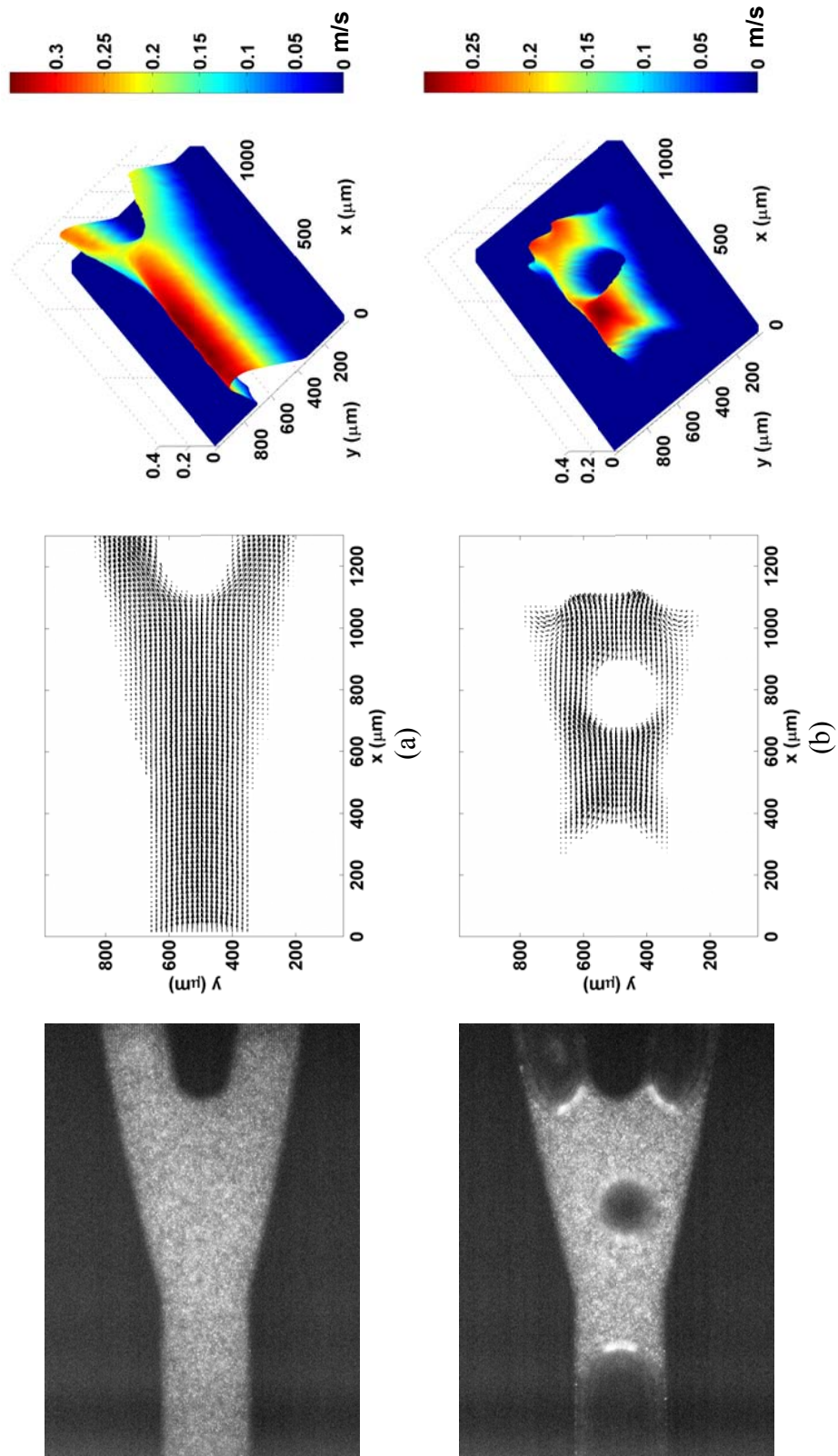


Figure 6.19. Experimental 2-D velocity vector fields at the bifurcation between $k=1$ and $k=2$ with u - v component contour plots. (a) liquid only, (b) bubble presence.

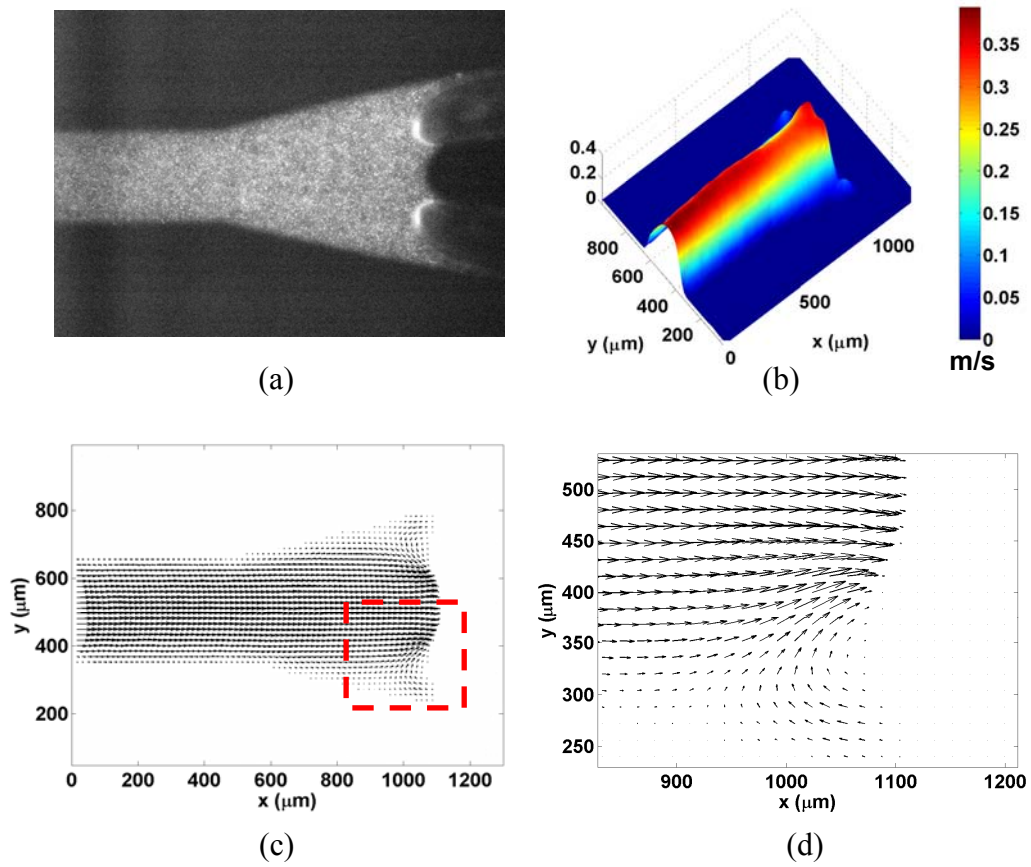


Figure 6.20. Experimental 2-D velocity vectors and contour at bifurcation between $k=1$ and $k=2$. (a) original micro-PIV image, (b) contour plot, (c) vector plot, (d) zoomed in dotted box.

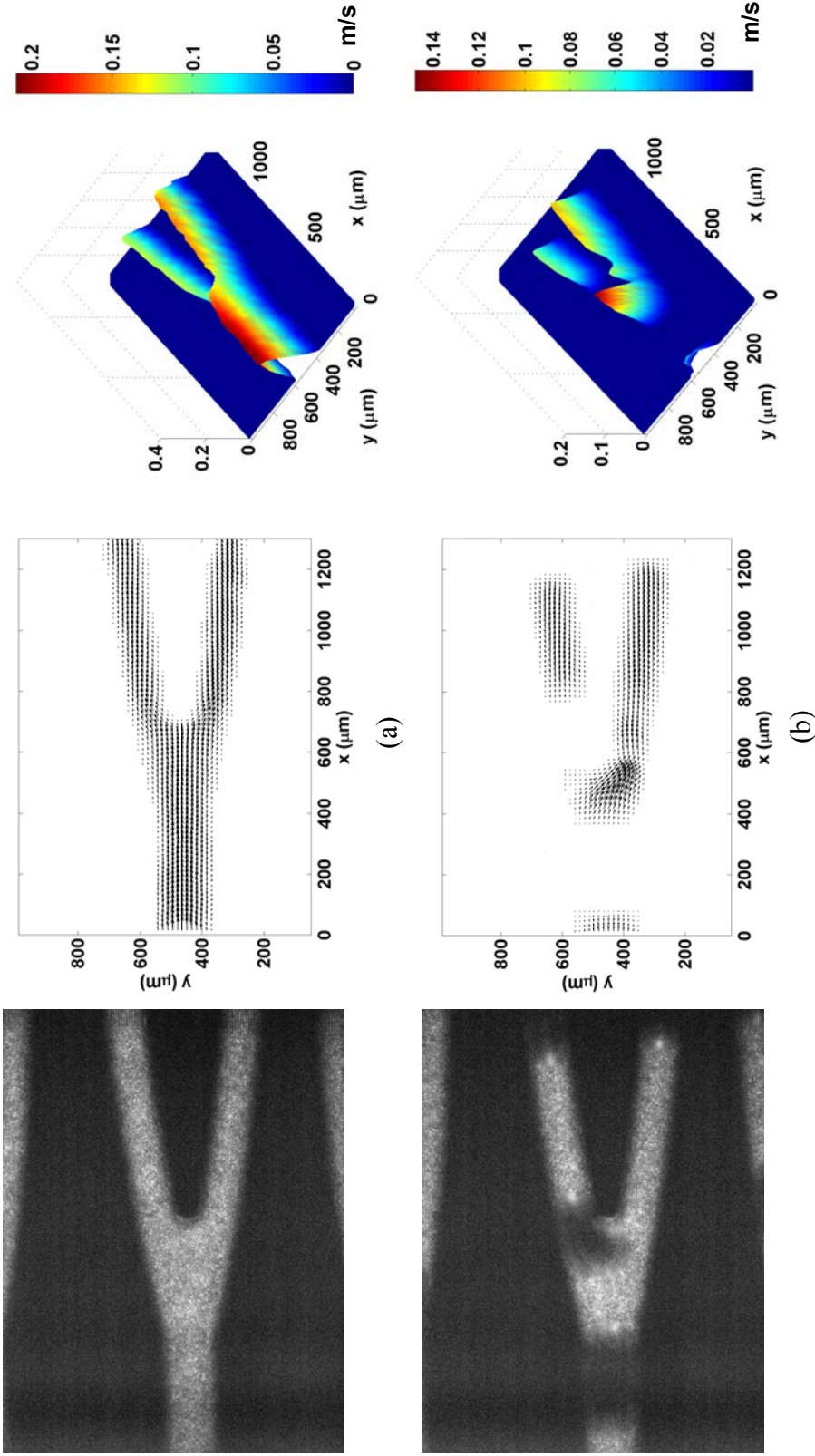


Figure 6.21. Experimental 2-D velocity vector fields at the bifurcation between $k=3$ and $k=4$ with u-v component contour plots. (a) liquid only, (b) bubble presence.

CHAPTER 7

CONCLUSIONS AND RECOMMENDATIONS

7.1 Conclusions

In this study two-phase air-water flows were used to investigate two-phase flow patterns and flow regime maps, and to assess the validity of existing void fraction correlations. Two different methods were used to assess void fraction, one based on the slip ratio and the other using area-averaged images, time-averaged over the length of a movie sequence. The slip ratio is defined as the local gas velocity over the local liquid velocity. An average of the maximum centerline velocity of the liquid phase was measured by micro-PIV in the fully developed region of the flow field. Using the experimentally measured maximum velocity, the average cross-sectional velocity was computed using the three-dimensional theoretical equation derived by Shah and London (1978). To assess gas velocity, the average velocity of the interfaces between the gas and liquid phase was determined using image analysis techniques.

Flow regime maps were generated using the Taitel and Dukler (1976) model for all levels in a fractal-like branching channel network. Twelve test cases were considered, with ranges of superficial air and water velocities between 0.007 m/s and 1.8 m/s and between 0.05 m/s and 0.42 m/s, respectively. Four different two-phase flow patterns, including bubbly, slug, ring and annular flows were observed and plotted on the flow regime maps. The Taitel and Dukler (1976) well predicted the flow regimes observed. Slug flow increased in prevalence as the two-phase flow migrated

toward the smaller channels for a fixed flow condition. Likewise, in general, slug flow became more predominate with decreases in superficial liquid flow rates or increases in superficial gas flow rate, in agreement with expectations from the Taitel and Dukler (1976) predictions.

For void fraction assessment using the slip ratio, five test cases were selected from the twelve conditions considered for regime mapping. Void fractions computed with the slip ratio and image analysis were compared with existing void fraction correlations. Results were plotted as a function of homogenous void fraction. In addition to having very different trends, the difference between the two assessments was significant in the homogenous void fraction range between 0.2 and 0.7. Two clearly different trends were observed at each branch level. Void fraction assessed with the slip ratio agreed very well with predictions from the homogeneous void fraction correlation. On the other hand, area-averaged void fraction determined from image processing showed better agreement with the void fraction correlation proposed by Zivi (1964). A clear recommendation of a specific void fraction correlation for predictive model is not presently obvious.

General observations of two-phase flows at several bifurcation sections for the flow conditions corresponding with case 8 were made. Given the symmetrical geometry of the fractal-like branching channel network, most two-phase slug flows observed exhibited symmetrical behavior. However, asymmetric two-phase flow behavior was observed when small bubbles traveled through the bifurcation sections. Bubbles too small to be split tend to flow down one downstream branch or the other,

the path taken likely influenced by downstream resistances. Slow flow regions near the outside walls in the bifurcation were observed. In addition, strong in-plane secondary flows are observed behind recently slip slugs and between bubble-bubble interactions.

7.2 Recommendations

Based on the results of the present study, several recommendations have been considered and are presented for consideration.

1. Code a two-phase, adiabatic gas-liquid flow model for predicting pressure drop in fractal-like branching flow networks. Vary which void fraction correlation is employed in the code and compare predicted pressure drops to those measured experimentally.
2. Use observed bubble curvature to extrapolate two-dimensional bubble images into three dimensional bubble images and reassess the void fraction in comparison with existing correlations. It is expected voids in channels wider than they are deep will fill the entire cross-section, save a film region surrounding the bubble. Voids in channels narrower than they are deep may either be axisymmetric or fill the cross-section. Both cases should be considered.
3. The Taitel and Duklar (1976) model should be assessed for its ability to predict two-phase boiling flows, both adiabatic and diabatic.

4. Finally, to minimize the potential for flow asymmetries resulting from flow resistances created by a gas bubble residing at the periphery of the flow network disk, submersion of the exit in water is suggested.

BIBLIOGRAPHY

Adrian, R.J., "Particle-Imaging Techniques for Experimental Fluid Mechanics," *Annual Rev. Fluid Mech.*, v. 23, pp. 261-304, 1991.

Alharbi, A.Y., D.V. Pence, and R.N. Cullion, "Fluid Flow through Microscale Fractal-Like Branching Channel Networks," *Journal of Fluids Engineering*, v. 125, no. 6, pp.1051-1057, 2003.

Alharbi, A.Y., D.V. Pence, and R.N. Cullion, "Thermal Characteristics in Micro-Scale Fractal-Like Branching Channels," *Journal of Heat Transfer*, v. 126, no. 5, pp. 744-752, 2004.

Armand, A.A., "The Resistance During The Movement of A Two-Phase System in Horizontal Pipes," *Izvestiya Vsesoyuznogo Teplotekhnicheskogo Instituta*, v.1, pp. 16-23, 1946.

Bao, Z.Y., D.F. Fletcher, and B.S. Haynes, "Flow Boiling Heat Transfer of Freon R11 and HCFC123 in Narrow Passages," *International Journal of Heat and Mass Transfer*, v. 43, pp. 3347-3358, 2000.

Beak, V., "The Resistance During The Movement of A Two-Phase System in Horizontal Pipes," *A.E.R.E. Transactions* 828, 1959.

Bejan, A. "Constructal Tree Network for Fluid Flow between a Finite-Size Volume and One Source or Sink," *Rev. Gen Therm*, v. 36, pp. 592-604, 1997.

Chisholm, D., "Void Fraction During Two-Phase Flow," *Journal Mechanical Engineering Science*, v. 13, no. 3, pp. 235-236, 1973.

Chung, P.M.-Y., and M. Kawaji, "The Effect of Channel Diameter on Adiabatic Two-Phase Flow Characteristics in Microchannels," *International Journal of Multiphase Flow*, v. 30, pp. 735-761, 2004.

Chung, P.M.-Y., M. Kawaji, A. Kawahara, and Y. Shibata, "Two-Phase Flow through Square and Circular Microchannels-Effects of Channel Geometry," *Journal of Fluids Engineering*, v. 126, pp. 546-552, 2004.

Collier, J.G. and J.R. Thome, "Convective Boiling and Condensation," Oxford Engineering Science Series, no. 38, Oxford University Press, USA, 1996.

Cullion, R.N., D.V. Pence, J.A. Liburdy and V. Narayanan, "Void Fraction Variations in a Fractal-Like Branching Microchannel Network," *Heat Transfer Engineering*, v. 20, no. 10, pp. 806-816, 2007.

Daniels, B., J.A. Liburdy, and D.V. Pence, "Adiabatic Flow Boiling in Fractal-Like Microchannels," *ECI International Conference on Boiling Heat Transfer*, Spoleto, May 7-12, 2006.

Daniels, BJ, J.A. Liburdy, and D.V. Pence, "Experimental Studies of Adiabatic Flow Boiling in Fractal-Like Branching Micro-Channels," *Proceedings of the ASME IMECE2008*, Paper #IMECE2008-69240, submitted.

Daniels, B.J., D.V. Pence, and J.A. Liburdy, "Predictions of Flow Boiling in Fractal-Like Branching Microchannels," *Proceedings of the ASME International Mechanical Engineering Conference and Exposition*, ASME-FED, v. 261, pp. 359-368, 2005.

Dupont, V., J.R. Thome, and A.M. Jacobi, "Heat Transfer Model for Evaporation in Microchannels. Part II: Comparison with the Database," *International Journal of Heat and mass Transfer*, v. 47, pp.3387-3401, 2004.

Enfield, K., D.V. Pence, and V. Narayanan, " Optimization of Single-Phase Microscale Fractal-Like Branching Flow Heat Sinks," *ECI Conference on Heat Transfer and Fluid Flow in Microscale*, Castelveccchio Pascoli, September 25-30, 2005.

Heymann, D., Y. Kwak, E. Edward, J. Liburdy, V. Narayanan, and D. Pence, "Area-Averaged Void Fraction Analysis of Flow Boiling in A Microscale Branching Channel Network," *Proceedings of IPACK2007, ASME InterPack'07*, Vancouver, British Columbia, Canada, July 8-12, 2007

Heymann, D., K. Enfield, D. Pence and V. Narayanan, "Gradient-Based Optimization of Single-Phase Microscale Fractal-like Branching Channel Heat Sinks," accepted for publication and presentation at the *Engineering Conference International Heat Transfer and Fluid Flow in Microscale III*, Whistler, BC, Canada, September 21-26, 2008.

Jacobi, A.M., and J.R. Thome, "Heat Transfer Model for Evaporation of Elongated Bubble Flows in Microchannels," *Journal of Heat Transfer*, v. 124, pp. 1131-1136, 2002.

Kawaji, M., and P.M.-Y. Chung, "Adiabatic Gas-Liquid Flow in Microchannels," *Microscale Thermophysical Engineering*, v. 8, pp. 239-257, 2004.

Kitagawa, A., K. Hishida, and Y. Kodama, "Flow Structure of Microbubble-Laden Turbulent Channel Flow Measured by PIV Combined with the Shadow Image Technique," *Experiments in Fluids*, v. 38, pp. 466-475, 2005.

Klank, H., G. Goranovic, J.P. Kutter, H. Gjelstrup, J. Michelsen, and C.H. Westergaard, "PIV Measurements in a Microfluidic 3D-Sheathing Structure with Three-Dimensional Flow Behaviour," *Journal of Micromechanics and Microengineering*, v. 12, pp. 862-869, 2002.

Kwak, Y., "Particle Image Velocimetry Studies of Low Reynolds Number Flows in Branching Flow Networks," M.S. thesis, Oregon State University, Corvallis, Oregon, 2003.

Meinhart, C.D., S.T. Wereley, and J.G. Santiago, "PIV Measurements of a Microchannel Flow," *Experiments in Fluids*, v. 27, pp. 414-419, 1999.

Obot, N.T., "Toward a Better Understanding of Friction and Heat/Mass Transfer in Microchannels – A Literature Review," *Proceedings of the International conference on Heat Transfer and Transport Phenomena in Microscale*, Banff, Canada, pp. 72-79, 2000

Park, J.S., C.K. Choi, and K.D. Kihm, "Optically Sliced Micro-PIV Using Confocal Laser Scanning Microscopy (CLSM)," *Experiments in Fluids*, v. 37, pp. 105-119, 2004.

Pence, D.V., "Reduced Pumping Power and Wall Temperature in Microchannel Heat Sink with Fractal-Like Branching Channel Networks," *Microscale Thermophysical Engineering*, v. 6, pp. 319-330, 2002.

Pence, D. and K. Enfield, "Inherent Benefits in Microscale Fractal-like Devices for Enhanced Transport Phenomena," *Design and Nature 2004*, Eds. M. Collins and C.A. Brebbia, WIT Press, pp. 317-328, Rhodes, Greece, 2004.

Peng, X.F., and G.P. Peterson, "Convective Heat Transfer and Flow Friction for Water Flow in Microchannel Structures," *International Journal of Heat and Mass Transfer*, v. 39, no. 12, pp. 2599-2608, 1996.

Polonsky, S., D. Barnea, and L. Shemer, "Averaged and Time-Dependent Characteristics of the Motion of an Elongated Bubble in a Vertical Pipe," *International Journal of Multiphase Flow*, v. 25, pp.795-812, 1999.

Revellin, R., D. Vincent, T. Ursenbacher, J.R. Thome, and I. Zun, "Characterization of Diabatic Two-Phase Flows in Microchannels: Flow Parameter Results for R-134a in A 0.5 mm Channel," *International Journal of Multiphase Flow*, v. 32, pp. 755-774, 2006.

Revellin, R., B. Agostini, T. Ursenbacher, and J.R. Thome, "Experimental Investigation of Velocity and Length of Elongated Bubbles for Flow of R-134a in A 0.5 mm Microchannel," *Experimental Thermal and Fluid Science*, v. 32, pp. 870-881, 2008.

Qu, W., and I. Mudawar, "Flow Boiling Heat Transfer in two-Phase Micro-Channel Heat Sinks – I. Experimental Investigation and Assessment of Correlation Methods," *International Journal of Heat and Mass Transfer*, v. 46, pp. 2755-2771, 2003.

Santiago, J.G., S.T. Wereley, C.D. Meinhart, D.J. Beebe, and R.J. Adrian, "A Particle Image Velocimetry Sytem for Microfluidics," *Experiments in Fluids*, v. 25, pp. 316-319, 1998.

Serizawa, A., Z. Feng, and Z. Kawara, "Two-Phase Flow in Microchannels," *Experimental Thermal and Fluid Science*, v. 26, pp. 703-714, 2002.

Shah, R.K. and A.L. London, "Laminar Flow Forced Convection in Ducts," *Advanced in Heat Transfer*, Supplement 1, Academic Press, New York, 1978.

Sobhan, C.B., and S.V. Garimella, "A Comparative Analysis of Studies on heat Transfer and Fluid Flow in Microchannels," *Microscale Thermophysical Engineering*, v. 5, pp. 293-311, 2001.

Steinke, M.E., and S.G. Kandlikar, "An Experimental Investigation of Flow Boiling Characteristics of Water in Parallel Microchannels," *Journal of Heat Transfer*, v. 126, pp.518-526, 2004.

Taitel Y. and A.E. Dukler, "A Model for Predicting Flow Regime Transitions in Horizontal and Near Horizontal Gas-Liquid Flow," *AIChE Journal*, v. 22, no. 1, pp. 47-55, 1976.

Thome, J.R., V. Dupont, and A.M. Jacobi, "Heat Transfer Model for Evaporation in Microchannels. Part I: Presentation of the Model," *International Journal of Heat and mass Transfer*, v. 47, pp.3375-3385, 2004.

Triplett, K.A., S.M. Ghiaasiaan, S.I. Abdel-Khalik, and D.L. Sadowski, "Gas-Liquid Two-Phase Flow in Microchannels Part I: Two-Phase Flow Patterns," *International Journal of Multiphase Flow*, v. 25, pp. 377-394, 1999a.

Triplett, K.A., S.M. Ghiaasiaan, S.I. Abdel-Khalik, A. LeMouel, and B.N. McCord, "Gas-Liquid Two-Phase Flow in Microchannels Part II: Void Fraction and Pressure Drop," *International Journal of Multiphase Flow*, v. 25, pp. 395-410, 1999b.

Tuckerman, D.B., and R.F.W. Pease, "High-Performance Heat Sinking for VLSI," *IEEE Electron Device Letters*, Vol. Edl-2, No. 5, 1981.

Wang, L., M. Chen, and M. Groll, "Experimental Study of Flow Boiling Heat Transfer in Mini-Tube," *Proceedings of ICMM 3rd International Conference on Microchannels and Minichannels*, Toronto, Ontario, Canada, June 13-15, 2005.

Wang, E.N., S. Devasenathipathy, C.H. Hidrovo, D.W. Fogg, J.M. Koo, J.G. Santiago, K.E. Goodson, and T.W. Kenny, "Liquid Velocity field Measurements in Two-Phase Microchannel Convection," *3rd International Symposium on Two-Phase Flow Modeling and Experimentation*, Pisa, September 22-24, 2004.

Wechsato, W., S. Lorente, and A. Bejan, "Optimal Tree-Shaped Networks for Fluid Flow in a Disc-Shaped Body," *International Journal of Heat and Mass Transfer*, v. 45, pp. 4911-4924, 2002.

West, G.B., J.H. Brown, and B.J. Enquist, "A General Model for the Origin of Allometric Scaling Laws in Biology," *Science*, Vol. 276, No. 4, pp. 122-339, 1997.

White, F.M., "Viscous Fluid Flow," McGraw Hill, New York, p. 293, 1991

Xiong, R., and J.N. Chung, "An Experimental Study of the Size Effect on Adiabatic Gas-Liquid Two-Phase Flow Patterns and Void Fraction in Microchannels," *Physics of Fluids*, v. 19, pp. 033301-1-16, 2007.

Zivi, S.M., "Estimation of Steady-State Steam Void-Fraction by Means of The Principle of Minimum Entropy Production". *Journal of Heat Transfer*, v. 86, pp. 247-252, 1964.

APPENDICES

APPENDIX A
FLUORESCENT FLOW ADDITIVES

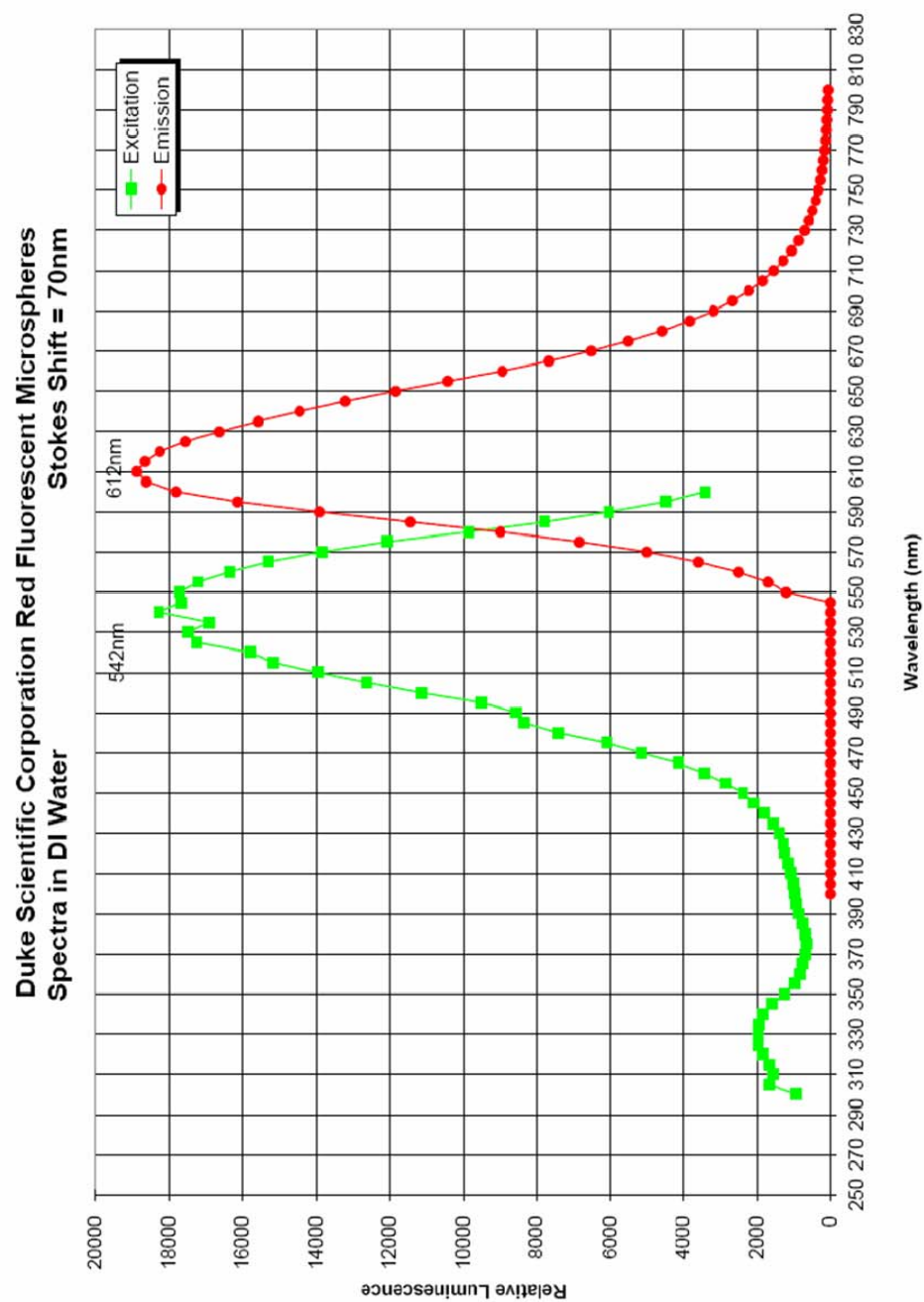


Figure A1. Wave length spectra of fluorescent particles (approved by Duke Scientific Co.)

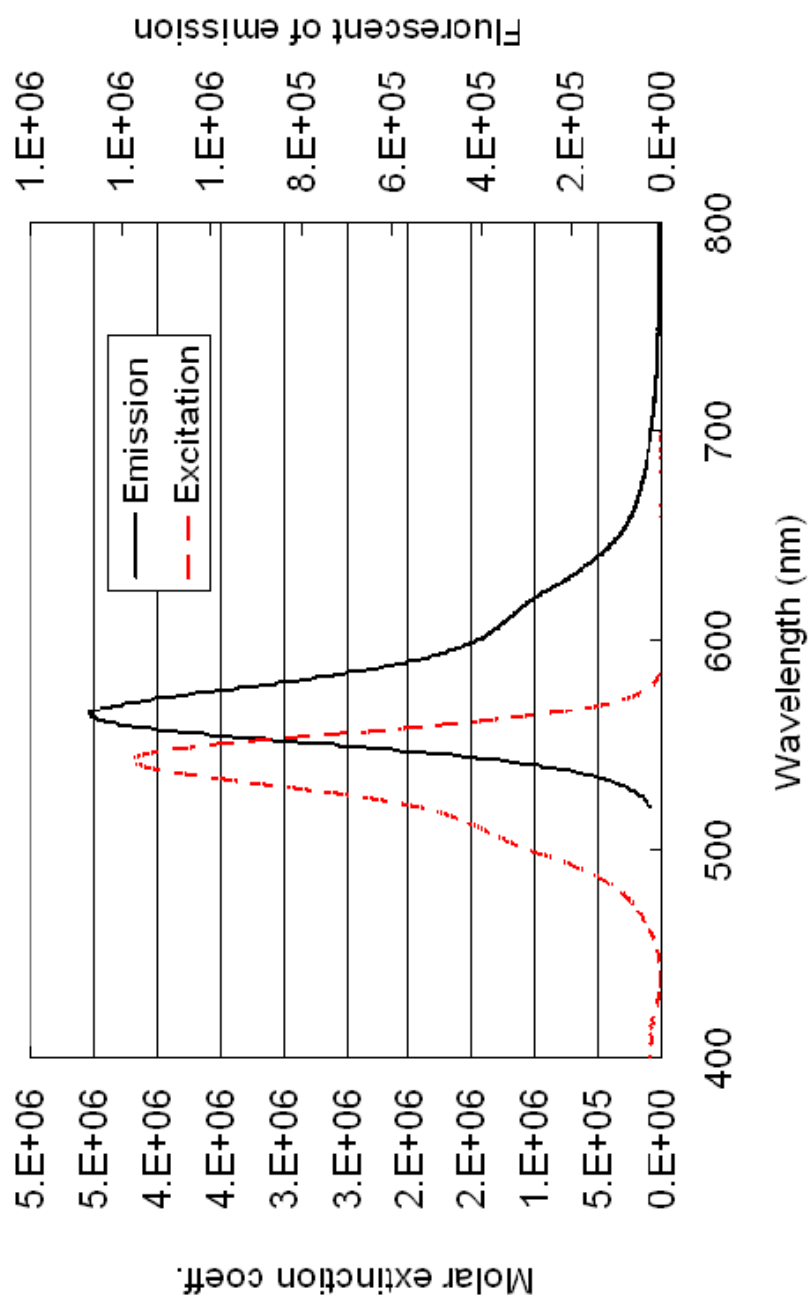


Figure A2. Wave length spectra of Rhodamine B
(used original data from <http://omlc.org/spectra/PhotochemCAD/html/rhodamineB.html>)

APPENDIX B
TWO-PHASE FLOW REGIME MAP

B.1 Flow Chart for Two-Phase Gas-Liquid Flow Map

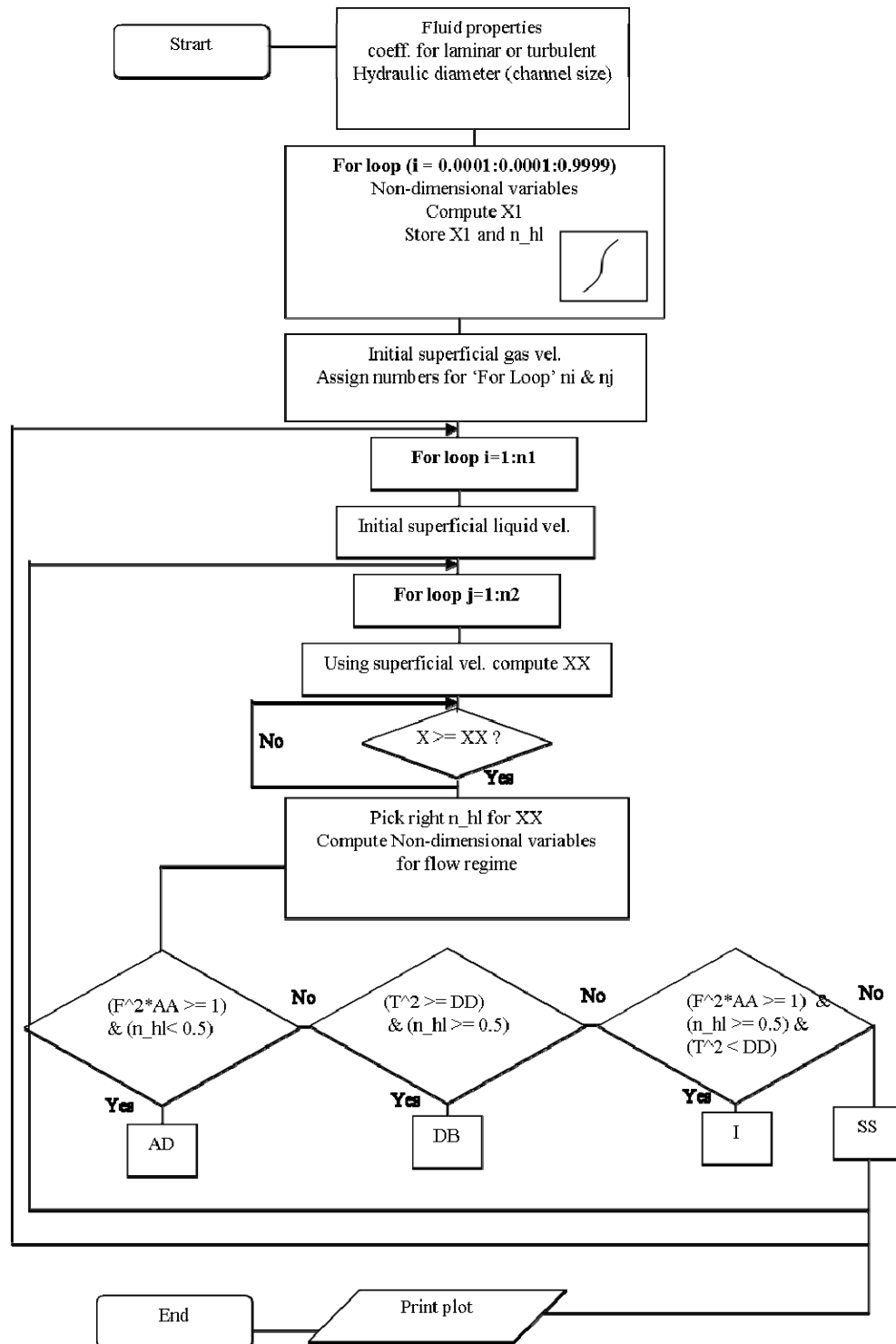


Figure A3. Flow chart for two-phase flow map

B.2 MATLAB Code for Flow Regime Map

```

%*****
% This program is for generating two-phase flow regime map
% proposed by Taitel and Dukler (1976)
% Turbulent coefficients are used for gas and liquid flows for fractal-like branching channel network
% Written by Younghoon Kwak
% Date: September, 2007
%*****

clear;
close all;
clc;
%*****fluid property*****
%water & air @25 degree C
nu_l=1.004e-6;% m^2/s %water
nu_g=1.560e-5;% m^2/s %air
rho_l=997.13;%kg/m^3 water
rho_g=1.168;%kg/m^3 air

%-----Coeff. set-----
% Liquid turbulent
C_l=0.042; n=0.2;
% Gas turbulent
C_g=0.042; m=0.2;

%----- hydraulic diameter, acceleration of gravity----
D = 308/(10^6); %hydraulic diameter (m)
g = 9.8; %(m/s^2)

%----- X vs. hl/Dh Taitel & Duckler -----
count=0;

for i=0.0001:0.0001:0.9999
    count=count+1;
    n_hl=i;
    n_Al=0.25*(pi-acos(2*n_hl-1)+(2*n_hl-1)*sqrt(1-(2*n_hl-1)^2));
    n_Ag=0.25*(acos(2*n_hl-1)-(2*n_hl-1)*sqrt(1-(2*n_hl-1)^2));
    n_sl=pi-acos(2*n_hl-1);
    n_sg=acos(2*n_hl-1);
    n_si=sqrt(1-(2*n_hl-1)^2);
    n_A=n_Al+n_Ag;
    n_ul=n_A/n_Al; n_ug=n_A/n_Ag;
    n_Dl=4*n_Al/n_sl; n_Dg=4*n_Ag/(n_sg+n_si);

    num=((n_ug*n_Dg)^(-m) * n_ug^2 * (n_sg/n_Ag+n_si/n_Al+n_si/n_Ag));
    denom=((n_ul*n_Dl)^(-n) * n_ul^2 * (n_sl/n_Al));

    Xl(count)=sqrt(num/denom);
    n_hl_d(count)=i;
end
%-----

u_gs=1e-2; %initial superficial gas velocity

```

```

n1=-2;% initial power of gas velocity

ni=17;%number of for-loop (superficial gas vel.)
nj=17;%number of for-loop (superficial liquid vel.)

for i=1:ni
    u_gs=u_gs+10^n1;%superficial gas velocity

    u_ls=1e-3;%initial superficial liquid velocity
    n2=-3;% initial power of liquid velocity

    for j=1:nj
        u_ls=u_ls+10^n2;%superficial liquid velocity

        % Store superficial gas and liquid velocity in ugs and uls
        ugs(j,i)=u_gs;
        uls(j,i)=u_ls;

        % Define X using dimensional values
        num_XX=4*C_l/D * (u_ls*D/nu_l)^-n * (rho_l*u_ls^2)/2;
        denum_XX=4*C_g/D * (u_gs*D/nu_g)^-m * (rho_g*u_gs^2)/2;
        XX=sqrt(num_XX/denum_XX);

        %searching for X1 array location equals to XX
        for h=1:count
            if X1(h) >= XX
                break;
            end
        end

        n_hl=n_hl_d(h); % Find dimensionless water level

        % using new dimensionless water level
        n_Al=0.25*(pi-acos(2*n_hl-1)+(2*n_hl-1)*sqrt(1-(2*n_hl-1)^2));
        n_Ag=0.25*(acos(2*n_hl-1)-(2*n_hl-1)*sqrt(1-(2*n_hl-1)^2));
        n_sl=pi-acos(2*n_hl-1);
        n_sg=acos(2*n_hl-1);
        n_si=sqrt(1-(2*n_hl-1)^2);
        n_A=n_Al+n_Ag;
        n_ul=n_A/n_Al; n_ug=n_A/n_Ag;
        n_Dl=4*n_Al/n_sl; n_Dg=4*n_Ag/(n_sg+n_si);

        %curve A
        diff=sqrt(1-(2*n_hl-1)^2);
        C2=1-n_hl;
        AA=(n_ug*diff/n_Ag/C2^2);
        F=sqrt(rho_g/(rho_l-rho_g))/sqrt(D*g)*u_gs;

        %curve D
        DD= 8*n_Ag / n_si / n_ul^2 / (n_ul*n_Dl)^-n ;
        num_T=(4*C_l/D) * (u_ls*D/nu_l)^(-n) * (rho_l*u_ls^2/2);
        denum_T=(rho_l-rho_g)*g;
        T=sqrt(num_T / denum_T);
    end
end

```

```

%-----Flow regime criteria -----
% AD (Annular Dispersed Flow)
if (F^2*AA >= 1) & (n_hl < 0.5)
    map(j,i)=2;% AD light blue

% DB (Dispersed Bubble or Bubbly Flow)
elseif (T^2 >= DD) & (n_hl >= 0.5)
    map(j,i)=3;% DB or bubbly flow yellow

% I (Intermittent)
elseif (F^2*AA >= 1) & (n_hl >= 0.5) & (T^2 < DD)%origin
    map(j,i)=1;%intermittent

% SS (Stratified Smooth)
else
    map(j,i)=4;% ss
end
%-----
n2=n2+0.2; %increament for superficial liquid vel
end

n1=n1+0.2; % increament for superfical gas vel
end

% ----- Flow map plot -----
count1=0; count2=0; count3=0; count4=0;
for i=1:ni
    for j=1:nj
        count1=count1+1;
        count2=count2+1;
        count3=count3+1;
        count4=count4+1;

        if map(j,i) == 1
            x1(count1)=ugs(j,i);
            y1(count1)=uls(j,i);
        elseif map(j,i) == 2
            x2(count2)=ugs(j,i);
            y2(count2)=uls(j,i);
        elseif map(j,i) == 3
            x3(count3)=ugs(j,i);
            y3(count3)=uls(j,i);
        else
            x4(count4)=ugs(j,i);
            y4(count4)=uls(j,i);
        end
    end
end

figure;
axes('box','on','LineWidth',2);
set(gcf,'color','w','units','inches','position',[0 0 10 8]);

```

```

set(gcf,'PaperPosition',[0 0 25.4 20.32]);
H=loglog(x1,y1,'kx',x2,y2,'g+',x3,y3,'ro',x4,y4,'bs');
set(H,'LineWidth',2,'MarkerSize',10);
set(gca,'FontSize',18,'FontWeight','bold');
xlabel('Superficial gas velocity (m/s)');
ylabel('Superficial liquid velocity (m/s)');
legend('Intermittent', 'Annular & dispersed', 'Bubbly', 'Stratified'

```

APPENDIX C

IMAGE AND DATA ANALYSIS PROGRAMS

C.1 Bubble Centerline Velocity Measurement

```

%*****
% This program is for determining bubble leading edge centerline velocity
% Written by Younghoon Kwak
% Date: September 2007
%*****
close all;
clear all;
imnum=input('Enter the number of images.----> ');
initial=input('Enter the initial number----> ');
base_name=input('Enter the base name of the images(in apostrophes).--->');
%base_name_b=input('Enter the base name of the images(in apostrophes).--->');

for kk=initial:imnum+initial-1
    str=num2str(kk);

    callname_a=[base_name,str,'_a'];
    callname_b=[base_name,str,'_b'];

    name_a=[callname_a,'.tif'];
    name_b=[callname_b,'.tif'];
    pa=imread(name_a,'tif');
    pb=imread(name_b,'tif');

    %pa=imread('bfront0010_a','tif');
    %pb=imread('bfront0010_b','tif');

    pa_hist=histeq(pa,255);
    pb_hist=histeq(pb,255);
    cut_max=725;
    cut_min=392;
    c_line=round(cut_min+(cut_max-cut_min)/2);

    sz=size(pa); num=sz(2)-100;

    for k=1:num;
        xpix(k)=k;
    end

    M=10;
    N=10;
    pa = MEDFILT2(pa_hist,[M N],'zeros');
    pb = MEDFILT2(pb_hist,[M N],'zeros');

    for ii=1:cut_min
        for jj=1:1344
            pa(ii,jj)=0;
            pb(ii,jj)=0;
        end
    end

    for ii=cut_max:1024

```



```

        for jj=1:1344
            pa(ii,jj)=0;
            pb(ii,jj)=0;
        end
    end
    factor=2;
    search_a=pa(c_line,:);
    search_b=pb(c_line,:);
    %dum1=size(search);
    ma=max(search_a(80:400));

    for i=100:num
        if search_a(i) == ma
            location_a(kk)=i;
            j=i;
            break;
        end
    end
    mb=max(search_b(j:j+300));

    for i=100:num
        if search_b(i) == mb
            location_b(kk)=i;
            break;
        end
    end
    %end
    pix_resolution=1; %micron/pix
    time_interval=480;
    'File number',kk
    process_num(kk)=kk;

    bfront_distance(kk)=location_b(kk)-location_a(kk);
    bubble_f_d(kk)=bfront_distance(kk);
    V_bubble_front(kk)=bubble_f_d(kk)*pix_resolution/time_interval;% [m/s]

end
V_front_mean=mean(V_bubble_front)
V_front_mean1(1:kk)=V_front_mean;
stdev=std(V_bubble_front)

figure;
axes('box','on','LineWidth',factor);
    set(gca,'FontSize',8,'FontWeight','bold','color','w');
    set(gcf,'color','w','units','inches','position',[0 0 7 6]);
    set(gcf,'PaperPosition',[0 0 18 13.14]);

H=plot(process_num, V_bubble_front,'bo',process_num,V_front_mean1,'b-');
set(H,'LineWidth',2,'MarkerSize',12);set(gca,'FontSize',18,'FontWeight','bold');
xlabel('N')
ylabel('u (m/s)')
legend('u_L','Ave. u_L')

```

```

grid on
%AXIS([0 45 -0.1 0.1])

crit_num=input('Do you want to save data? yes=1 or no=0 ----> ');
if crit_num==1

%%%%%%%%%%%%%%OUTPUT %%%%%%%%%%%%%%%

filename=input('please type the filename for writting----->');
fileout=[filename,'.txt'];

fid=fopen(fileout,'w');
for kk=1:imnum

        fprintf(fid,'%8.1f          %9.7f          \n',
bubble_f_d(kk),V_bubble_front(kk));

end
status=fclose(fid);

%%%%%%%%%%%%%%
else
end

```

C.2 Base Image Maker

```
%*****
% This program is to determining channel boundary and generating base images
% for each case and  $k_{th}$  branching level
% written by Douglas Heymann
% Date: Apr, 2008
%*****

clear; clc; close all
b=imread('case12_ch0_1.tif',10);figure;imshow(b);
write_name='Current_BW_Base_case12_ch0.tif';
A=histsq(b);figure;imshow(A);
A=wiener2(A,[5 5]);figure;imshow(A);
A=imcomplement(A);figure;imshow(A);
A=imfill(A);figure;imshow(A);
A2=im2bw(A,.63);
A2=medfilt2(A2,[5 5]);figure; imshow(A2);
Dec=input('Yes (type 1) or no (type 0)? ');
if Dec ==1
    imwrite(A2,write_name);
else
    break
end
```

C.3 Case Running Program

```
%*****
% Ave_in_out_curve.m
% This program is the main program for assigning case number and
% kth branching level
% written by Douglas Heymann
% modified by Younghoon Kwak
% Date: Apr, 2008
%*****

clear; clc; close all
ii=0;
%for i=[10]; % i represents the case
%    k_level=1;
%    ii=ii+1;
%    Void_Frac(ii)=Ave_in_out_curve(i,k_level);
%end
case_no=12;
for i=[0]; % i k level

    k_level=i;
    ii=ii+1;
    Void_Frac(ii)=Ave_in_out_curve1(case_no,k_level);
end
```

C.4 Function m-File for Void Fraction Measurement

```
% Ave_in_out_curve.m
% This program will determine void fraction by averaging the inner and
% outer edges of the bubbles to account for the bubble curvature
% written by Douglas Heymann
% modified by Younghoon Kwak
% Date: Apr, 2008
function VoidFrac=Ave_in_out_curve1(case_no,k_level);
switch k_level;
    case 0 % All data for k=0
        switch case_no
            case 2
                case_path='/Volumes/WDOUG/ONR/Cases 1-5/case2_ch0_1.tif';
                b=imread(case_path,2);
                rect=[132.510000000000,148.510000000000,642.980000000000,196.980000000000;];
                case2_base_path='/Volumes/WDOUG/ONR/Cases 1-
5/Current_BW_Base_case2_ch0.tif';
                bw=imread(case2_base_path);
                save_name=['Case_2_ch0_' datestr(now,30) '.mat'];
            case 4
                case_path='case4_ch0_1.tif';
                b=imread(case_path,1);
                case4_base_path='Current_BW_Base_case4_ch0.tif';
                rect=[151.510000000000,166.510000000000,638.980000000000,200.980000000000;];
                bw=imread(case4_base_path);
                save_name=['Case_4_ch0_' datestr(now,30) '.mat'];
            case 5
                case_path='/Volumes/WDOUG/ONR/Cases 1-5/case5_ch0_1.tif';
                b=imread(case_path,1);
                case5_base_path='/Volumes/WDOUG/ONR/Cases 1-
5/Current_BW_Base_case5_ch0.tif';
                rect=[146.510000000000,146.510000000000,634.980000000000,199.980000000000;];
                bw=imread(case5_base_path);
                save_name=['Case_5_ch0_' datestr(now,30) '.mat'];
            case 6
                case_path='/Volumes/WDOUG/ONR/Cases 1-5/case6_ch0_1.tif';
                b=imread(case_path,213);
                case6_base_path='/Volumes/WDOUG/ONR/Cases 1-
5/Current_BW_Base_case6_ch0.tif';
                rect=[128.510000000000,158.510000000000,649.980000000000,191.980000000000;];
                bw=imread(case6_base_path);
                save_name=['Case_6_ch0_' datestr(now,30) '.mat'];
            case 7
                case_path='/Volumes/WDOUG/ONR/Cases 7-12/case7_ch0_1.tif';
                b=imread(case_path,1);
                case7_base_path='/Volumes/WDOUG/ONR/Cases 7-
12/Current_BW_Base_case7_ch0.tif';
                rect=[150.510000000000,148.510000000000,632.980000000000,213.980000000000;];
                bw=imread(case7_base_path);
                save_name=['Case_7_ch0_' datestr(now,30) '.mat'];
            case 8
                case_path='/Volumes/WDOUG/ONR/Cases 7-12/case8_ch0_1.tif';
```

```

        b=imread(case_path,2030);
        case8_base_path='/Volumes/WDOUG/ONR/Cases 7-
12/Current_BW_Base_case8_ch0.tif';
        rect=[147.510000000000,150.510000000000,631.980000000000,209.980000000000;];
        bw=imread(case8_base_path);
        save_name=['Case_8_ch0_' datestr(now,30) '.mat'];
    case 9
        case_path='/Volumes/WDOUG/ONR/Cases 7-12/case9_ch0_1.tif';
        b=imread(case_path,11);
        case9_base_path='/Volumes/WDOUG/ONR/Cases 7-
12/Current_BW_Base_case9_ch0.tif';
        rect=[154.510000000000,146.510000000000,636.980000000000,206.980000000000;];
        bw=imread(case9_base_path);
        save_name=['Case_9_ch0_' datestr(now,30) '.mat'];
    case 10
        case_path='/Volumes/WDOUG/ONR/Cases 7-12/case10_ch0_1.tif';
        rect=[161.510000000000,148.510000000000,623.980000000000,202.980000000000;];
        b=imread(case_path,22);
        case10_base_path='/Volumes/WDOUG/ONR/Cases 7-
12/Current_BW_Base_case10_ch0.tif';
        bw=imread(case10_base_path);
        save_name=['Case_10_ch0_' datestr(now,30) '.mat'];
    case 11
        case_path='/Volumes/WDOUG/ONR/Cases 7-12/case11_ch0_1.tif';
        rect=[147.510000000000,145.510000000000,626.980000000000,208.980000000000;];
        b=imread(case_path,1002);
        case11_base_path='/Volumes/WDOUG/ONR/Cases 7-
12/Current_BW_Base_case11_ch0.tif';
        bw=imread(case11_base_path);
        save_name=['Case_11_ch0_' datestr(now,30) '.mat'];
    case 12
        case_path='case12_ch0_1.tif';
        rect=[1,1,1024,512;];
        %rect=[155.510000000000,168.510000000000,628.980000000000,205.980000000000;]
;

        b=imread(case_path,10);
        case12_base_path='Current_BW_Base_case12_ch0.tif';
        bw=imread(case12_base_path);
        save_name=['Case_12_ch0_' datestr(now,30) '.mat'];

    end % Ending the k=0 case switch
%-----
case 1 % All data for k=1
switch case_no
    case 1
        case_path='case1_ch1_1.tif';
        rect=[1,1,1024,512;];
        b=imread(case_path,2);
        case1_base_path='Current_BW_Base_case1_ch1.tif';
        bw=imread(case1_base_path);
        save_name=['Case_1_ch1_' datestr(now,30) '.mat'];
    case 2

```

```

case_path='case2_ch1_1.tif';
rect=[1,1,1024,512;];
b=imread(case_path,1);
case2_base_path='Current_BW_Base_case2_ch1.tif';
bw=imread(case2_base_path);
save_name=['Case_2_ch1_' datestr(now,30) '.mat'];
case 3
case_path='case3_ch1_1.tif';
rect=[1,1,1024,512;];
b=imread(case_path,1);
case3_base_path='Current_BW_Base_case3_ch1.tif';
bw=imread(case3_base_path);
save_name=['Case_3_ch1_' datestr(now,30) '.mat'];
case 4
case_path='case4_ch1_1.tif';
rect=[240.510000000000,0.510000000000000,555.980000000000,511.980000000000;];
b=imread(case_path,4);
case4_base_path='Current_BW_Base_case4_ch1.tif';
bw=imread(case4_base_path);
save_name=['Case_4_ch1_' datestr(now,30) '.mat'];
case 5
case_path='case5_ch1_1.tif';
rect=[238.510000000000,1.51000000000000,554.980000000000,510.980000000000;];
b=imread(case_path,1);
case5_base_path='Current_BW_Base_case5_ch1.tif';
bw=imread(case5_base_path);
save_name=['Case_5_ch1_' datestr(now,30) '.mat'];
case 6
case_path='case6_ch1_1.tif';
rect=[1,1,1024,512;];
b=imread(case_path,1);
case6_base_path='Current_BW_Base_case6_ch1.tif';
bw=imread(case6_base_path);
save_name=['Case_6_ch1_' datestr(now,30) '.mat'];
case 7
case_path='case7_ch1_1.tif';
rect=[241.510000000000,1.51000000000000,550.980000000000,510.980000000000;];
b=imread(case_path,2);
case7_base_path='Current_BW_Base_case7_ch1.tif';
bw=imread(case7_base_path);
save_name=['Case_7_ch1_' datestr(now,30) '.mat'];
case 8
case_path='case8_ch1_1.tif';
rect=[245.510000000000,1.51000000000000,541.980000000000,510.980000000000;];
b=imread(case_path,6);
case8_base_path='Current_BW_Base_case8_ch1.tif';
bw=imread(case8_base_path);
save_name=['Case_8_ch1_' datestr(now,30) '.mat'];
case 9
case_path='case9_ch1_2.tif';
rect=[240.510000000000,0.510000000000000,548.980000000000,511.980000000000;];
b=imread(case_path,27);
case9_base_path='Current_BW_Base_case9_ch1.tif';

```

```

        bw=imread(case9_base_path);
        save_name=['Case_9_ch1_' datestr(now,30) '.mat'];
case 10%-----
    case_path='case10_ch1_2.tif';
    rect=[1,1,1024,512;];
    b=imread('case10_ch1_1.tif',263);
    case10_base_path='Current_BW_Base_case10_ch1.tif';
    bw=imread(case10_base_path);
    save_name=['Case_10_ch1_2' datestr(now,30) '.mat'];
case 11
    case_path='case11_ch1_1.tif';
    rect=[241.510000000000,2.51000000000000,549.980000000000,508.980000000000;];
    b=imread(case_path,40);
    case11_base_path='Current_BW_Base_case11_ch1.tif';
    bw=imread(case11_base_path);
    save_name=['Case_11_ch1_' datestr(now,30) '.mat'];
case 12
    case_path='case12_ch1_1.tif';
    rect=[242.510000000000,0.51000000000000,539.980000000000,510.980000000000;];
    b=imread(case_path,2);
    case12_base_path='Current_BW_Base_case12_ch1.tif';
    bw=imread(case12_base_path);
    save_name=['Case_12_ch1_' datestr(now,30) '.mat'];
end % Ending the k=1 case switch

case 2 % k=2 level
    switch case_no% %This switches between cases for the k=2 level
        case 1
            case_path='case1_ch2_1.tif';
            rect=[1,1,1024,512;];
            b=imread(case_path,1);
            case1_base_path='Current_BW_Base_case1_ch2.tif';
            bw=imread(case1_base_path);
            save_name=['Case_1_ch2_' datestr(now,30) '.mat'];
        case 2
            case_path='case2_ch2_1.tif';
            rect=[1,1,1024,512;];
            b=imread(case_path,1);
            case2_base_path='Current_BW_Base_case2_ch2.tif';
            bw=imread(case2_base_path);
            save_name=['Case_2_ch2_' datestr(now,30) '.mat'];
        case 3
            case_path='case3_ch2_1.tif';
            rect=[1,1,1024,512;];
            b=imread(case_path,1);
            case3_base_path='Current_BW_Base_case3_ch2.tif';
            bw=imread(case3_base_path);
            save_name=['Case_3_ch2_' datestr(now,30) '.mat'];
        case 4
            case_path='case4_ch2_1.tif';
            rect=[1,1,1024,512;];
            b=imread(case_path,1);
            case4_base_path='Current_BW_Base_case4_ch2.tif';

```

```

bw=imread(case4_base_path);
save_name=['Case_4_ch2_' datestr(now,30) '.mat'];
case 5
case_path='case5_ch2_1.tif';
rect=[1,1,1024,512;];
b=imread(case_path,1);
case5_base_path='Current_BW_Base_case5_ch2.tif';
bw=imread(case5_base_path);
save_name=['Case_5_ch2_' datestr(now,30) '.mat'];
case 6
case_path='case6_ch2_1.tif';
rect=[1,1,1024,512;];
b=imread(case_path,1);
case6_base_path='Current_BW_Base_case1_ch2.tif';
bw=imread(case6_base_path);
save_name=['Case_6_ch2_' datestr(now,30) '.mat'];
case 7
case_path='case7_ch2_1.tif';
rect=[1,1,1024,512;];
b=imread(case_path,1);
case7_base_path='Current_BW_Base_case1_ch2.tif';
bw=imread(case7_base_path);
save_name=['Case_7_ch2_' datestr(now,30) '.mat'];
case 8
case_path='case8_ch2_1.tif';
rect=[1,1,1024,512;];
b=imread(case_path,2);
case8_base_path='Current_BW_Base_case8_ch2.tif';
bw=imread(case8_base_path);
save_name=['Case_8_ch2_' datestr(now,30) '.mat'];
case 9
case_path='case9_ch2_1.tif';
rect=[1,1,1024,512;];
b=imread(case_path,243);
case9_base_path='Current_BW_Base_case9_ch2.tif';
bw=imread(case9_base_path);
save_name=['Case_9_ch2_' datestr(now,30) '.mat'];
case 10%-----
case_path='case10_ch2_2.tif';
rect=[1,1,1024,512;];
b=imread('case10_ch2_1.tif',1407);
case10_base_path='Current_BW_Base_case10_ch2.tif';
bw=imread(case10_base_path);
save_name=['Case_10_ch2_2' datestr(now,30) '.mat'];
case 11
case_path='case11_ch2_1.tif';
rect=[1,1,1024,512;];
b=imread(case_path,1222);
case11_base_path='Current_BW_Base_case11_ch2.tif';
bw=imread(case11_base_path);
save_name=['Case_11_ch2_' datestr(now,30) '.mat'];
case 12
case_path='case12_ch2_1.tif';

```



```

rect=[1,1,1024,512;];
b=imread(case_path,21);
case12_base_path='Current_BW_Base_case12_ch2.tif';
bw=imread(case12_base_path);
save_name=['Case_12_ch2_' datestr(now,30) '.mat'];
end
case 3 % k=3 level
switch case_no% This switches between cases for the k=3 level
case 1
case_path='case1_ch3_1.tif';
rect=[1,1,1024,512;];
b=imread(case_path,1);
case1_base_path='Current_BW_Base_case1_ch3.tif';
bw=imread(case1_base_path);
save_name=['Case_1_ch3_' datestr(now,30) '.mat'];
case 2
case_path='case2_ch3_1.tif';
rect=[1,1,1024,512;];
b=imread(case_path,1);
case2_base_path='Current_BW_Base_case2_ch3.tif';
bw=imread(case2_base_path);
save_name=['Case_2_ch3_' datestr(now,30) '.mat'];
case 3
case_path='case3_ch3_1.tif';
rect=[1,1,1024,512;];
b=imread(case_path,1);
case3_base_path='Current_BW_Base_case3_ch3.tif';
bw=imread(case3_base_path);
save_name=['Case_3_ch3_' datestr(now,30) '.mat'];
case 4
case_path='case4_ch3_1.tif';
rect=[1,1,1024,512;];
b=imread(case_path,3);
case4_base_path='Current_BW_Base_case4_ch3.tif';
bw=imread(case4_base_path);
save_name=['Case_4_ch3_' datestr(now,30) '.mat'];
case 5
case_path='case5_ch3_1.tif';
rect=[1,1,1024,512;];
b=imread(case_path,1);
case5_base_path='Current_BW_Base_case5_ch3.tif';
bw=imread(case5_base_path);
save_name=['Case_5_ch3_' datestr(now,30) '.mat'];
case 6
case_path='case6_ch3_1.tif';
rect=[1,1,1024,512;];
b=imread(case_path,1);
case6_base_path='Current_BW_Base_case1_ch3.tif';
bw=imread(case6_base_path);
save_name=['Case_6_ch3_' datestr(now,30) '.mat'];
case 7
case_path='case7_ch3_1.tif';
rect=[1,1,1024,512;];

```

```

b=imread(case_path,1);
case7_base_path='Current_BW_Base_case1_ch3.tif';
bw=imread(case7_base_path);
save_name=['Case_7_ch3_' datestr(now,30) '.mat'];
case 8
case_path='case8_ch3_1.tif';
rect=[1,1,1024,512;];
b=imread(case_path,2);
case8_base_path='Current_BW_Base_case8_ch3.tif';
bw=imread(case8_base_path);
save_name=['Case_8_ch3_' datestr(now,30) '.mat'];
case 9
case_path='case9_ch3_1.tif';
rect=[1,1,1024,512;];
b=imread(case_path,206);
case9_base_path='Current_BW_Base_case9_ch3.tif';
bw=imread(case9_base_path);
save_name=['Case_9_ch3_' datestr(now,30) '.mat'];
case 10%-----
case_path='case10_ch3_2.tif';
rect=[1,1,1024,512;];
b=imread('case10_ch3_1.tif',1012);
case10_base_path='Current_BW_Base_case10_ch3.tif';
bw=imread(case10_base_path);
save_name=['Case_10_ch3_2' datestr(now,30) '.mat'];
case 11
case_path='case11_ch3_2.tif';
rect=[1,1,1024,512;];
b=imread(case_path,310);
case11_base_path='Current_BW_Base_case11_ch3.tif';
bw=imread(case11_base_path);
save_name=['Case_11_ch3_2' datestr(now,30) '.mat'];
case 12
case_path='case12_ch3_1.tif';
rect=[1,1,1024,512;];
b=imread(case_path,10);
case12_base_path='Current_BW_Base_case12_ch3.tif';
bw=imread(case12_base_path);
save_name=['Case_12_ch3_' datestr(now,30) '.mat'];
end
case 4 % k = 4 level
switch case_no % This switches between cases for the k=4 level
case 1
case_path='case1_ch4_1.tif';
rect=[1,1,1024,256;];
b=imread(case_path,1);
case1_base_path='Current_BW_Base_case1_ch4.tif';
bw=imread(case1_base_path);
save_name=['Case_1_ch4_' datestr(now,30) '.mat'];
case 2
case_path='case2_ch4_1.tif';
rect=[1,1,1024,256;];
b=imread(case_path,1);

```

```

case2_base_path='Current_BW_Base_case2_ch4.tif';
bw=imread(case2_base_path);
save_name=['Case_2_ch4_' datestr(now,30) '.mat'];
case 3
case_path='case3_ch4_1.tif';
rect=[1,1,1024,256;];
b=imread(case_path,2);
case3_base_path='Current_BW_Base_case3_ch4.tif';
bw=imread(case3_base_path);
save_name=['Case_3_ch4_' datestr(now,30) '.mat'];
case 4
case_path='case4_ch4_1.tif';
rect=[1,1,1024,256;];
b=imread(case_path,1);
case4_base_path='Current_BW_Base_case4_ch4.tif';
bw=imread(case4_base_path);
save_name=['Case_4_ch4_' datestr(now,30) '.mat'];
case 5
case_path='case5_ch4_1.tif';
rect=[1,1,1024,256;];
b=imread(case_path,2);
case5_base_path='Current_BW_Base_case5_ch4.tif';
bw=imread(case5_base_path);
save_name=['Case_5_ch4_' datestr(now,30) '.mat'];
case 6
case_path='case6_ch4_1.tif';
rect=[1,1,1024,256;];
b=imread(case_path,1);
case6_base_path='Current_BW_Base_case6_ch4.tif';
bw=imread(case6_base_path);
save_name=['Case_6_ch4_' datestr(now,30) '.mat'];
case 7
case_path='case7_ch4_1.tif';
rect=[1,1,1024,256;];
b=imread(case_path,2);
case7_base_path='Current_BW_Base_case7_ch4.tif';
bw=imread(case7_base_path);
save_name=['Case_7_ch4_' datestr(now,30) '.mat'];
case 8
case_path='case8_ch4_1.tif';
rect=[1,1,1024,256;];
b=imread(case_path,2);
case8_base_path='Current_BW_Base_case8_ch4.tif';
bw=imread(case8_base_path);
save_name=['Case_8_ch4_' datestr(now,30) '.mat'];
case 9
case_path='case9_ch4_1.tif';
rect=[1,1,1024,256;];
b=imread(case_path,47);
case9_base_path='Current_BW_Base_case9_ch4.tif';
bw=imread(case9_base_path);
save_name=['Case_9_ch4_' datestr(now,30) '.mat'];
case 10 %------

```

```

        case_path='case10_ch4_2.tif';
        rect=[1,1,1024,256;];
        b=imread('case10_ch4_1.tif',217);
        case10_base_path='Current_BW_Base_case10_ch4.tif';
        bw=imread(case10_base_path);
        save_name=['Case_10_ch4_2' datestr(now,30) '.mat'];
    case 11
        case_path='case11_ch4_1.tif';
        rect=[1,1,1024,256;];
        b=imread(case_path,297);
        case11_base_path='Current_BW_Base_case11_ch4.tif';
        bw=imread(case11_base_path);
        save_name=['Case_11_ch4_' datestr(now,30) '.mat'];
    case 12
        case_path='case12_ch4_1.tif';
        rect=[1,1,1024,256;];
        b=imread(case_path,39);
        case12_base_path='Current_BW_Base_case12_ch4.tif';
        bw=imread(case12_base_path);
        save_name=['Case_12_ch4_' datestr(now,30) '.mat'];
    end

end % Ending the k level switch

tic % Begin Program

bw=imcomplement((bw(:, :, 1))); bw=im2uint8(bw);
for image_index=1:4076%2038 % [258,487,582,853,925,1038,1056,1423,1744,1979,2002,2031;]%
    clear bord area area2 L_a2_index
    disp(['Image ' num2str(image_index) ' of case no. ' num2str(case_no)]);
    a=imread(case_path,image_index );figure; imshow(a);%*****
    %original_im=a;
    figure; imshow(b);%*****
    wn=15;          figure; imshow(a);%*****
    a=imabsdiff(a,b);figure; imshow(a);%*****

    a=imcrop(a,rect);

    a=imadjust(a,[0 1],[0 1],.5);
    a=wiener2(a, [wn wn]);figure; imshow(a);%*****
    %a0=a;
    a2=a;
    a=im2bw(a, 170);figure; imshow(a);%*****
    if sum(a(:))~=0
        a=wiener2(a, [wn wn]-10);
    end
    a2=imclose(a2,strel('disk',10));figure; imshow(a2); %*****
    a2=imfill(a2,'holes');figure; imshow(a2); %*****
    a2=wiener2(a2,[wn wn]);figure; imshow(a2); %*****
    a2=im2bw(a2,.1);figure; imshow(a2); %*****
    a=im2uint8(a);figure; imshow(a); %*****

```

```

a2=im2uint8(a2); figure;imshow(a2); %*****
a=imsubtract((a),bw);figure; imshow(a); %*****
a2=imsubtract((a2),bw);figure; imshow(a2); %*****
a=im2bw(a); figure; imshow(a); %*****
a2=im2bw(a2);figure; imshow(a2); %*****
a2=[zeros(size(a2,1),1) a2 zeros(size(a2,1),1)];
a=[zeros(size(a,1),1) a zeros(size(a,1),1)];

VF(image_index)=(sum(a2(:))-1/2*sum(a(:)))/(1/255*sum(imcomplement(bw(:))));
    % For each "body" found in a2, subtract 1/2 of the edge defined inside the
    % the body to get a rough estimate contribution of the bubble curvature to
    % the total void fraction
end
time_run=toc
VoidFrac=mean(VF);
save(save_name)

```

C.5 Liquid Vector Field at Bifurcation Section

```

%*****
% This program is to generate figures for 2D vector fields and 3D contours at
% bifurcation section between k=0 and k=1.
% written by Younghoon Kwak
% April, 2008
%*****
clear all
close all
n=input('enter name -----> ');
numy=83;
filein=[n,'.txt'];
p=load (filein,'txt');

initialy=p(1,2);
picsize=size(p);
totalnum=picsize(1,1);
numx=totalnum/numy;
sc=1;
count=0;

for i=1:numx
    for j=1:numy
        count=count+1;
        x(j,i)=p(count,3)*1000*sc;
        y(j,i)=p(count,4)*1000*sc;

        u(j,i)=p(count,5)*sc;
        v(j,i)=p(count,6)*sc;

        v_mag(j,i)=p(count,7)*sc;
    end
end

```

```
factor=1;
figure; %2d quiver plot
axes('box','on','LineWidth',factor);
    set(gca,'FontSize',8,'FontWeight','bold','color','w');
    set(gcf,'color','w','units','inches','position',[0 0 7 5.5]);
    set(gcf,'PaperPosition',[0 0 17.8 14]);
```

```
H=quiver(x,y,u,v,0.9,'k-');
set(H,'LineWidth',1);
set(gca,'FontSize',18,'FontWeight','bold');
```

```
AXIS([0 1300 50 990])%<<<<<<<<<<<
PBASPECT([1.32 1 1])
```

```
xlabel('x (\mu m)');
ylabel('y (\mu m)');
```

```
figure; %color surf 3-d plot
axes('box','on','LineWidth',factor);
set(gca,'FontSize',8,'FontWeight','bold','color','w');
set(gcf,'color','w','units','inches','position',[0 0 7 5.5]);
set(gcf,'PaperPosition',[0 0 17.8 14]);
```

```
H=surf(x,y,v_mag);
shading interp;
colorbar('vert');
set(H,'LineWidth',1);
set(gca,'FontSize',18,'FontWeight','bold');
```

```
AXIS([0 1300 50 990])%<<<<<<<<<<<<<<<
PBASPECT([1.32 1 1])
xlabel('x (\mum)');
ylabel('y (\mum)');
```

C.6 Velocity Profile and Comparison with Analytical Solution

[illegible]

```

count=0; Vmag=0; Vsum=0; Usum=0;

for j=1:numy
    for i=xmin:xmax
        if u(j,i) > 0
            count=count+1;
            Usum=u(j,i)+Usum;
            Vsum=v(j,i)+Vsum;
            Vmag=v_mag(j,i)+Vmag;
        else
            end
        end
        umax(:,i)=max(u(:,i));
    end
    Ave_U=Usum/count;
    Ave_V=Vsum/count;
    Ave_Vmag=Vmag/count;

    %Analytical solution (Shah and London) for each channel
    depth=250; width=440; % atk=0
    b=depth/2; a=width/2;
    z=0;
    aspec=b/a;
    m=1.7+0.5*(aspec^-1.4);

    if aspec <= 1/3
        n=2;
    else
        n=2+0.3*(aspec-1/3);
    end
    y_var=-a:2:a];
    dum=size(y_var);
    for j=1:dum(2)
        non_u(j)=(1-(z/b)^n)*(1-(abs(y_var(j)/a))^m);
        non_y(j)=y_var(j)/a;
    end
    %
    county=0;
    for j=1:numy
        county=county+1;
        countx=0;
        for i=xmin:xmax
            if u(j,i) > 0
                countx=countx+1;
                u_sel(county,countx)=u(j,i);
                y_sel(county,countx)=y(j,i);
                countxx=countx;

            else
                county=0;
            end
        end
    end
end

```



```

end

[maxu_sel, loc1]=max(u_sel);% find the max. vels. and its locations
[mmax,loc2]=max(maxu_sel);% find the location of y for the max. vel
loc3=loc1(loc2)+1; %max_location adjustment using addition or subtraction

for ii=1:countxx
    non_u_sel(:,ii)=u_sel(:,ii)/mmax;%maxu_sel(ii);

    non_y_sel(:,ii)=(y_sel(:,ii)-y_sel(loc3))/(width/2);
end

%-----
figure(2);
plot(non_u,non_y,'b-')
%-----
figure(3);
plot(u_sel,y_sel,'o')
%-----
figure(4);
axes('box','on','LineWidth',2);
H=plot(non_u_sel,non_y_sel,'o');
set(H,'LineWidth',2,'MarkerSize',12);
set(gca,'FontSize',16,'FontWeight','bold');
hold on
H=plot(non_u,non_y,'b-');
set(H,'LineWidth',2,'MarkerSize',12);
set(gca,'FontSize',16,'FontWeight','bold');
xlabel('u');
ylabel('y');
%-----
figure(5);% averaged & stdev
axes('box','on','LineWidth',2);
set(gcf,'color','w','units','inches','position',[0 0 6 5]);
set(gcf,'PaperPosition',[0 0 15.24 12.70]);
sz=size(non_u_sel);

for i=1:sz(1)
    ave_non_u_sel(i) = mean(non_u_sel(i,:));
    std_non_u_sel(i) = std(non_u_sel(i,:));
end

H=plot(ave_non_u_sel,non_y_sel(:,1),'ro');
set(H,'LineWidth',2,'MarkerSize',12);
set(gca,'FontSize',16,'FontWeight','bold');
hold on
H=plot(non_u,non_y,'b--');
set(H,'LineWidth',2,'MarkerSize',12);
set(gca,'FontSize',16,'FontWeight','bold');
xlabel('u');
ylabel('y');
grid on

```

```
axis([0 1.2 -1 1])
```

```
figure(6);
axes('box','on','LineWidth',2);
set(gcf,'color','w','units','inches','position',[0 0 6 5]);
set(gcf,'PaperPosition',[0 0 15.24 12.70]);
H=plot(u_sel(:,1),y_sel(:,1),'bs',u_sel(:,20),y_sel(:,20),'m<',u_sel(:,40),y_sel(:,40),'gd',u_sel(:,60),y_sel(
:,:60),'r*',u_sel(:,70),y_sel(:,70),'ko',u_sel(:,80),y_sel(:,80),'y^');
set(H,'LineWidth',2,'MarkerSize',12);
set(gca,'FontSize',16,'FontWeight','bold');
xlabel('u (m/s)');
ylabel('y (\mum)');
legend('x=16 \mum','x=326 \mum', 'x=652 \mum', 'x=978 \mum', 'x=1141 \mum','x=1304 \mum')
grid on
```

APPENDIX D

UNCERTAINTY ANALYSIS

This appendix presents uncertainty analysis for homogeneous void fraction and void fraction based on slip ratio.

D.1 Uncertainty of Homogeneous Void Fraction

The homogeneous void fraction was discussed in both Chapter 4 and Chapter 6. The homogeneous void fraction is defined as the ratio between gas and total volumetric flow rates. These volumetric flow rates for liquid and gas flows can be expressed by superficial velocities.

$$\beta = \frac{Q_g}{Q_g + Q_f} = \frac{j_g}{j_g + j_f} \quad (\text{D.1})$$

where Q and j are volumetric flow rate and superficial velocity, respectively. The subscripts of g and f present gas and liquid phases. Using Kline-McClintock relationship, the uncertainty of homogeneous void fraction is defined as

$$U_\beta = \sqrt{\left(\frac{\partial \beta}{\partial j_g} U_{j_g}\right)^2 + \left(\frac{\partial \beta}{\partial j_f} U_{j_f}\right)^2} \quad (\text{D.2})$$

where U_β , U_{j_g} and U_{j_f} are uncertainties of homogeneous void fraction, superficial gas velocity and superficial liquid velocity, respectively. The uncertainty of

homogeneous void fraction presented in Eq. D.2 is associated with uncertainties of superficial gas and liquid velocities. These gas and liquid superficial velocities are expressed by its mass flow rates over density and a cross-sectional area and also, presented in Eq. D.3.

$$j_g = \frac{\dot{m}_g}{\rho_g A} \quad \& \quad j_f = \frac{\dot{m}_f}{\rho_f A} \quad (\text{D.3})$$

Using Kline-McClintock relationship, the uncertainties of superficial velocities for gas and liquid phases are presented in Eq. D.4.

$$U_{j_g} = \sqrt{\left(\frac{\partial j_g}{\partial \dot{m}_g} U_{\dot{m}_g} \right)^2 + \left(\frac{\partial j_g}{\partial \rho_g} U_{\rho_g} \right)^2} \quad (\text{D.4})$$

$$U_{j_f} = \sqrt{\left(\frac{\partial j_f}{\partial \dot{m}_f} U_{\dot{m}_f} \right)^2 + \left(\frac{\partial j_f}{\partial \rho_f} U_{\rho_f} \right)^2}$$

Equation D.4 shows the uncertainties of gas and liquid velocities that are associated with uncertainties of mass flow rate and density. The uncertainty of cross-sectional channel area is not included in Eq. D.4, because the depth of channel is unable to be physically measured. The uncertainty of mass flow rate for liquid phase is determined by bias and precision errors from a mass flow meter and flow measurements, respectively. The uncertainty of water density is negligible because of use of incompressible flow at the room temperature of 25°C. However, the uncertainty of air mass flow rate is associated with other uncertainties from measurements. The air mass flow rate is defined as

$$\dot{m}_g = \rho_{gas\ inject,g} Q_{gas\ inject,g} = \frac{P_{gas\ inject,g}}{RT_{gas\ inject,g}} Q_{gas\ inject,g} \quad (D.5)$$

where \dot{m}_g , $\rho_{gas\ inject,g}$, $P_{gas\ inject,g}$, $T_{gas\ inject,g}$ and R are mass flow rate, density, pressure, temperature and gas constant for air gas at the gas injector. Based on Eq. D.5, the uncertainty of air mass flow rate is determined using McClintock relationship.

$$U_{\dot{m}_g} = \sqrt{\left(\frac{\partial \dot{m}_g}{\partial P_{gas\ inject,g}} U_{P_{gas\ inject,g}} \right)^2 + \left(\frac{\partial \dot{m}_g}{\partial T_{gas\ inject,g}} U_{T_{gas\ inject,g}} \right)^2 + \left(\frac{\partial \dot{m}_g}{\partial Q_{gas\ inject,g}} U_{Q_{gas\ inject,g}} \right)^2} \quad (D.6)$$

By substituting uncertainties of pressure, temperature and volumetric flow rate for air gas at the gas injector, the uncertainty of air mass flow rates can be determined using Eq. D.6. Each pressure, temperature and volumetric flow rate uncertainty is also associated bias and precision errors. With a similar uncertainty analysis as shown in above, the uncertainty of local air density between the inlet of vacuum chuck and the exit can be determined as

$$U_{\rho_g} = \sqrt{\left(\frac{\partial \rho_g}{\partial P_g} U_{P_g} \right)^2 + \left(\frac{\partial \rho_g}{\partial T_g} U_{T_g} \right)^2} \quad (D.7)$$

where ρ_g , P_g , and T_g present air gas local density, pressure and temperature. The local pressure and temperature are expressed as average values of inlet and exit conditions. The uncertainties of local press and temperature are

$$U_{P_g} = \sqrt{\left(\frac{U_{P_{in}}}{2} \right)^2 + \left(\frac{U_{P_{atm}}}{2} \right)^2} \quad \& \quad U_{T_g} = \sqrt{\left(\frac{U_{T_{in}}}{2} \right)^2 + \left(\frac{U_{T_{atm}}}{2} \right)^2} \quad (D.8)$$

where P_{in} , T_{in} , P_{atm} and T_{atm} present inlet pressure, inlet temperature, exit pressure and exit temperature. The uncertainties of pressure and temperature at the inlet and exit of the test section obtain bias and precision errors from instruments and measurements. The bias and precision uncertainties determined directly by instruments and measurements are listed in Table D.1. Table D.2 presents other computed uncertainties of flow properties by submitting bias and precision errors from measurement at $k=0$ branching level. Finally, the uncertainties of homogeneous void fractions based on image and slip ratio are listed in Table D.3. The maximum and minimum relative uncertainties of homogeneous void fraction based on image are 11% and 1%, respectively. The higher relative uncertainties occur in lower homogeneous void fraction cases and lower relative uncertainties occur in higher homogeneous void fraction cases. The average homogeneous void fraction is approximately 5%.

Table D.1. Measured values and uncertainties from global measurements from (a) image based void fraction and (b) slip ratio base void fraction experiments

(a)

	mdot in (g/min)	U_mdot (g/min)	Pair (psi)	U_Pair (psi)	Tair (C)	U_Tair (C)	Tin(C) (C)	U_Tin (C)	Patm (kPa)	U_Patm (kPa)	Tatm (C)	U_Tatm (C)	Qair (ml/min)	U_Qair (ml/min)	Pin (kPa)	U_Pin (kPa)
case																
1	40.1	0.1	3.2	0.10	24	1.0	24.9	0.4	101.1	0.3	24.4	0.34	0.58	0.06	2.8904	0.35
2	20.1	0.1	3.2	0.10	25	1.0	26.0	0.4	101.0	0.3	25.3	0.30	0.57	0.06	1.8102	0.35
3	5.0	0.1	3.2	0.10	26	1.0	26.1	0.4	100.8	0.3	25.6	0.30	0.57	0.06	1.4228	0.35
4	5.1	0.1	4.2	0.10	26	1.0	26.3	0.4	100.6	0.3	25.8	0.30	1.06	0.08	1.3922	0.35
5	20.1	0.1	4.2	0.10	26	1.0	27.2	0.4	100.5	0.3	26.0	0.30	1.09	0.09	1.9904	0.35
6	40.1	0.1	4.2	0.10	26	1.0	26.5	0.4	100.3	0.3	24.7	0.30	1.09	0.09	2.5571	0.35
7	40.3	0.1	7.3	0.10	24	1.0	24.5	0.4	100.0	0.3	22.9	0.30	6.64	0.16	3.605	0.35
8	20.0	0.1	7.3	0.10	24	1.0	24.6	0.4	99.9	0.3	22.9	0.30	6.75	0.17	2.7708	0.35
9	5.1	0.1	7.3	0.10	24	1.0	23.8	0.4	99.7	0.3	22.8	0.31	6.87	0.17	3.0398	0.35
10	5.3	0.1	29.7	0.10	24	1.0	24.0	0.4	99.0	0.3	23.2	0.30	58.26	5.02	4.4024	0.35
11	20.4	0.1	29.7	0.10	24	1.0	25.0	0.4	99.1	0.3	23.3	0.30	60.05	5.18	6.1983	0.35
12	40.1	0.1	29.7	0.10	24	1.0	25.0	0.4	99.2	0.3	23.4	0.30	60.06	5.18	7.0276	0.35

(b)

case	mndot_in (g/min)	U_mndot (g/min)	Pair (psi)	U_Pair (psi)	Tair (C)	U_Tair (C)	Tin (C)	U_Tin (C)	Patm (kPa)	U_Patm (kPa)	Tatm (C)	U_Tatm (C)	Qair (ml/min)	U_Qair (ml/min)	Pin (kPa)	U_Pin (kPa)
2	20.4	0.1	5.2	0.10	24	1.0	26.6	0.4	101.7	0.3	23.4	0.36	0.55	0.06	1.5	0.35
4	5.3	0.1	6.1	0.10	24	1.0	25.8	0.4	101.4	0.3	24.2	0.31	1.20	0.10	1.9	0.35
5	20.3	0.1	5.6	0.10	24	1.0	27.6	0.4	101.6	0.3	24.1	0.32	1.86	0.15	2.3	0.35
6	40.4	0.1	4.6	0.10	24	1.0	25.9	0.4	101.6	0.3	23.8	0.34	1.67	0.13	2.6	0.35
8	20.3	0.1	8.1	0.10	24	1.0	26.8	0.4	101.7	0.3	24.2	0.30	7.10	0.18	3.7	0.35

Table D.2. Computed uncertainties of flow properties for (a) image based void fraction and (b) slip ratio base void fraction experiments

(a)

case	\dot{m}_{air} (g/min)	$U_{\dot{m}_{\text{air}}}$ (g/min)	X	U_X	j_g (m/s)	U_{j_g} (m/s)	j_f (m/s)	U_{j_f} (m/s)
1	5.20E-05	5.70.E-06	2.1.E-05	2.3E-06	0.0072	0.0008	0.4194	0.0009
2	5.20E-05	5.70.E-06	4.1.E-05	4.5E-06	0.0072	0.0008	0.2099	0.0009
3	5.10E-05	5.60.E-06	1.6.E-04	1.8E-05	0.0072	0.0008	0.0527	0.0008
4	1.00E-04	7.90.E-06	3.2.E-04	2.5E-05	0.0141	0.0011	0.0531	0.0008
5	1.02E-04	8.10.E-06	8.2.E-05	6.5E-06	0.0145	0.0011	0.2097	0.0008
6	1.03E-04	8.10.E-06	4.1.E-05	3.2E-06	0.0145	0.0011	0.4193	0.0009
7	7.33E-04	1.85.E-05	2.9.E-04	7.4E-06	0.1022	0.0026	0.4206	0.0009
8	7.44E-04	1.88.E-05	5.9.E-04	1.5E-05	0.1044	0.0027	0.2094	0.0008
9	7.57E-04	1.91.E-05	2.4.E-03	7.1E-05	0.1059	0.0027	0.0529	0.0009
10	1.30E-02	1.12.E-03	3.8.E-02	3.2E-03	1.8192	0.1571	0.0551	0.0009
11	1.34E-02	1.15.E-03	1.0.E-02	8.9E-04	1.8603	0.1607	0.2128	0.001
12	1.34E-02	1.16.E-03	5.3.E-03	4.6E-04	1.8524	0.16	0.4185	0.0014

(b)

case	\dot{m}_{air} (g/min)	$U_{\dot{m}_{\text{air}}}$ (g/min)	X	U_X	j_g (m/s)	U_{j_g} (m/s)	j_f (m/s)	U_{j_f} (m/s)
2	5.60E-05	6.50E-06	4.4E-05	5.1E-06	0.0078	0.0009	0.2128	0.0009
4	1.26E-04	1.05E-05	3.8E-04	3.3E-05	0.0176	0.0015	0.0549	0.0009
5	1.91E-04	1.59E-05	1.5E-04	1.3E-05	0.0266	0.0022	0.2120	0.0009
6	1.63E-04	1.31E-05	6.5E-05	5.2E-06	0.0225	0.0018	0.4216	0.0009
8	8.18E-04	2.12E-05	6.5E-04	1.7E-05	0.1129	0.0029	0.2116	0.0009

Table D.3. Uncertainties of homogeneous void fractions from based on (a) image and (b) slip ratio experiments

(a)				(b)			
case	β	U_β	Relative uncertainty (%)	case	β	U_β	Relative uncertainty (%)
1	0.02	0.002	11	2	0.04	0.004	11
2	0.03	0.004	11	4	0.24	0.016	6
3	0.12	0.012	10	5	0.11	0.008	7
4	0.21	0.013	6	6	0.05	0.004	8
5	0.06	0.005	7	8	0.35	0.006	2
6	0.03	0.003	8				
7	0.20	0.004	2				
8	0.33	0.006	2				
9	0.67	0.007	1				
10	0.97	0.003	0.3				
11	0.90	0.008	1				
12	0.82	0.013	2				

D.2 Uncertainty of Void Fraction

Void fraction base on slip ratio is expressed by slip ratio, mass fraction and density and presented in Eq. D.9.

$$\alpha_{slip} = \frac{1}{1 + S \left(\frac{1-x}{x} \frac{\rho_g}{\rho_f} \right)} \quad \& \quad S = \frac{u_g}{u_f} \quad (D.9)$$

Using Kline-McClintock relationship, the uncertainty of void fraction based on slip ratio is defined as

$$U_{\alpha,slip} = \sqrt{\left(\frac{\partial \alpha_{slip}}{\partial S} U_S \right)^2 + \left(\frac{\partial \alpha_{slip}}{\partial X} U_X \right)^2 + \left(\frac{\partial \alpha_{slip}}{\partial \rho_g} U_{\rho_g} \right)^2} \quad (D.10)$$

where S and X are slip ratio and mass fraction, respectively. The uncertainty equation of void fraction based on slip ratio is associated with uncertainty of slip ratio, mass fraction and density of air. The uncertainty of water density was discussed in the previous section.

To determine uncertainty of slip ratio with Eq. D.9, uncertainties of local velocities for air and water, also, need to be determined. The uncertainty equation of slip ratio and associated uncertainties of local gas and liquid velocities are presented in Eq. D.11 and Eq. D.13.

$$U_S = \sqrt{\left(\frac{\partial S}{\partial u_g} U_{u_g} \right)^2 + \left(\frac{\partial S}{\partial u_f} U_{u_f} \right)^2} \quad (D.11)$$

$$U_{u_g} = \sqrt{(B_{u_g})^2 + (P_{u_g})^2} \quad \& \quad U_{u_f} = \sqrt{(U_{u_f, \max})^2 + (P_{u_f})^2} \quad (D.12)$$

$$U_{u_f, \max} = \sqrt{B_{u_f, \max}^2 + P_{u_f, \max}^2} \quad (\text{D.13})$$

where B and P are total bias and precision errors, respectively. The total bias and precision errors for local air velocity are

$$B_{u_g} = \sqrt{\left(\frac{\partial}{\partial t} U_{pix}\right)^2 + \left(U_{u_g, image\ filter}\right)^2} \quad (\text{D.14})$$

$$P_{u_g} = \frac{U_{stdev}}{\sqrt{N_{sample}}} \quad (\text{D.15})$$

where U_{pix} , $U_{u_g, image\ filter}$, U_{stdev} and N_{sample} are the uncertainty of pixel resolution for sequential images, uncertainty of gas velocity associated with the changes of image filter sizes from 6x6 pixels to 14x14 pixels, standard deviation of gas velocity measurement and number of samples, respectively. Equation D.15 presents the precision error from standard deviation of mean of gas velocity measurements. For liquid velocity uncertainty presented in Eqs. 12 and 13, two major uncertainties are involved. The first uncertainty is associated with the maximum values of velocity profiles to determine liquid velocities using analytical solution. The second uncertainty is the precision error in curve fits between velocity profiles generated by analytical solution and micro-PIV measurements. The uncertainty from maximum velocity has bias and precision errors in Eq. 13. The bias and precision errors for maximum velocities are determined by position error from micro-PIV measurement and the standard deviation of mean from the fluctuations of the maximum velocity at the interested streamwise locations. The bias and precision errors from the maximum velocity measurement and precision error from the velocity profile curve fit between

analytical solution and micro-PIV present in Eqs. D.16 and 17.

$$B_{u_{f,max}} = \frac{dU_{position,PIV}}{dt} \quad \& \quad P_{u_{f,max}} = U_{u_{f,max,std.mean}} \quad (D.16)$$

$$P_{u_f} = \sqrt{\frac{\sum (u_{f,piv} - u_{f,analytical})^2}{N-1}} \quad (D.17)$$

For uncertainties of mass fraction and density of gas the Kline-McClintock relationships are

$$U_X = \sqrt{\left(\frac{\partial X}{\partial \dot{m}_g} U_{\dot{m}_g}\right)^2 + \left(\frac{\partial X}{\partial \dot{m}_f} U_{\dot{m}_f}\right)^2} \quad (D.18)$$

$$U_{\rho_g} = \sqrt{\left(\frac{\partial \rho_g}{\partial P_g} U_{P_g}\right)^2 + \left(\frac{\partial \rho_g}{\partial T_g} U_{T_g}\right)^2} \quad (D.19)$$

The uncertainties of mass flow rates of gas and liquid and density of gas are discussed in the previous section of this chapter. The uncertainties of slip ratio and density of gas for all branching levels are listed in Table D.4. Also, the void fractions based on slip ratio are listed in Table D.5. The averaged relative uncertainty for void fraction based on slip ratio is approximately 5%.

Table D.4. Uncertainties of slip ratio and density of gas for all branching levels (a) image based void fraction and (b) slip ratio base void fraction experiments

Slip ratio

k_{th}	case 2	case 4	case 5	case 6	case 8
0	1	1	0.9	1.2	1.1
1	1	0.7	1	1	1
2	1	1	0.9	1	0.9
3	1.1	1	1.2	1.1	1.1
4	1.3	1	1.1	1.3	1.2

Uncertainty

k_{th}	case 2	case 4	case 5	case 6	case 8
0	0.038	0.019	0.031	0.105	0.045
1	0.019	0.023	0.037	0.039	0.027
2	0.026	0.027	0.022	0.054	0.034
3	0.032	0.07	0.038	0.03	0.047
4	0.063	0.027	0.042	0.039	0.032

Density of air

(a)

case	ρ_g (kg/m ³)	Uncertainty of ρ_g (kg/m ³)
1	1.20	0.0037
2	1.19	0.0037
3	1.18	0.0037
4	1.18	0.0037
5	1.18	0.0037
6	1.18	0.0037
7	1.20	0.0037
8	1.19	0.0037
9	1.19	0.0037
10	1.19	0.0037
11	1.20	0.0037
12	1.20	0.0037

(b)

case	ρ_g (kg/m ³)	Uncertainty of ρ_g (kg/m ³)
2	1.20	0.0037
4	1.20	0.0037
5	1.20	0.0037
6	1.20	0.0037
8	1.21	0.0037

Table D.5. Void fractions based on slip ratio and uncertainties for all cases and branching levels.

α_{slip}					
k_{th}	case 2	case 4	case 5	case 6	case 8
0	0.04	0.24	0.12	0.04	0.33
1	0.04	0.31	0.11	0.05	0.35
2	0.04	0.24	0.12	0.05	0.37
3	0.03	0.24	0.09	0.05	0.33
4	0.03	0.24	0.10	0.04	0.31

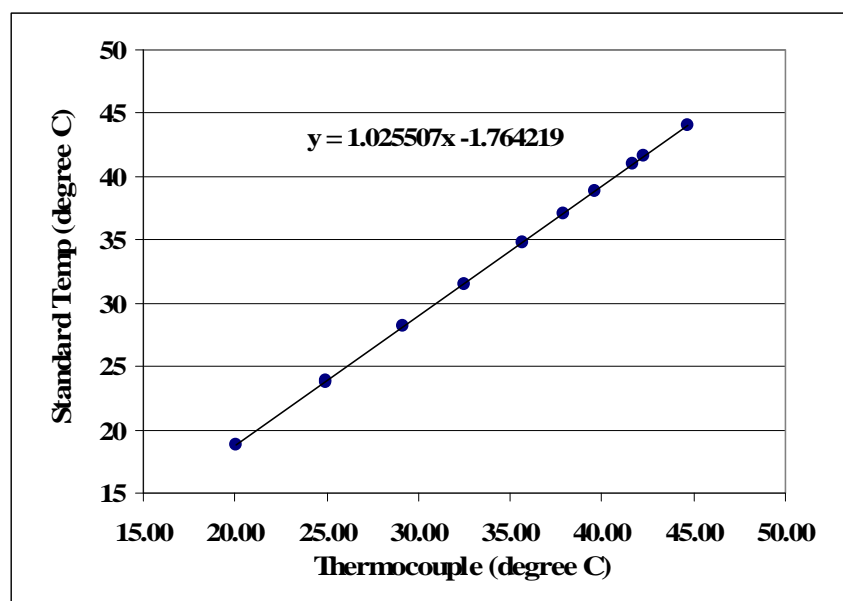
Uncertainty of α_{slip}					
k_{th}	case 2	case 4	case 5	case 6	case 8
0	0.002	0.010	0.005	0.004	0.010
1	0.002	0.012	0.006	0.003	0.008
2	0.002	0.011	0.005	0.003	0.010
3	0.002	0.015	0.005	0.002	0.011
4	0.002	0.010	0.005	0.002	0.007

D.3 Calibration Curve and Uncertainties

T-type thermocouple

Standard_error (+/-) 0.3 C
 Manufacture 1C or 75% choose bigger one
 Regress_error 0.0216
 student-t 2.045

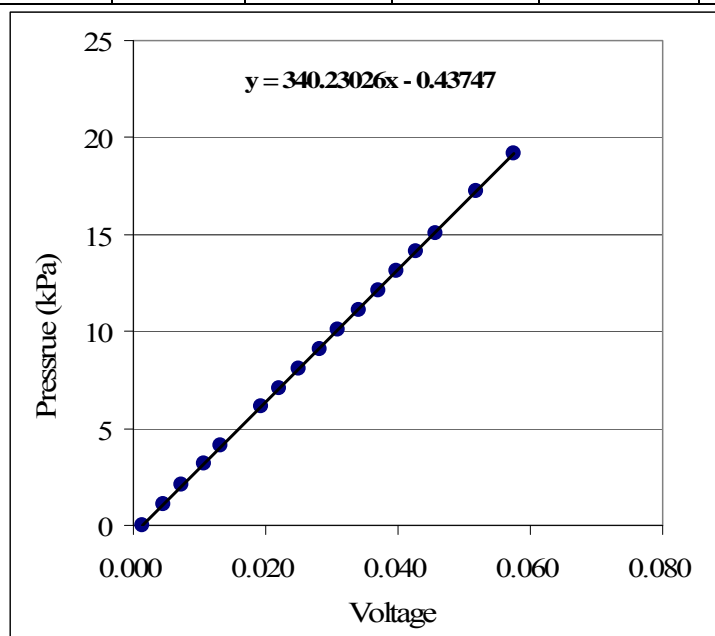
	Thermocouple	Precession	Precession	Total	Total	Total
standard	(T-type)	error	95%conf.	calibration	error	error
(degree C)	(degreeC)	(degreeC)	(degreeC)	uncertainty		+/-1°C
18.77	20.05	0.0014	0.0029	0.0218	0.33	1.04
23.77	24.91	0.0014	0.0029	0.0218	0.35	1.04
23.90	24.99	0.0014	0.0028	0.0218	0.35	1.04
28.17	29.18	0.0013	0.0028	0.0218	0.37	1.04
31.54	32.46	0.0014	0.0028	0.0218	0.38	1.04
34.81	35.68	0.0013	0.0028	0.0218	0.40	1.04
37.07	37.88	0.0013	0.0028	0.0218	0.41	1.04
38.90	39.64	0.0013	0.0028	0.0218	0.42	1.04
40.99	41.67	0.0013	0.0027	0.0218	0.43	1.04
41.60	42.29	0.0013	0.0028	0.0218	0.43	1.04
44.02	44.67	0.0013	0.0027	0.0218	0.45	1.04



Inlet pressure

Standard error 0.3447 kPa <--0.05% FS of 100 psia
 Regress. error 0.0314 kPa
 PT_manufacture
 error 0.1000 mV

				precession	
				95% conf.	total error
P_abs (kPa)	dP (kPa)	Voltage	SD	(kPa)	(kPa)
100.8	0	0.001	1.68E-05	0.01	0.35
101.9	1.1	0.004	4.98E-05	0.03	0.35
102.9	2.1	0.007	3.98E-05	0.03	0.35
104.0	3.2	0.011	6.11E-05	0.04	0.35
104.9	4.1	0.013	5.6E-05	0.04	0.35
106.9	6.1	0.019	2.29E-05	0.02	0.35
107.9	7.1	0.022	3.72E-05	0.02	0.35
108.9	8.1	0.025	5.01E-05	0.03	0.35
109.9	9.1	0.028	2.06E-05	0.01	0.35
110.9	10.1	0.031	1.84E-05	0.01	0.35
111.9	11.1	0.034	4.47E-05	0.03	0.35
112.9	12.1	0.037	1.71E-05	0.01	0.35
113.9	13.1	0.040	7.83E-05	0.05	0.35
114.9	14.1	0.043	1.96E-05	0.01	0.35
115.9	15.1	0.046	2.15E-05	0.01	0.35
118.0	17.2	0.052	1.78E-05	0.01	0.35
120.0	19.2	0.058	1.83E-05	0.01	0.35



Gas injector pressure

11-20-2007

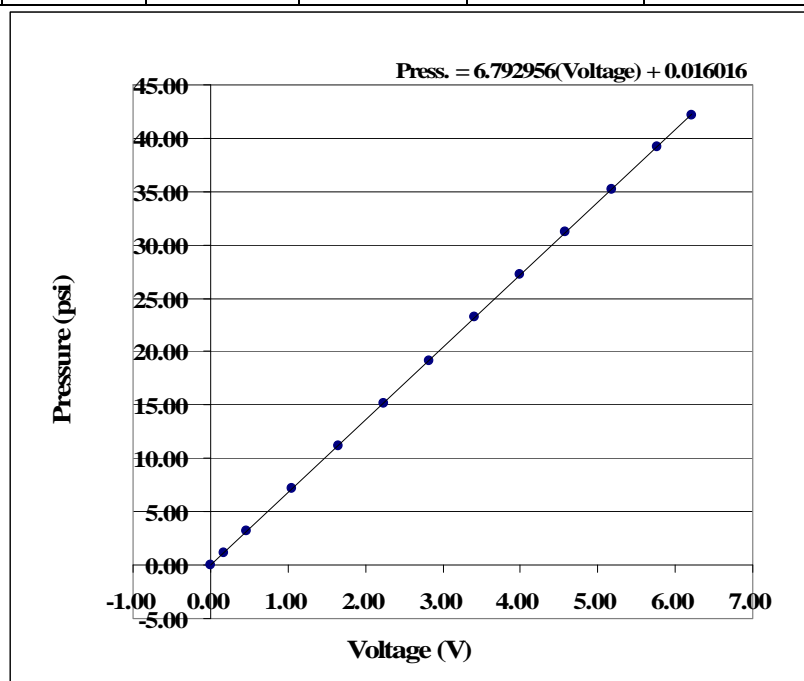
Younghoon Kwak

Manufact error 0.1 psi

Standard error 0.05 psi

Regression error 0.02 psi

Standard psia	Standard psig	pooled mean (V)	pooled std. of mean (V)	95% conf. precision error (V)	95% conf. precision error (psi)	U_total (psi)
14.80	0.00	0.00	3.38E-06	6.84E-06	4.64E-05	0.1
22.00	7.20	1.06	6.69E-06	1.35E-05	9.18E-05	0.1
30.00	15.20	2.23	8.17E-06	1.65E-05	1.12E-04	0.1
38.00	23.20	3.41	7.85E-06	1.59E-05	1.08E-04	0.1
46.00	31.20	4.59	9.37E-06	1.89E-05	1.29E-04	0.1
54.00	39.20	5.77	1.59E-05	3.21E-05	2.18E-04	0.1
57.00	42.20	6.22	4.96E-06	1.00E-05	6.81E-05	0.1
50.00	35.20	5.18	1.20E-05	2.42E-05	1.64E-04	0.1
42.00	27.20	4.00	9.47E-06	1.91E-05	1.30E-04	0.1
34.00	19.20	2.82	8.75E-06	1.77E-05	1.20E-04	0.1
26.00	11.20	1.65	1.09E-05	2.21E-05	1.50E-04	0.1
18.00	3.20	0.47	8.69E-06	1.76E-05	1.19E-04	0.1
16.00	1.20	0.18	3.40E-06	6.87E-06	4.66E-05	0.1



Inlet mass flow meter

Linear regression with const intercept

U regress 95% conf.

mdot in (g/min)	mdot out (g/min)
0.04	0.01

Manufacturing error

mass	(g/min)
flowmeter	0.045

notes:

Flowmeter setup: 10 kHz / 40 g/min

Calibrated mass flowmeters at temp of 24.2 C and density of 998 kg/m³

File name	Catch and Weight				Mass Flowmeter						U over all	Relative uncertainty
	mass (g)	dt (min)	mdot (g/min)	U meas (g/min)	mdot in (g/min)	stdev in (g/min)	stdev out (g/min)	N	t_95	95% conf stdev of mean mdot in (g/min)	mdot in (g/min)	% error (%)
2	168.2	11.26	14.9	0.009	15.0	0.11	0.11	88	2.0	0.023	0.068	0.45
3	180.9	8.93	20.3	0.018	20.4	0.26	0.26	69	2.0	0.063	0.091	0.45
4	204.7	8.24	24.8	0.023	24.9	0.16	0.14	65	2.0	0.039	0.078	0.31
5	341.1	11.31	30.2	0.014	30.2	0.14	0.15	89	2.0	0.030	0.071	0.24
6	571	16.25	35.1	0.011	35.2	0.05	0.05	127	2.0	0.010	0.065	0.18
7	352.9	8.81	40.1	0.061	40.1	0.04	0.04	69	2.0	0.011	0.089	0.22
8	341.9	9.01	37.9	0.036	38.0	0.05	0.05	71	2.0	0.013	0.074	0.19
9	347.6	10.52	33.0	0.026	33.0	0.06	0.07	82	2.0	0.014	0.070	0.21
10	287.8	10.29	28.0	0.028	28.0	0.07	0.07	77	2.0	0.015	0.071	0.25
11	220.3	9.56	23.0	0.027	23.0	0.03	0.03	75	2.0	0.008	0.069	0.30
12	229.4	12.74	18.0	0.012	18.0	0.04	0.05	100	2.0	0.009	0.065	0.36
13	162.2	12.49	13.0	0.013	13.0	0.03	0.03	95	2.0	0.007	0.065	0.50
14	153.3	15.35	10.0	0.007	10.0	0.04	0.04	120	2.0	0.006	0.064	0.64

